INTERPLAY BETWEEN MECHANICS, ELECTRONICS, AND ENERGETICS IN ATOMIC-SCALE JUNCTIONS

Sriharsha V. Aradhya

Submitted in partial fulfillment of the
requirements for the degree of
Doctor of Philosophy
in the Graduate School of Arts and Sciences

COLUMBIA UNIVERSITY

2013

ABSTRACT

Interplay between mechanics, electronics, and energetics in atomic-scale junctions

Sriharsha V. Aradhya

The physical properties of materials at the nanoscale are controlled to a large extent by their interfaces. While much knowledge has been acquired about the properties of material in the bulk, there are many new and interesting phenomena at the interfaces that remain to be better understood. This is especially true at the scale of their constituent building blocks – atoms and molecules. Studying materials at this intricate level is a necessity at this point in time because electronic devices are rapidly approaching the limits of what was once thought possible, both in terms of their miniaturization as well as our ability to design their behavior. In this thesis I present our explorations of the interplay between mechanical properties, electronic transport and binding energetics of single atomic contacts and single-molecule junctions. Experimentally, we use a customized conducting atomic force microscope (AFM) that simultaneously measures the current and force across atomic-scale junctions. We use this instrument to study single atomic contacts of gold and silver and single-molecule junctions formed in the gap between two gold metallic point contacts, with molecules with a variety of backbones and chemical linker groups. Combined with density functional theory based simulations and analytical modeling, these experiments provide insight into the correlations between mechanics and electronic structure at the atomic level.

In carrying out these experimental studies, we repeatedly form and pull apart nanoscale junctions between a metallized AFM cantilever tip and a metal-coated substrate. The force and conductance of the contact are simultaneously measured as each junction evolves through a

series of atomic-scale rearrangements and bond rupture events, frequently resulting in single atomic contacts before rupturing completely. The AFM is particularly optimized to achieve high force resolution with stiff probes that are necessary to create and measure forces across atomic-size junctions that are otherwise difficult to fabricate using conventional lithographic techniques. In addition to the instrumentation, we have developed new algorithmic routines to perform statistical analyses of force data, with varying degrees of reliance on the conductance signatures.

The key results presented in this thesis include our measurements with gold metallic contacts, through which we are able to rigorously characterize the stiffness and maximum forces sustained by gold single atomic contacts and many different gold-molecule-gold single-molecule junctions. In our experiments with silver metallic contacts we use statistical correlations in conductance to distinguish between pristine and oxygen-contaminated silver single atomic contacts. This allows us to separately obtain mechanical information for each of these structural motifs. The independently measured force data also provides new insights about atomic-scale junctions that are not possible to obtain through conductance measurements alone. Using a systematically designed set of molecules, we are able to demonstrate that quantum interference is not quenched in single-molecule junctions even at room temperature and ambient conditions. We have also been successful in conducting one of the first quantitative measurements of van der Waals forces at the metal-molecule interface at the single-molecule level. Finally, towards the end of this thesis, we present a general analytical framework to quantitatively reconstruct the binding energy curves of atomic-scale junctions directly from experiments, thereby unifying all of our mechanical measurements. I conclude with a summary of the work presented in this thesis, and an outlook for potential future studies that could be guided by this work.

CONTENTS

TABLE OF FIGURES

ix

ACKNOWLEDGEMENTS

This thesis marks an important milestone in my life, and many people have played an important role in my journey towards it. First, I am most grateful for the mentorship that I have received from Prof. Latha Venkataraman. I have admired her rigor and depth of knowledge throughout my Ph.D. experience. At the same time I feel very fortunate to have received her guidance and motivation whenever I needed it, while also enjoying the freedom to explore ideas on my own. Her generosity and able leadership, as well as the collaborative spirit she has fostered in our research group have been essential to whatever success I have had during my doctoral work.

I thank Dr. Mark Hybertsen for all his guidance, and I feel particularly lucky for having had many opportunities to discuss our research with him. His patience and eagerness for explain difficult concepts – along with his breadth of understanding – have inspired me at every instance. After each interaction, I have felt that he was not only nudging me towards answers to my questions, but that he was in fact leading me to frame and ask better questions in the first place. I have also been very fortunate to have had fruitful collaborations with chemists, especially Prof. Colin Nuckolls and members of his research group. I am always amazed by how quickly and intuitively new ideas are developed whenever I have participated in discussions with him and Dr. Michael Steigerwald. I also thank Prof. Herman and Prof. Marianetti for their guidance and for being a part of my doctoral committee.

I have enjoyed the day-to-day work in our lab because of the talented and friendly students and postdocs in our group. In particular, much of my initial exposure to the force experiment came from Mike Frei, whose excitement about this research and his friendly introduction to the lab played a crucial role in the development of my interest in our lab's

research. I have had the privilege of knowing most of the members who have been part of our young group, and I have cherished my all interactions with each of them – both inside and outside the lab.

My associations with several student groups and organizations at Columbia have been personally fulfilling in many ways. I will fondly remember hawking tickets to grad students, and struggling to come up with cheap ideas for social outings as a part of the graduate student council and the international student office. Most of all, I have tremendously enjoyed my time as a DJ at WKCR-FM New York. I won't forget the many interesting people I have met and all the beautiful music I have heard due to this affiliation anytime soon. I will miss New York when I leave, but I will fondly remember these past few years as a special time that enriched my life.

Finally, and most importantly, I thank my family for their patience and unwavering support throughout the years. My father and mother have always encouraged me to follow my curiosities, while constantly motivating me to set a higher bar for myself. And my sister has been my ardent supporter, ever since I can remember. Perhaps the biggest vote of confidence I have received came from my wife who (bravely) agreed to marry me one month before I started working towards the Ph.D. I couldn't have made it without all of you.

Thank you!

Sriharsha

To my family,

for the roots and the wings…

1

Introduction and motivation

The idea of using individual molecules as active electronic components provided the impetus to develop a variety of experimental platforms to probe their electronic transport properties. Among these, single-molecule junctions in a metal-molecule-metal motif have contributed significantly to our fundamental understanding of the basic principles required to realize molecular scale electronic components. Going beyond electronic transport characterization, new approaches to investigate metal-molecule-metal junctions with multiple probes are needed to understand both the fundamental and applied aspects of mechanical, optical and thermoelectric properties at the atomic and molecular scales, as well as to demonstrate quantum phenomena like interference and manipulation of spins in single-molecule circuits that can herald new device concepts with no classical analogues. This thesis describes my efforts to use simultaneous measurements of force and conductance to explore the interrelations between mechanics, electronics and energetics at the atomic scale in single-atomic contacts and single-molecule junctions.

❖ Contents of this chapter are adapted from a review article: S. V. Aradhya and L. Venkataraman, Nature Nanotechnology, 2013. **8**(6): p. 399-410.

Stimulated by the initial proposal that molecules could be used as the functional building blocks in electronic devices[1], researchers around the world have been probing transport phenomena at the single-molecule level both experimentally and theoretically[2-11]. Recent experimental advances include the demonstration of conductance switching[12-16], rectification[17-21], and illustrations on how quantum interference effects[22-26] play a critical role in the electronic properties of single metal-molecule-metal junctions. The focus of these experiments has been to both provide a fundamental understanding of transport phenomena in nano-scale devices as well as to demonstrate functionality from chemistry in single molecule junctions. Although to date there are no 'molecular electronics' devices manufactured commercially, fundamental research in this area has advanced significantly.

Specifically, the drive to create functional molecular devices has pushed the frontiers of both measurement capabilities and our fundamental understanding of varied physical phenomena at the single-molecule level, including mechanics, thermoelectrics, optoelectronics and spintronics in addition to electronic transport characterizations. Metal-molecule-metal junctions thus represent a powerful template for understanding and controlling these physical and chemical properties at the atomic and molecular length scales. In this realm, molecular devices differ from devices based on quantum dots as the latter do not generally consist of systems where the structure is defined with atomic precision. Combined with the vast toolkit afforded by rational molecular design[22], these techniques hold a significant promise towards the development of actual devices that can transduce a variety of physical stimuli, beyond their proposed utility as electronic elements[23]. Together, these varied investigations underscore the importance of single molecule junctions in current and future research aimed at understanding and controlling a variety of physical interactions at the atomic and molecular length scale.

1.1 Electronic transport and quantum interference in atomic-size junctions

Atomic-scale junctions have proven to be fundamental tools for investigating quantum mechanical aspects of electronic transport [24]. Figure 1.1a,b show schematic illustrations of atomic-scale metallic and single-molecule junctions, respectively, consisting of a metallic 'source' and 'drain' electrodes on either side of a single or a few metallic atoms or molecules. The conductance (G) can be quantified by applying a bias voltage (V) between the source and drain electrodes, and measuring the current (I) that flows through the junction as a result of this bias:

$$G = I / V \qquad \textbf{Eq. 1-1}$$

Figure 1.1. Schematic representation of an atomic-scale metallic junction and a molecular junction. Electronic transport through these junctions can be quantified through the application of a bias voltage (V) and measuring the resulting current (I) flowing through the junction. Chemical linkers are typically needed to bind the molecule to the metallic electrodes. Spheres represent atoms: yellow - Au, grey - C, white-H, blue - N.

The electronic transport in the atomic-scale region is in the ballistic transport regime, *i.e.*, the length of the conducting region is smaller than the mean free path as well as the phase relaxation length of the conducting electrons in the material. In this scenario, the transport can be thought of as arising from transmission of electrons from one electrode to the other[25]. Under a small applied bias (V_{dc}), the conductance is given by the Landauer-Buttiker formula:

$$G\big|_{V \to 0} = \frac{dI}{dV}\bigg|_{V \to 0} = \frac{2e^2}{h} \sum \tau_i \qquad \textbf{Eq. 1-2}$$

where 'e' is the charge of an electron, 'h' is the Planck's constant and τ is the transmission (the probability for an electron to tunnel from the source to the drain electrode). The summation is carried out over 'i' transmission channels that contribute to conductance at a specified energy, namely the Fermi energy. Specifically, for a one-atom wide wire with a single fully transmitting channel ($\tau = 1$), the conductance is $G_0=2e^2/h$ ($\approx$ 77.5 μS $\approx$ [12.9 kΩ]$^{-1}$), the quantum of conductance.

In the case of a single-molecule junction, the conduction typically occurs through non-resonant coherent transport mechanism, where the alignment and broadening of the molecular orbitals becomes critical[26]. Figure 1.2a shows a schematic energy level diagram for a single molecule junction, depicting the case when the highest occupied molecular orbital (HOMO) is closer to the Fermi level of the metallic electrodes than the lowest unoccupied molecular orbital (LUMO). If in addition, the HOMO and LUMO are far from the Fermi energy (E_F) of the metallic electrodes, transport is not resonant, and the conductance of the single-molecule junctions is typically less than the quantum of conductance at small bias values. Figure 1.2b schematically shows the transmission in such an idealized
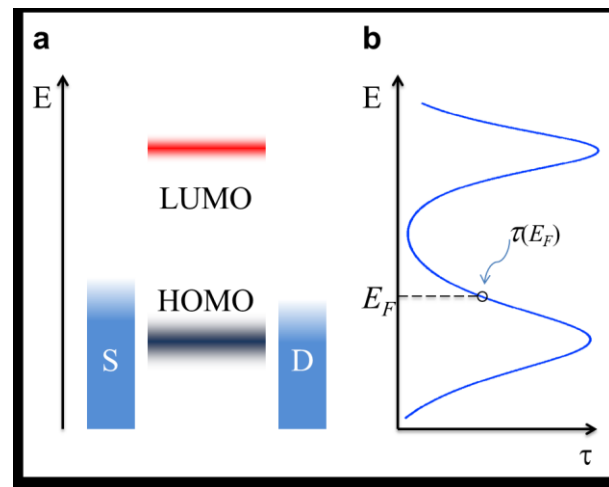
Figure 1.2. Electronic transport in a single-molecule junction. (a) The energy level diagram illustrates the presence of the highest occupied (HOMO) and lowest unoccupied (LUMO) molecular orbitals that modulate the electronic transport between the source and drain electrodes. (b) The transmission function

junction as a function of energy. The conductance at small bias voltages can simply be evaluated as the transmission probability at the Fermi energy, $\tau(E_F)$. Therefore, measurement of the

conductance probes an important aspect of the quantum mechanical electronic transport in these atomic-size junctions. Experimentally, conductance measurements are typically performed using scanning tunneling microscopes (STM) and conducting atomic force microscopes (AFM), or through specially microfabricated structures[27]. The STM and AFM based methods provide two distinct advantages: a) nanometer-sized gaps are easier to achieve using STM/AFM, and b) thousands of individual junctions can be measured during the course of an experiment to statistically capture inevitable microscopic variations in the atomic-scale structure of the junctions.

Additional complexities in the electronic transport properties of atomic-scale junctions are introduced by one of the quintessential quantum mechanical phenomenon - quantum interference - that arises due to the wave nature of the electrons when the device length scale becomes comparable to the electronic phase coherence length. Although this length scale criteria is already satisfied by mesoscale devices[28], experiments at the molecular level are not merely a simple extension of such measurements down to the atomic scale; instead, they provide new insights and methods towards controlling charge transport at the level of the wavefunction through chemical design and, potentially, through electrical control. A prime example is the dramatic lowering of the conductance (Figure 1.3) of a cross-conjugated (or a *meta*-terminated) molecule when compared with the linearly conjugated (or *para*-terminated) analogue, as predicted theoretically[29, 30]. Formally, the reduced conductance of cross-conjugated molecular junctions is due to an anti-resonance in the junction transmission function[31], *i.e.*, $\tau(E \to E_F) = 0$. Controlling the position of this anti-resonance, relative to the electrode Fermi level could open up a pathway to create a quantum-interference-controlled molecular switch with a potentially large on-off ratio[32-35]. It has also been proposed that it might be possible to could

toggle between a conjugated and cross-conjugated molecular junction through chemically or conformationally induced changes[33, 36].

The characteristic signature for destructive interference in molecular junctions is the anti-resonance in the transmission probability through the junction; this can, in principle, be probed by measuring the differential conductance of the junction as a function of applied

para- terminated molecule

meta- terminated molecule

Figure 1.3. Chemical structure and quantum interference. Subtle chemical differences such as (a) *para-* versus (b) *meta-* terminations of the chemical linkers in a molecule (benzene diamine in this example) can drastically alter the conductance of the single-molecule junction due to destructive quantum interference.

bias voltage. Although this has not been achieved to date in a single-molecule junction where the conductance signal-to-noise can be quite small, Guédon *et al.* were able to show evidence for a transmission anti-resonance in a junction composed of about 100 molecules[37]. They used a conducting AFM technique[38] to measure the differential conductance of molecular junctions in a series of anthraquinone derivatives that were either cross-conjugated or linearly conjugated. They observe that the conductance of the cross-conjugated molecular junction was two orders of magnitude lower than that of the linearly conjugated one, even though the difference in their HOMO and LUMO energies was almost the same. Furthermore, the differential conductance measured through the cross-conjugated system showed clear evidence for an anti-resonance, with a sharp dip in the differential conductance close to zero-bias. Although these devices could not be gated electrically in these experiments, the results show that a shift in molecular anti-resonance in such a system by ~0.5 V would yield a two-order of magnitude increase in

conductance. The fact that discrete energy levels in a molecular junction allow for interference effects to be preserved even at high temperatures is technologically important. The ability to control interference effects encoded in the chemical structure of a molecule could enable novel functionalities that reliably operate at room temperature.

1.2 The need for mechanical measurements and a brief overview of experimental techniques

Measurements of electronic properties of nanoscale and molecular junctions do not, in general, provide direct structural information about the junction. One of the early techniques to directly image at the atomic resolution while measuring electronic transport was demonstrated by Ohnishi *et al.* for monoatomic Au wires[39]. However this technique has not proved feasible for investigating metal-molecule-metal junctions with carbon-based organic molecules. Simultaneous mechanical and electronic measurements (Figure 1.4) provide an alternate method to address questions relating to the structure of atomic-size junctions[24]. Specifically, the measurements of forces across single metal-molecule-metal junctions and of metal point-contacts provide independent mechanical information, which can be used to: 1) relate junction structure to conductance, 2) quantify bonding at the molecular scale, and 3) provide a mechanical 'knob' that can be used to control transport through nanoscale devices. The first simultaneous measurement of force and conductance in nanoscale junctions were carried out for Au point-contacts by Rubio *et al.*[40], who showed that abrupt changes in

Figure 1.4. Simultaneous measurement of force and in atomic-size junctions. Force provides independent information about junction structure and evolution.

force across the junction are correlated with quantized changes in its conductance, unambiguously demonstrating the structural basis for the observed conductance quantization.

These initial experiments relied on the so-called static mode of AFM force spectroscopy, where the force on the cantilever is monitored as a function of junction elongation. In this method the deflection of the AFM cantilever is directly related to the force on the junction by Hooke's law (Force = cantilever stiffness × cantilever deflection). In contrast, dynamic mode AFM force spectroscopy makes use of the frequency shift of an AFM cantilever under forced near-resonance oscillation to detect changes in the cantilever stiffness due to its interaction with the sample; this frequency shift can then be related to the gradient of the tip/sample interaction force. In particular, the 'q-Plus' configuration[41] utilizes a very stiff tuning fork as a force sensor, thereby enabling high resolution measurements of atomic-size junctions. The basic advantage of this approach is that frequency-domain measurement of high-Q resonators is significantly easier to carry out with high precision. This technique has recently enabled studies of single atomic metallic contacts[42, 43], as well as various molecules adsorbed on metallic surfaces[44-47]. However, in addition to experimental complexity of this technique, recovering the junction force from frequency shifts, especially in the presence of dissipation and dynamic structural changes during junction elongation experiments, still remains challenging[48].

The feasibility of extending the static mode AFM technique from metal point contacts to ambient measurements of force and conductance across single-molecule junctions was demonstrated by Tao *et al.*[49], analogous to their STM based break-junction scheme for conductance measurements[8]. In this approach, single-molecule junctions are formed between an Au-metal substrate and an Au-coated cantilever in an environment of molecules. Measurements of current through the junction under an applied bias determine conductance,

while simultaneous measurements of cantilever deflection relate to the force applied across the junction. Although measurements of current through such junctions are easily accomplished using standard commercial instrumentation, measurements of forces with high resolution are not straightforward. This is because a rather stiff cantilever (with typical spring constant of ~50 N/m) is typically required in order to break the Au-point contact that is first formed between the tip and substrate, before the molecular junctions are created. The force resolution is then limited by the smallest deflection of the cantilever that can be measured. With a custom-designed conducting AFM we have achieved a cantilever displacement resolution of ~2 pm (*cf.* Au atomic diameter ~280 pm) using an optical detection scheme, allowing the AFM force noise floor to be as low as 0.1 nN even with these stiff cantilevers. The details of our experimental setup have previously been presented elsewhere[50].

In most of the experiments mentioned thus far, the measured forces were typically used as a secondary probe of junction properties, instead relying on the junction conductance as the primary signature for the formation of the junction. However, as is the case in large biological molecules[51, 52], forces measured across single-molecule junctions can also provide the primary signature, thereby making it possible to characterize non-conducting molecules that nonetheless do form junctions. This is especially important in the study of single-molecule junctions that exhibit destructive interference (as discussed in the previous section), where it is also necessary to distinguish between the effects of quantum interference from possible modulations induced by more mundane aspects such as contact mechanics[53]. In addition, molecules possess many internal degrees of motion (including vibrations and rotations) that can directly influence the electronic transport[54], and the measurement of forces with such molecules can open up new avenues for mechano-chemistry[55]. This potential of force

measurements in elucidating the fundamentals of electronic transport and binding interactions at the single-molecule level is prompting new activity in this area of research[56-58].

1.3   Scientific questions and outline of thesis

The focus of this thesis is the study of the interplay between mechanics, electronics and energetics of atomic-scale junctions. As our main experimental tool, we use the custom-designed conducting AFM optimized for high force resolution to perform break-junction measurements. Following this introductory chapter which provided a brief background of experimental techniques and the motivations for simultaneous measurement of conductance and force in atomic-scale junctions, the subsequent chapters in this thesis are organized according to certain central questions or themes that I, along with our collaborators, have explored during the course of my doctoral research:

Chapter 2 presents the experimental methods and several automated analysis procedures that were developed to extract and statistically compile information from large experimental datasets. Such techniques are important because the inevitable microscopic variability of the structure in these atomic-scale junctions necessitates the quantification of not only the mean value, but also the estimates of the variability in measured properties. The application of these techniques to obtain the rupture force of Au single atomic contacts and different Au-molecule-Au single-molecule junctions with a variety of backbones and chemical linker groups are presented. The good agreement of these experimentally to density functional theory based calculations validates our experimental and analysis techniques.

Chapter 3 summarizes our study of the electronic transport and stability of single-molecule junctions formed by carboxyl terminated alkane and aromatic molecules. Using a

combination of systematic conductance measurements and force measurements, we are able to identify the bonding mechanism responsible for the formation of these junctions. In addition to the intrinsic value, an understanding of the binding mechanism is an important step towards enabling the many attractive chemical modification opportunities afforded by the carboxyl group.

Chapter 4 presents our study of a series of stilbene derivatives with methyl-sulfide linkers that systematically probed the occurrence of destructive interference phenomena in single-molecule junctions. This study is one of the first to establish the robustness of destructive interference in electronic transport in single-molecule junctions, while simultaneously verifying that the mechanics of the junction is unaltered due to the similar S-Au donor-acceptor binding at the contacts for each of the molecules in the series.

Chapter 5 details mechanical measurements of single-molecule junctions of pyridine terminated molecules that goes beyond quantification of the junction rupture force. This study yielded one of the first experimental measurements of van der Waals forces at the single-molecule level that was also corroborated with state-of-the-art density functional theory calculations.

Chapter 6 presents the quantification of rupture forces in silver single-atomic contacts at room temperature in ambient conditions. We use a conductance cross-correlation analysis technique to separately analyze pristine Ag single-atomic contacts as well as point contacts with oxygen atomic impurities in series and parallel with the Ag atoms. Utilizing complementary information from force and conductance, we demonstrate the correlation of conductance with the structural evolution at the atomic scale.

Chapter 7 presents a new analytical method to reconstruct quantitative binding energy curves of atomic point contacts and single-molecule junctions directly from experimental measurements, using a simplified model for their mechanics. Comparing the results to density functional theory calculations, we find striking agreement for each of the cases considered. Combined with the demonstrated feasibility of single-molecule experiments, this technique provides an approach to significantly expand the versatility of atomic force microscopy towards quantifying binding energetics at the atomic scale – even at room temperature, and in ambient or in the presence of solvents.

Chapter 8 summarizes the conclusions and provides an outlook for future investigations that can build upon the work presented in this thesis.

1.4   References

1.   A. Aviram and M.A. Ratner, *Molecular rectifiers.* Chemical Physics Letters, 1974. **29**(2): p. 277-283.

2.   M.A. Reed, C. Zhou, C.J. Muller, T.P. Burgin, and J.M. Tour, *Conductance of a molecular junction.* Science, 1997. **278**(5336): p. 252-254.

3.   M. Di Ventra, S.T. Pantelides, and N.D. Lang, *First-principles calculation of transport properties of a molecular device.* Physical Review Letters, 2000. **84**(5): p. 979-982.

4.   R.H.M. Smit, Y. Noat, C. Untiedt, N.D. Lang, M.C. van Hemert, and J.M. van Ruitenbeek, *Measurement of the conductance of a hydrogen molecule.* Nature, 2002. **419**(6910): p. 906-909.

5.   Y.Q. Xue, S. Datta, and M.A. Ratner, *First-principles based matrix Green's function approach to molecular electronic devices: general formalism.* Chemical Physics, 2002. **281**(2-3): p. 151-170.

6.   J. Reichert, R. Ochs, D. Beckmann, H.B. Weber, M. Mayor, and H.v. Löhneysen, *Driving Current through Single Organic Molecules.* Physical Review Letters, 2002. **88**(17): p. 176804.

7.   M. Brandbyge, J.L. Mozos, P. Ordejon, J. Taylor, and K. Stokbro, *Density-functional method for nonequilibrium electron transport.* Physical Review B, 2002. **65**(16).

8.   B. Xu and N.J. Tao, *Measurement of Single-Molecule Resistance by Repeated Formation of Molecular Junctions.* Science, 2003. **301**(5637): p. 1221-1223.

9.   Y. Selzer, L.T. Cai, M.A. Cabassi, Y.X. Yao, J.M. Tour, T.S. Mayer, and D.L. Allara, *Effect of local environment on molecular conduction: Isolated molecule versus self-assembled monolayer.* Nano Letters, 2005. **5**(1): p. 61-65.

10.   L. Venkataraman, J.E. Klare, C. Nuckolls, M.S. Hybertsen, and M.L. Steigerwald, *Dependence of single-molecule junction conductance on molecular conformation.* Nature, 2006. **442**(7105): p. 904-907.

11.   H.J. Choi, M.L. Cohen, and S.G. Louie, *First-principles scattering-state approach for nonlinear electrical transport in nanostructures.* Physical Review B, 2007. **76**(15).

12.   F. Chen, J. He, C. Nuckolls, T. Roberts, J.E. Klare, and S. Lindsay, *A molecular switch based on potential-induced changes of oxidation state.* Nano Letters, 2005. **5**(3): p. 503-506.

13.   E. Lörtscher, J.W. Ciszek, J. Tour, and H. Riel, *Reversible and controllable switching of a single-molecule junction.* Small, 2006. **2**(8-9): p. 973-977.

14.   P. Liljeroth, J. Repp, and G. Meyer, *Current-induced hydrogen tautomerization and conductance switching of naphthalocyanine molecules.* Science, 2007. **317**(5842): p. 1203-6.

15.   S.Y. Quek, M. Kamenetska, M.L. Steigerwald, H.J. Choi, S.G. Louie, M.S. Hybertsen, J.B. Neaton, and L. Venkataraman, *Mechanically controlled binary conductance switching of a single-molecule junction.* Nature Nanotechnology, 2009. **4**(4): p. 230-234.

16.   J.S. Meisner, M. Kamenetska, M. Krikorian, M.L. Steigerwald, L. Venkataraman, and C. Nuckolls, *A Single-Molecule Potentiometer.* Nano Letters, 2011. **11**(4): p. 1575-1579.

17.   M. Elbing, R. Ochs, M. Koentopp, M. Fischer, C. von Hanisch, F. Weigend, F. Evers, H.B. Weber, and M. Mayor, *A single-molecule diode.* Proceedings of the National Academy of Sciences of the United States of America, 2005. **102**(25): p. 8815-8820.

18.   I. Díez-Pérez, J. Hihath, Y. Lee, L.P. Yu, L. Adamska, M.A. Kozhushner, I.I. Oleynik, and N.J. Tao, *Rectification and stability of a single molecular diode with controlled orientation.* Nature Chemistry, 2009. **1**(8): p. 635-641.

19.   S.K. Yee, J.B. Sun, P. Darancet, T.D. Tilley, A. Majumdar, J.B. Neaton, and R.A. Segalman, *Inverse Rectification in Donor-Acceptor Molecular Heterojunctions.* Acs Nano, 2011. **5**(11): p. 9256-9263.

20.   H. Nakamura, Y. Asai, J. Hihath, C. Bruot, and N.J. Tao, *Switch of Conducting Orbital by Bias-Induced Electronic Contact Asymmetry in a Bipyrimidinyl-biphenyl Diblock Molecule: Mechanism to Achieve a pn Directional Molecular Diode.* Journal of Physical Chemistry C, 2011. **115**(40): p. 19931-19938.

21. R.M. Metzger, B. Chen, U. Hopfner, M.V. Lakshmikantham, D. Vuillaume, T. Kawai, X.L. Wu, H. Tachibana, T.V. Hughes, H. Sakurai, J.W. Baldwin, C. Hosch, M.P. Cava, L. Brehmer, and G.J. Ashwell, *Unimolecular electrical rectification in hexadecylquinolinium tricyanoquinodimethanide.* Journal of the American Chemical Society, 1997. **119**(43): p. 10455-10466.

22. L. Bartels, *Tailoring molecular layers at metal surfaces.* Nature Chemistry, 2010. **2**(2): p. 87-95.

23. D. Natelson, *Mechanical Break Junctions: Enormous Information in a Nanoscale Package.* ACS Nano, 2012. **6**(4): p. 2871-2876.

24. N. Agraït, A.L. Yeyati, and J.M. van Ruitenbeek, *Quantum properties of atomic-sized conductors.* Physics Reports, 2003. **377**(2-3): p. 81-279.

25. S. Datta, *Electronic transport in mesoscopic systems.* Cambridge studies in semiconductor physics and microelectronic engineering. 1995, New York: Cambridge University Press.

26. S. Karthauser, *Control of molecule-based transport for future molecular devices.* Journal of Physics-Condensed Matter, 2011. **23**(1).

27. H.B. Akkerman and B. de Boer, *Electrical conduction through single molecules and self-assembled monolayers.* Journal of Physics: Condensed Matter, 2008. **20**(1): p. 013001.

28. R.A. Webb, S. Washburn, C.P. Umbach, and R.B. Laibowitz, *Observation of h/e Aharonov-Bohm Oscillations in Normal-Metal Rings.* Physical Review Letters, 1985. **54**(25): p. 2696-2699.

29. G.C. Solomon, C. Herrmann, T. Hansen, V. Mujica, and M.A. Ratner, *Exploring local currents in molecular junctions.* Nat Chem, 2010. **2**(3): p. 223-228.

30. G.C. Solomon, D.Q. Andrews, T. Hansen, R.H. Goldsmith, M.R. Wasielewski, R.P.V. Duyne, and M.A. Ratner, *Understanding quantum interference in coherent molecular conduction.* Journal of Chemical Physics, 2008. **129**(5): p. 054701.

31. P. Sautet and C. Joachim, *Electronic Interference Produced by a Benzene Embedded in a Polyacetylene Chain.* Chemical Physics Letters, 1988. **153**(6): p. 511-516.

32. R. Baer and D. Neuhauser, *Phase coherent electronics: A molecular switch based on quantum interference.* Journal of the American Chemical Society, 2002. **124**(16): p. 4200-4201.

33. D.M. Cardamone, C.A. Stafford, and S. Mazumdar, *Controlling quantum transport through a single molecule.* Nano Letters, 2006. **6**(11): p. 2422-2426.

34. S.-H. Ke, W. Yang, and H.U. Baranger, *Quantum-Interference-Controlled Molecular Electronics.* Nano Letters, 2008. **8**(10): p. 3257-3261.

35. T. Markussen, R. Stadler, and K.S. Thygesen, *The Relation between Structure and Quantum Interference in Single Molecule Junctions.* Nano Letters, 2010. **10**(10): p. 4260-4265.

36. R. Stadler, M. Forshaw, and C. Joachim, *Modulation of electron transmission for molecular data storage.* Nanotechnology, 2003. **14**(2): p. 138-142.

37. C.M. Guédon, H. Valkenier, T. Markussen, K.S. Thygesen, J.C. Hummelen, and S.J. van der Molen, *Observation of quantum interference in molecular charge transport.* Nature Nanotechnology, 2012. **7**(5): p. 305-9.

38. X.D. Cui, A. Primak, X. Zarate, J. Tomfohr, O.F. Sankey, A.L. Moore, T.A. Moore, D. Gust, G. Harris, and S.M. Lindsay, *Reproducible measurement of single-molecule conductivity.* Science, 2001. **294**(5542): p. 571-574.

39. H. Ohnishi, Y. Kondo, and K. Takayanagi, *Quantized conductance through individual rows of suspended gold atoms.* Nature, 1998. **395**(6704): p. 780-783.

40. G. Rubio, N. Agraït, and S. Vieira, *Atomic-Sized Metallic Contacts: Mechanical Properties and Electronic Transport.* Physical Review Letters, 1996. **76**(13): p. 2302-2305.

41. F.J. Giessibl, *Atomic resolution on Si(111)-(7x7) by noncontact atomic force microscopy with a force sensor based on a quartz tuning fork.* Applied Physics Letters, 2000. **76**(11): p. 1470-1472.

42. M. Ternes, C. Gonzalez, C.P. Lutz, P. Hapala, F.J. Giessibl, P. Jelinek, and A.J. Heinrich, *Interplay of Conductance, Force, and Structural Change in Metallic Point Contacts.* Physical Review Letters, 2011. **106**(1): p. 016802.

43. M. Ternes, C.P. Lutz, C.F. Hirjibehedin, F.J. Giessibl, and A.J. Heinrich, *The Force Needed to Move an Atom on a Surface.* Science, 2008. **319**(5866): p. 1066-1069.

44. J. Welker and F.J. Giessibl, *Revealing the Angular Symmetry of Chemical Bonds by Atomic Force Microscopy.* Science, 2012. **336**(6080): p. 444-449.

45. C. Wagner, N. Fournier, F.S. Tautz, and R. Temirov, *Measurement of the Binding Energies of the Organic-Metal Perylene-Teracarboxylic-Dianhydride/Au(111) Bonds by Molecular Manipulation Using an Atomic Force Microscope.* Physical Review Letters, 2012. **109**(7): p. 076102.

46. N. Fournier, C. Wagner, C. Weiss, R. Temirov, and F.S. Tautz, *Force-controlled lifting of molecular wires.* Physical Review B, 2011. **84**(3): p. 035435.

47. H. Nadine, M. Fabian, G. Leo, M. Gerhard, F. Thomas, and B. Richard, *Force and conductance during contact formation to a C 60 molecule.* New Journal of Physics, 2012. **14**(7): p. 073032.

48. J.E. Sader, T. Uchihashi, M.J. Higgins, A. Farrell, Y. Nakayama, and S.P. Jarvis, *Quantitative force measurements using frequency modulation atomic force microscopy - theoretical foundations.* Nanotechnology, 2005. **16**(3): p. S94-S101.

49. B.Q. Xu, X.Y. Xiao, and N.J. Tao, *Measurements of single-molecule electromechanical properties.* Journal of the American Chemical Society, 2003. **125**(52): p. 16164-16165.

50. M. Frei, *Force and Conductance Spectroscopy of Single Molecule Junctions (Ph.D. Thesis)*, 2012, Columbia University: United States -- New York.

51. A. Borgia, P.M. Williams, and J. Clarke, *Single-molecule studies of protein folding.* Annual Review of Biochemistry, 2008. **77**: p. 101-125.

52. T.E. Fisher, P.E. Marszalek, and J.M. Fernandez, *Stretching single molecules into novel conformations using the atomic force microscope.* Nature Structural Biology, 2000. **7**(9): p. 719-724.

53. H. Vázquez, R. Skouta, S. Schneebeli, M. Kamenetska, R. Breslow, L. Venkataraman, and M.S. Hybertsen, *Probing the conductance superposition law in single-molecule circuits with parallel paths.* Nature Nanotechnology, 2012. **7**(10): p. 663-667.

54. M. Ruben, A. Landa, E. Lörtscher, H. Riel, M. Mayor, H. Görls, H.B. Weber, A. Arnold, and F. Evers, *Charge Transport Through a Cardan-Joint Molecule.* Small, 2008. **4**(12): p. 2229-2235.

55. I. Franco, C.B. George, G.C. Solomon, G.C. Schatz, and M.A. Ratner, *Mechanically Activated Molecular Switch through Single-Molecule Pulling.* Journal of the American Chemical Society, 2011. **133**(7): p. 2242-2249.

56. V.P. Ilya, M. Gábor, Y. Koji, M. Artem, G. Murat, R.B. Martin, and W. Thomas, *An approach to measure electromechanical properties of atomic and molecular junctions.* Journal of Physics: Condensed Matter, 2012. **24**(16): p. 164210.

57. J.F. Zhou, C.L. Guo, and B.Q. Xu, *Electron transport properties of single molecular junctions under mechanical modulations.* Journal of Physics-Condensed Matter, 2012. **24**(16).

58. C. Nef, P.L.T.M. Frederix, J. Brunner, C. Schonenberger, and M. Calame, *Force-conductance correlation in individual molecular junctions.* Nanotechnology, 2012. **23**(36).

2

Experimental procedures and analysis techniques

One of the challenges in the study of single atomic contacts and single-molecule junctions is to form nanometer size contacts and gaps with metallic electrodes. Conventional microfabrication techniques are unable to achieve such gaps, and require special methods such as controlled electromigration which have low device yields. In our experimental work we use the 'break junction' technique employing either a scanning tunneling microscope (STM) or a conducting atomic force microscope (AFM), where junctions are repeatedly formed and broken thousands of times in the course of a typical experiment. This chapter describes the experimental protocols used to carry out these measurements, and the analysis techniques we have developed to perform statistical analyses of large datasets.

2.1   STM- and AFM-based break junction setups

We utilize the break-junction technique to perform experimental studies of atomic-scale contacts[1, 2]. In this technique, two metallic electrodes are repeatedly brought into and out of contact with each other. Upon complete rupture of the junction, a gap on the order of ~1 nanometer opens up in the case of gold electrodes due to atomic relaxation[3]. This gap is ideally suited to measure single-molecule conductance with molecules that are terminated with chemical groups, thereby spontaneously forming junctions by binding to the Au electrodes on either ends. The STM-based break junction (STM-BJ) setup[1, 4] (Figure 2.1a) consists of a freshly cut Au wire held in a home-built tip holder, that is brought into and out of contact with an Au substrate. The substrates are mica sheets with ~100 nm of evaporated gold (99.9999% pure, from Alfa Aesar). Before every experiment, we clean the cantilever and substrate in a UV/ozone cleaner.

Whereas the Au wire used in STM experiments represents, effectively, an infinitely stiff cantilever, AFM break junction (AFM-BJ, Figure 2.1b) measurements necessitate the use of
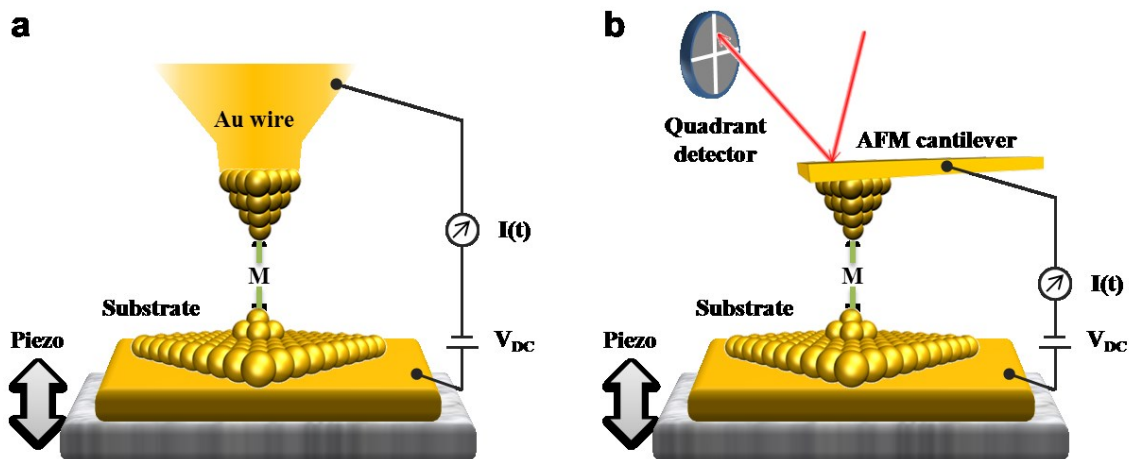
Figure 2.1. Schematic representations of the experimental setups. (a) STM-BJ setup for conductance-only measurements where a freshly cleaved Au wire forms one of the electrodes, while an Au-coated mica substrate is used as the second electrode. (b) AFM-BJ setup for simultaneous of force and conductance measurements, where an Au-coated AFM micro-cantilever acts as one of the electrodes.

finite stiffness probes[2, 5]. In terms of the force resolution in an optical beam deflection type AFM setup in the static mode AFM force spectroscopy, it is best to use the softest possible probes[6], since the deflection of the cantilever $\Delta x = \Delta F / k$, where ΔF is the change in force and K is the stiffness. However, we need stiff probes to perform break-junction measurements for two reasons: 1) To rupture Au-Au bonds in the experiment, the AFM cantilever needs to have a minimum stiffness corresponding to the stiffness of an Au-Au bond ($\sim$ 8N/m)[7], and 2) The thermal noise density (n_{th})of an AFM cantilever has the form:

$$n_{th} = \sqrt{\frac{2k_B T}{\pi f_0 k Q} \frac{1}{\left[1-(f/f_0)^2\right]^2 + f^2/(f_0 Q)^2}} \qquad \textbf{Eq. 2-1}$$

where, k_B is the Boltzmann constant, T is the temperature, f_0 is the resonant frequency, Q is the quality factor, and k is the spring constant of the cantilever and f is the frequency. Therefore, a stiffer cantilever with a high resonant frequency is required for the lowest force noise. In addition, previous molecular dynamics based theoretical simulations and experimental results by other researchers have also indicated that a stiff cantilever is better suited to measure the mechanics of atomic-scale junctions[7-9]. With these considerations, we therefore use commercial AFM cantilevers (NanoAndMore, Inc) of $\sim$ 50 N/m stiffness after coating with 35 nm of Cr and 120 nm of gold (99.9999% pure, from Alfa Aesar) through thermal evaporation (Edwards BOC/Auto 306). We have optimized our conducting AFM setup (modified from a commercial Veeco Multimode AFM) to obtain high force resolution. The modifications to the experimental setup include customized optics to maximize signal-to-noise ratio, using a temperature controlled superluminescent diode as an incoherent light source and many

modifications to the AFM to decouple it from external mechanical and acoustic noise sources. The details of the experimental setup have been presented elsewhere[10].

In both the STM- and AFM-based break junction setup, we apply a bias voltage (V_{dc}, typically 25 mV but higher for low conducting molecules) across the Au tip and substrate and the current flowing across the junction is measured using a current amplifier (Kiethly 428). We use a calibrated single-axis piezoelectric positioner (Mad City Labs) which is calibrated by the manufacturer as well as independently by us using laser interference measurements to be accurate within 5%. We use a high resolution 24-bit data acquisition card (National Instruments, PXI-4461) operating at upwards of 40,000 samples/sec to collect the current data and to control the piezo. Finally, we collect the force data using a 16-bit data acquisition card (National Instruments PXI-6251) after low-pass filtering at 10 kHz followed by summing and amplifying using commercial data processing modules (SRS).

2.2 AFM cantilever calibrations

We obtain force data by measuring the deflection of a focused laser beam off the back of the AFM cantilever. This beam is collected on a quadrant detector and the voltage signal is converted into a force reading in two steps:

1) We obtain the voltage signal during a 200 nm motion of the cantilever in hard contact with the substrate. Since we know the piezo displacement, we can calculate the conversion factor for the voltage signal to cantilever displacement.

2) We measure the power spectrum of the free cantilever displacement. The area using a Lorentzian fit to the thermal power spectrum provides a measure of the mean displacement

$\sqrt{<x^2>}$ of the oscillator. From the equipartition theorem, the spring constant/stiffness of the cantilever is calculated as[6]:

$$k_{cant} = k_B T / <x^2>$$
Eq. 2-2

2.3 Measurement protocols

We start each measurement by contacting the tip (STM Au wire or Au-coated AFM cantilever) to the substrate to achieve a conductance larger than 5 G_0 ($G_0 = 2$ e^2/h, the quantum of conductance). This ensures that we sample a wide variety of junction structures in our measurements. From this position, we pull the substrate away from the AFM tip at the rate of 18 nm/s. During this retraction, we either measure the current (STM-BJ) or we simultaneously measure the current and force (AFM-BJ). Knowing the applied bias voltage (V) and the current (I), the conductance ($G=I/V$) of the junction is monitored as a function of piezo displacement. Figure 2.2 shows sample simultaneously measured conductance (red) and force (blue) traces with a clean Au substrate using the AFM-BJ setup. Experiments with the STM-BJ are qualitatively identical, however, only the conductance can be measured in that case. The conductance trace shows steps/plateaus in conductance close to integer multiples of G_0, highlighting the quantized conductance in Au atomic-size junctions described by the Landauer-Buttiker formalism (Eq. 1–2). Beyond the 1 G_0 plateau corresponding to the Au single atomic point contact, the junction ruptures and conductance falls to the noise levels of the instrument (inset of Figure 2.2). At the same time well-correlated saw-tooth features are observed in the force data: conductance plateaus correspond to ramps in force, indicating tensile loading of the
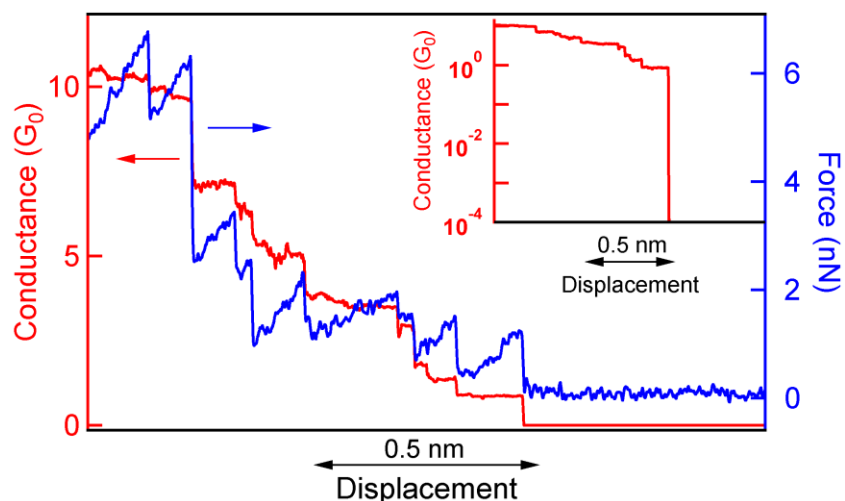
Figure 2.2. Sample simultaneously measured conductance and force trace for Au point contact. Conductance (red, left axis) and force (blue, right axis) data show the evolution and rupture of an Au point contact as a function of the displacement of the substrate. Inset: conductance data plotted on a logarithmic axis to make the conductance noise level visible.

junction and drops in conductance correspond to drops in force, indicating junction rearrangement or bond rupture events in the junction.

Molecules of interest can be deposited onto the substrate either by evaporating small quantities of the molecule, or by deposition of a drop of dilute (~ 1 mMol) solution of the molecule dissolved in a suitable solvent (typically 1,2,4-trichlorobenzene). In the presence of molecules with chemical linkers that bind to the Au electrodes, additional conductance features are observed below 1 G_0. Figure 2.3 shows a sample simultaneously measured conductance (plotted on a logarithmic axis, red) and force data (blue) in the presence of 1,4 - bis(methylsulfide) butane (**C4SMe**), which is a saturated four-atom carbon chain with methylsulfide (-S-CH$_3$) linkers[11] (chemical structure shown in the inset). The force data shows multiple saw-tooth features during the molecular conductance plateau. After the molecular junction is extended for ~ 0.3 nm, the junction ruptures completely and no further features are observed in the force and conductance within the instrumental noise.
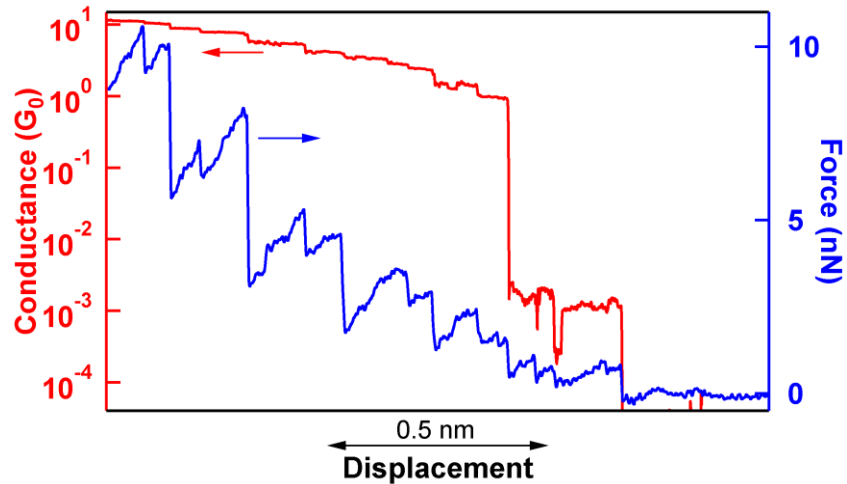
Figure 2.3. Sample simultaneously measured conductance and force trace for a single-molecule junction. In addition to conductance (red, left axis) plateaus near integers of G_0, additional conductance plateau is seen at $\sim 10^{-3}$ G_0 due to the formation of a single-molecule junction with **C4SMe** molecule. Force data (blue, right axis) show a clear saw-tooth features over the molecular conductance plateau. Inset: chemical structure of the molecule (grey – carbon, yellow – sulfur, and white – hydrogen.

2.4 One-dimensional histograms for conductance analysis

The sample traces shown in Figure 2.2 and Figure 2.3 represent particular junction evolution scenarios. When the experiment is repeated a different junction evolution might occur, due to inevitable microscopic differences at the atomic-scale. Therefore, in all our experiments, we measure thousands of individual traces and perform analyses of these large datasets to obtain statistically meaningful results. One of the most basic and powerful statistical analysis tools for conductance that has been widely used in atomic point contact and single-molecule experiments is the 1D conductance histogram[12]. In this technique, the conductance values are divided into either equally spaced bins, resulting in 'linearly binned histograms' or divided into logarithmically spaced bind, resulting in 'logarithmically binned histograms'. All the analyses are performed using custom programs written in the Wavemetrics Igor Pro software. Figure 2.4a,b shows 1D histograms constructed from 3000 traces each with clean Au and with **C4SMe** evaporated on the Au substrate using linear binning and logarithmic binning, respectively. Peaks

at quantized conductance values appear in the case of Au, where as a clear peak corresponding to the molecule appears at ~10^{-3} G_0 when **C4SMe** is present on the substrate. The logarithmic binning accentuates low conductance values, as seen in Figure 2.4b. Gaussian or Lorentzian lineshapes can then be fit to the molecular conductance features to extract the most frequently occurring conductance from either the linearly or logarithmically binned histograms.
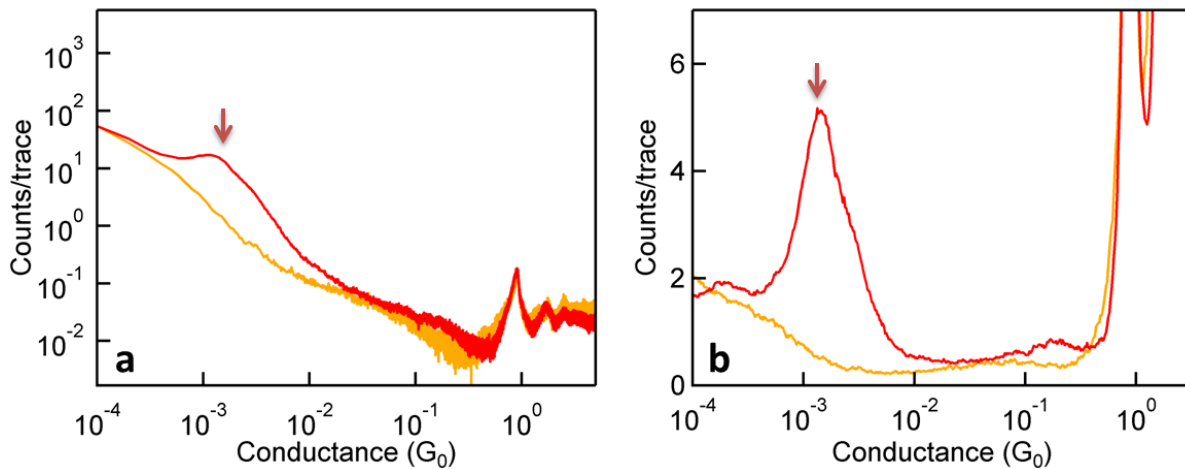
Figure 2.4. 1D conductance histograms. (a) Linearly binned (conductance bin size of 10^{-4} G_0) histograms for clean Au (yellow) and **C4SMe** (red). Note the logarithmic plotting for both axis. (b) Logarithmically binned (100 bins/decade) histograms for clean Au (yellow) and **C4SMe** (red). The arrows indicate the most frequently occuring conductance value corresponding to Au-**C4SMe**-Au single-molecule junctions.

2.5   Two-dimensional histograms for conductance and force analysis

While the 1D conductance histograms provide a way to obtain a statistical value for the conductance features, the displacement information present in the experimentally acquired conductance data is lost in the histograms. To extract statistically significant characteristics from the evolution of junction conductance and force as a function of sample displacement, we construct two-dimensional (2D) histograms from the conductance and force traces, setting the origin of the displacement axis at the point where either the 1 G_0 conductance step or the

molecular conductance step breaks. This well-defined position on the x-axis is determined individually for each trace, using an automated algorithm. A fraction of the traces do not show a conductance plateau at G_0 or a plateau corresponding to a molecular junction. It is likely that the absence of the G_0 or the molecular conductance plateau means that a single-atom point contact or a single molecule junction was not formed during that particular measurement. Therefore, these traces are not used for further analysis, as they do not contain the bond rupture event of interest. The statistical occurrence of the junction of interest varies with the case, but a statistically significant and unbiased data set results in each case. Each data point on the digitized conductance (force) trace is thus assigned a conductance (force) coordinate (along the y-axis) and a position coordinate (along the x-axis). Two-dimensional conductance histograms are then generated without further analysis. For the two-dimensional force histogram, we also set the force at the new zero-displacement position to zero force by subtracting an offset from the entire force trace. This realigns all force traces to a common point such that each force and displacement value was now determined relative to the value at the end of the conductance step in each trace. After this realignment, thousands of force traces were added to generate a two-dimensional force histogram. We then obtain a statistically averaged force profile from this histogram by locating the peaks of Gaussian fits to vertical sections at every displacement bin.

Figure 2.5a,b shows two-dimensional conductance and force histograms, respectively, constructed from over 31,000 traces measured without any molecules present and using 20 different tip/sample pairs. Insets to Figure 2.5a,b show a sample conductance and simultaneously acquired force trace, respectively, to illustrate where the zero in displacement is set. The conductance is plotted on a logarithmic axis, whereas the force and the position (x-) axes use
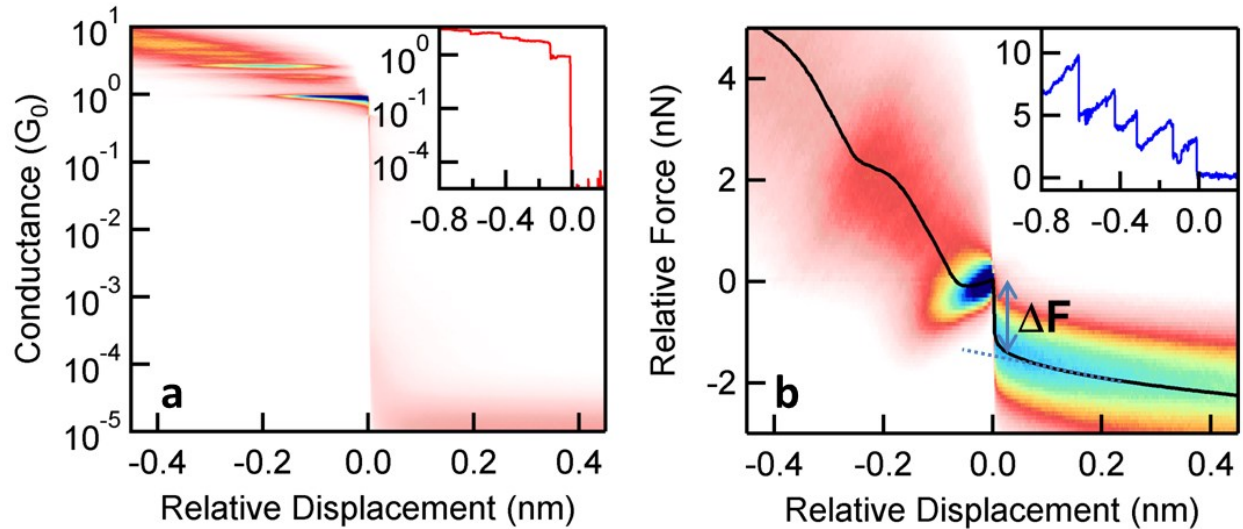
Figure 2.5. Statistical two-dimensional histograms for Au. (a) Two-dimensional conductance histogram constructed from over 31,000 traces. All traces are aligned such that the end of the plateau at 1 G_0 is at zero along the displacement axis. A large number of counts is visible at integer multiples of G_0. Inset: Sample conductance trace aligned to zero displacement at the end of the 1 G_0 plateau. (b) Two-dimensional force histogram constructed from simultaneously acquired force traces. The force profile (black curve) is overlaid and shows a clear jump at zero displacement. The rupture force of 1.4 nN for a single atomic contact is determined by extrapolating the fit of the force profile (dotted line). Inset: Force trace acquired simultaneously with conductance trace shown in the inset to panel (a), aligned at the 1 G_0 break.

linear bins in these plots. Negative displacements are events that occur before the end of the 1 G_0 plateau while positive corresponds to data beyond the end of the plateau. These histograms are generated from traces where the G_0 step can be identified with our automated algorithm. Approximately 80% (31,033 out of 39,000) of the measured traces exhibit a clearly identifiable 1 G_0 step and are included. Figure 2.5a shows clear peaks at integer multiples of G_0 occurring at negative displacements, and almost no counts at positive displacements, since zero displacement is set at the point when the G_0 contact breaks.

The 2D force histogram, created from the same set of traces, (Figure 2.5b) shows a trend in the force that is increasing with increasing displacement, just prior to the clear sharp drop at zero displacement. The force required to break the G_0 contact can be determined from the magnitude

of this drop. The force profile is effectively an averaged force trace for the single atom contact rupture event. It shows a clearly defined drop of 1.4 ± 0.2 nN at zero displacement, as illustrated in Figure 2.5b, corresponding to the breaking force of a single Au-Au bond. This value is in good agreement with published experimental and theoretical results[7, 9, 13], validating our 2D analysis method. We note here that this result is from a statistically significant data set of about 31,000 traces, providing a robust and unbiased determination of the Au single atomic contact rupture force.

We have also extended the 2D conductance and force histogram technique to a variety of single molecule junctions (Figure 2.6) consisting of different chemical backbones[14] and linker groups[15, 16]. Here we present a brief summary of the measured rupture forces and conductances measured for six molecules representing (a) four different molecular backbones (butane, hexane, benzene and bipyridine), each with a nitrogen termination, and (b) three linker groups (Amine [NH$_2$], thiomethyl [SMe], and diphenylphosphine [DPP]), each attached to
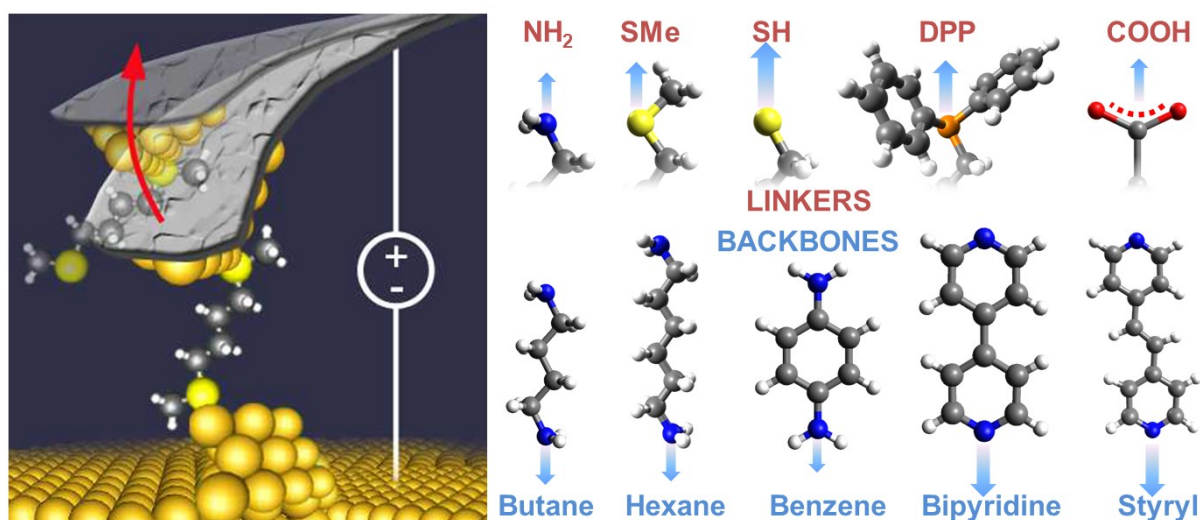
Figure 2.6. Experimental measurement scheme and chemical structures explored. On the left is an illustration of the stretching and breaking of a single molecule junction between the AFM cantilever and the substrate. Chemical structure of the linker groups and molecular backbones measured in this study are shown along with arrows of size proportional to their respective measured rupture forces.

similar saturated backbones (of 4-6 carbon atoms). The chemical names (and abbreviations used in the following discussion) for the molecules are: (a) 1,4 diaminobenzene (**BDA**), (b) 4,4' bipyridine (**BP**), (c) 1,6-hexanediamine (**C6A**), (d) 1,4-butanediamine (**C4A**) (e) 1,4-bis(methylsulfide) butane (**C4SMe**), and (f) 1,5 bis-(diphenyl-phosphino)pentane (**C5DPP**). Each compound is obtained from commercial sources, and used without further purification. Conductance is determined by measuring current through the junction at a constant applied bias of 25 mV for all molecules, except 75 mV for **C6A** and for **BP**. The molecules are deposited onto the Au substrate either by evaporation or by addition of a dilute concentration of molecule in the solvent 1,2,4-tricholorobenzene (**TCB**). Both the conductance and force results are independent of the deposition method. Over 10,000 individual conductance and simultaneously acquired force traces are collected with multiple tip/sample pairs for each molecule and are analyzed to generate 2D histograms in order to characterize their molecular breaking force.

As an example, Figure 2.7a shows a 2D conductance histogram for **C4A** where the origin in the displacement axis is set at the end of the molecular conductance step. Logarithmic bins for the conductance (y) axis and linear bins for the displacement (x) axis are chosen for image clarity. The measured traces that show a molecular conductance step were selected using an automated algorithm for both conductance and force analysis. Insets of Figure 2.7a,b show conductance and simultaneous force data for one particular junction breaking event, out of the over 3500 individual measurements used to construct the 2D histograms. A clear feature is seen in the conductance histogram at 9×10^{-4} G_0, which gives us the most probable conductance of an Au-**C4A**-Au junction. This peak extends over a displacement of about 0.15 nm, indicating that molecular junctions can be elongated over this distance prior to the final rupture. From Figure 2.7b, we obtain the most frequently occurring rupture force for **C4A** to be 0.6 nN.
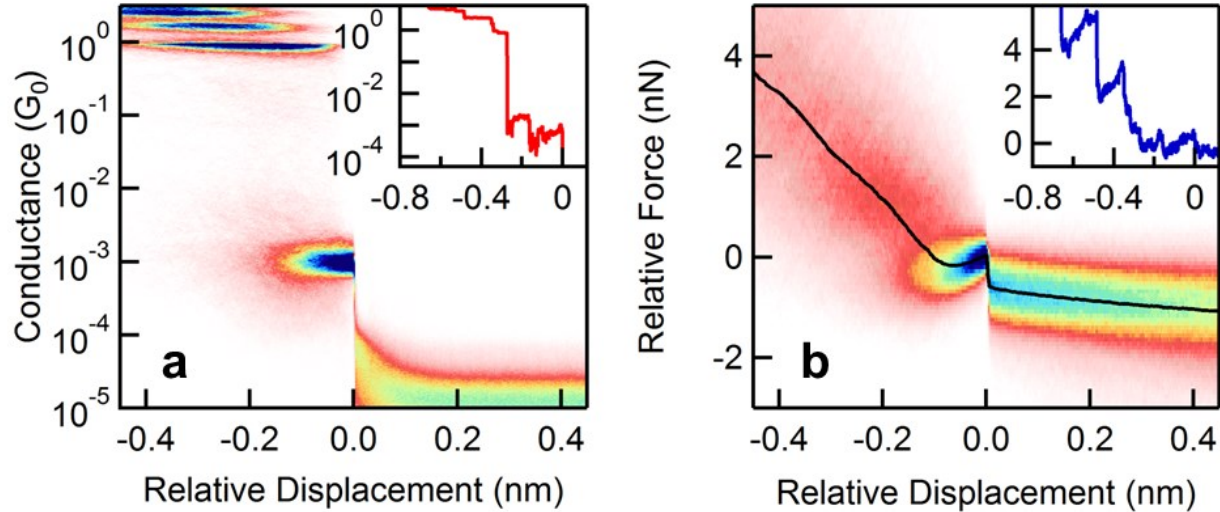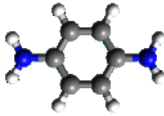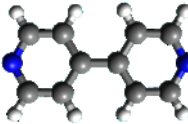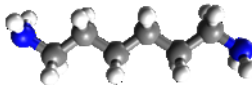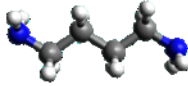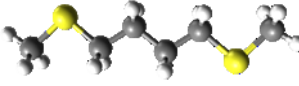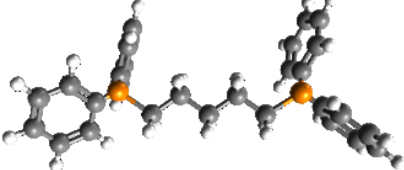
Figure 2.7. Statistical two-dimensional histograms for C4A. (a) Two-dimensional conductance histogram of **C4A** constructed from over 3,500 traces with a molecular conductance step. Features representing a sequence of Au contacts appear at integer multiples of G_0. A molecular signature can be clearly seen at 9×10^{-4} G_0. Inset: A sample conductance trace showing a G_0 and molecular plateau with zero displacement set to the end of the molecular plateau. (b) The two-dimensional force histogram for **C4A** is constructed from the simultaneously acquired force traces of the same set of traces used to construct the conductance histogram. The average force profile (black curve) shows a clear drop at zero-displacement of ~0.6 nN. Inset: Simultaneously acquired force trace aligned after the molecular step.

Each of these six molecules shows characteristic conductance features due to the selective binding of the N, SMe or DPP linker to undercoordinated Au atoms[4, 11]. Particularly, **BP** shows two characteristic conductance peaks (a 'high-G' and a 'low-G' peak) that occur at distinct junction elongation distances[17-19]. In this work, we probe the rupture from the low-G peak, which corresponds to a geometry where the molecule bridges the two Au electrodes vertically[19]. We note that the conductance peak positions (corresponding to the most frequently measured conductance, see Table 2.1) are in good agreement with previously published data collected in solution using the STM-based break junction technique[11, 19]. Furthermore, the clear conductance signature seen for all these molecules allows us to measure specific single Au-molecule-Au junction rupture events unambiguously. In each case, except the thiolate (SH) linker, it is also known that the binding mechanism is the (N, P or S)-Au donor-acceptor interaction[4, 11, 19-22]. In Table 2.1, we show bond rupture forces determined from

2D force histograms for all the six molecules. We see that in all these cases, the Au-molecule-Au junction ruptures at a force smaller than that of an Au-Au bond, indicating that rupture occurs at the respective donor-acceptor bonds consistent with earlier work[2, 11, 22]. Specifically in the amine linked molecules, by comparing the measured rupture forces for **C4A** and **C6A** we see first that for these two alkanes with 4 and 6 carbons in the backbone, the rupture forces are very similar. Additionally, we see that the force required to break the N-Au bond in the conjugated molecule, **BDA**, is considerably smaller than in **C4A** and **C6A**, which are fully saturated.

Table 2.1. Comparison of most frequently measured conductance and rupture force for molecular junctions with a nitrogen termination having different backbones (rows 1-4) and saturated backbones having different linker groups (rows 4-6).

#	Molecule	Chemical Structure	Conductance (G_0)	Force (nN)
1	1,4 benzenediamine (**BDA**)		6×10^{-3}	0.5
2	4,4' bipyridine (**BP**)		1×10^{-4}	0.8
3	1,6 hexanediamine (**C6A**)		1×10^{-4}	0.6
4	1,4 butanediamine (**C4A**)		9×10^{-4}	0.6
5	1,4-bis(methylsulfide) butane (**C4SMe**)		1×10^{-3}	0.7
6	1,5 bis-(diphenyl-phosphino)-pentane (**C5DPP**)		7×10^{-4}	0.8

2.6 Trace-by-trace analysis of conductance and force

In addition to 2D histograms, it is desirable to also obtain detailed statistical distributions of rupture force, stiffness and conductance on a trace-by-trace basis in order to estimate both the most frequently occurring values as well as their variance in our experiments. While this strategy is straight-forward, it is challenging to implement in the analyses of experimental datasets due to the presence of noise and the large variability in the properties of interest from junction to junction. We have overcome these challenges in developing trace-by-trace analysis techniques due to two significant developments. First, having a good force resolution in the AFM-BJ setup is a crucial factor in revealing subtle structural rearrangements that is not obviously to glean from conductance data alone. For instance, in Figure 2.3 several force saw-tooth features are seen over the course of a single molecular conductance plateau. So far, such features were not accounted for in experimental studies present in the literature. Second, in addition to the information that can be gained about structural rearrangements, these force signatures also need to be taken into account to obtain reliable junction stiffness values, which contains critical mechanical information about the junction. Therefore, robust automated algorithms needed to be developed in order to take into account the structural rearrangement signatures in the experimental data.

To achieve this, we have created an algorithm (see Figure 2.8) that identifies structural rearrangement signatures in the force data and use it to compile statistically relevant datasets of rupture force, stiffness and rearrangement lengths. We start by finding the displacement where the conductance plateau of interest ruptures to noise levels. This point is then used as a datum for further force analysis. All significant force events before this point are identified by a subroutine that locates sharp and large force fluctuations. This procedure consists of separately analyzing
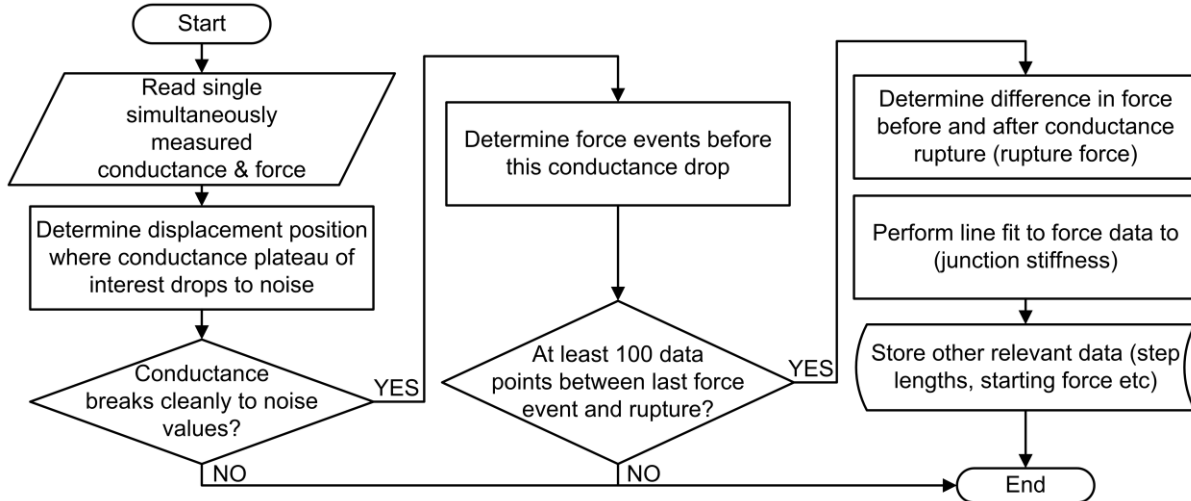
Figure 2.8. Flow chart explaining the algorithm to obtain rupture force and stiffness. This algorithm is geared towards identifying and accounting for subtle structural rearrangement events that are not observable through the analysis of the conductance data alone.

high and low pass filtered force data, and finding the locations at which sharp (large high frequency components) and large (large low frequency components) events occur coincidentally. Every force fluctuation above 0.25 nN, (~1.5× standard deviation of instrument noise) is identified in this manner. To be included in the results, we require that: a) the conductance beyond the plateau of interest drops to conductance noise levels to ensure that we are analyzing a junction rupture event, and b) the final load-rupture saw-tooth have at least 100 datapoints, to ensure meaningful fitting required in analyzing the stiffness. Each individual measurement satisfying these two criteria are included in the results and without any further selection. This ensures that there is no selection based on rupture force, stiffness or rearrangement length.

To demonstrate this analysis, we consider again the case of **C4SMe** single-molecule junction. In the conductance data (highlighted in Figure 2.9a, red, left axis), a clear molecular plateau around 10^{-3} G_0 is seen, and the rupture of the molecular junction is identified at a displacement of ~3.5 nm. The force data (highlighted in Figure 2.9b, blue, right axis) shows two fluctuations that are identified by the algorithm to be significantly larger than the instrument
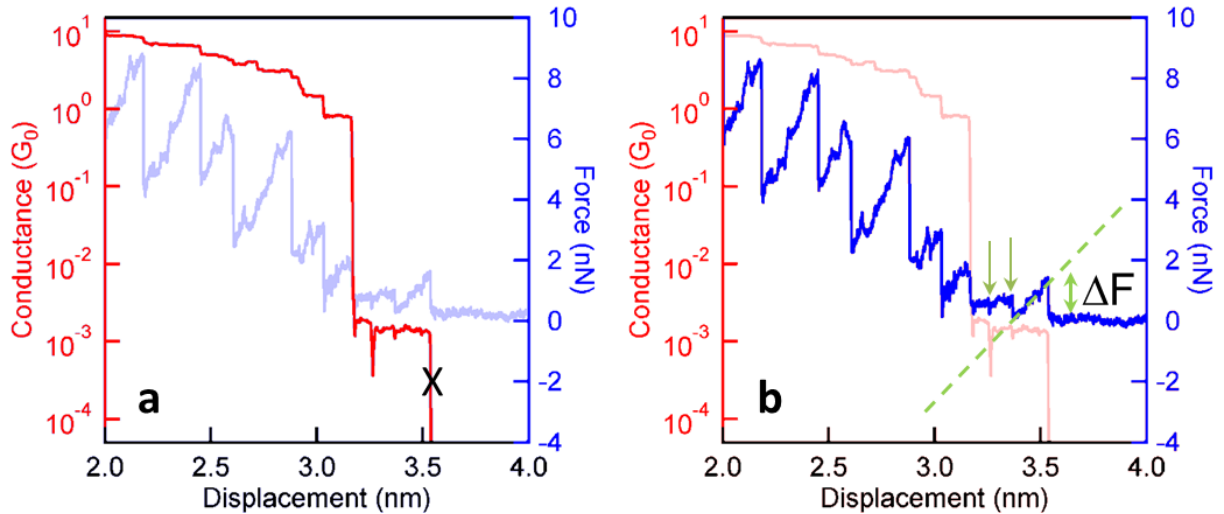
Figure 2.9. Sample C4SMe measurement demonstrating the trace-by-trace analysis algorithm. Simultaneously measured conductance (red, left axis) and force (blue, right axis) trace. (a) The conductance drop after the plateau of interest (here a **C4SMe** molecular conductance plateau) is located (shown by the X mark). (b) The algorithm then identifies significant force fluctuations beyond the experimental noise limit. These force events are not accounted for when extracting the stiffness of the junction using linear fitting to the force data (dashed green line). The rupture force is the drop in the force at the end of the conductance plateau.

noise (green downward arrows). Correlated with the conductance drop, a sharp drop is also observed in the force data. This drop in force (ΔF) is the junction rupture force. Finally, the force data between the rupture location and the force event that immediately precedes the rupture is fitted with a linear fit to obtain the slope (k_{raw}) of the force ramp. The stiffness of the junction (k_{junc}) is then obtained after correcting for AFM spring constant (k_{cant} ~50 nN) in series:

$$k_{junc} = (k_{cant} \times k_{raw}) / (k_{cant} - k_{raw})$$

Eq. 2-3

For each experimental dataset, we obtain the rupture force for clean gold samples, and perform a Gaussian fit to a histogram compiled from this force data. The combined errors in the measurements of the voltage-to-displacement factor and cantilever stiffness as well as known variability in detector sensitivity[23] manifest themselves in the mean value of the Au-Au rupture force[7]. We have rigorously characterized this value by compiling more than 10,000

individual Au rupture events (out of 39,000 measurements performed with multiple tips, substrates and calibrations) using the same algorithm described above. Figure 2.10 shows the histogram of these forces along with a Gaussian fit centered at 1.5 ± 0.02 nN (fitted mean $\pm$ standard error). With day-to-day changes in AFM tips, substrates and calibrations, we observe that the mean rupture force of Au G_0 is Gaussian distributed, but the mean varies by up to a maximum of $\pm 20\%$ of 1.5 nN. Therefore, we correct for these day-to-day calibration errors across datasets by using a single correction factor per dataset, such that the mean Au G_0 rupture force is set to the reference value of 1.5 nN. The absence of this correction does not affect the observed trends,
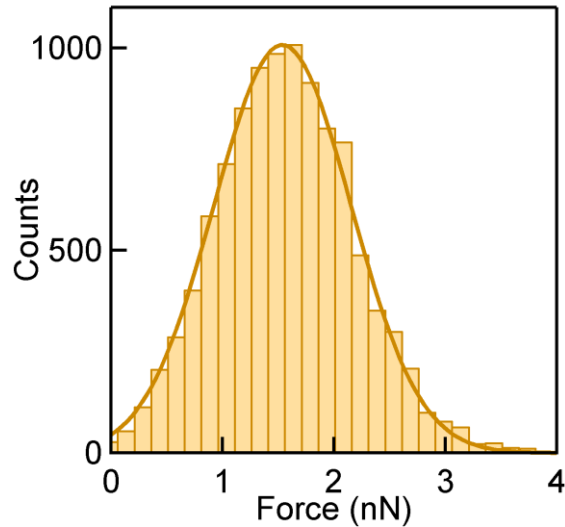
Figure 2.10. Rupture force distribution for Au-Au bond rupture. Histogram of Au G_0 rupture forces (compiled from more than 10,000 individual measurements) can be fitted to a Gaussian profile, and the most frequently measured value obtained is 1.5 ± 0.02 nN.

and its influence on the quantitative results is reduced due to averaging of multiple datasets. We note that the rupture force value obtained from this large dataset trace-by-trace analysis is 1.5 nN, whereas the value obtained from 2D analysis of similarly large dataset in Section 2.5 was 1.4 nN. This discrepancy (which is nonetheless within the experimental uncertainty of ± 0.2 nN of the 2D value) likely arises from the slight ambiguity in extracting the drop in the force of the statistically averaged force profile (Figure 2.5). While the most frequently measured rupture force is obtained on a trace-by-trace basis as the most frequently occurring value of the difference in two force values (*i.e.*, force values immediately before (F_{max}) and after (F_0)

rupture), the rupture force is obtained from the 2D force histogram is the average difference in these two values. These two values need not be equal in general:

$$< F_{max} - F_0 > \neq < F_{max} > - < F_0 >$$

<div align="right">**Eq. 2-4**</div>

2.7 Force analysis in the case of low- or non-conducting molecular junctions

A distinct advantage of single-molecule measurements using AFM-BJ is that the force data is collected independent of the conductance. Therefore, the force data can potentially be used as a complementary probe of junction evolution irrespective of the conductance. This ability is exploited in Chapter 4, in the study of molecules which do not show a measurable conductance due to destructive quantum interference in their electronic transport. The algorithm developed for this analysis performs three sequential operations on every individual simultaneously measured conductance and force traces: (1) identifying the location of the end of the 1 G_0 conductance plateau, (2) analyzing the force data beyond this point to find the last force event within 1 nm of this point and (3) setting the origin of conductance and force traces at this location and creating 2D histograms of force and conductance. Figure 2.11 demonstrates application of this technique on a sample individual elongation measurement of (*E*)-3,3′-di(methylthio)stilbene molecular junction that does not show an identifiable molecular conductance plateau, but the force events beyond the Au point contact rupture provide a clear indication of the presence of the molecule in the junction. The conductance drop from 1 G_0 is easily identified since the conductance decreases by more than two orders of magnitude upon the rupture of Au point-contacts. Analyzing the force data to identify significant events is carried out by the following procedure. First, the force trace *F* (Figure 2.11, blue trace) is transformed to a trace *F** (Figure 2.11, green trace) where every data point *F*[p]* with index *p* is defined as:

$$F*[p] = \sqrt{F[p]_{avg,10} \times F[p]_{avg,50}}$$ **Eq. 2-5**

where,

$$F_{avg,n}[p] = \frac{1}{n}\left(\sum_{i=p-n}^{p} F[i] - \sum_{j=p}^{p+n} F[j]\right)$$ **Eq. 2-6**
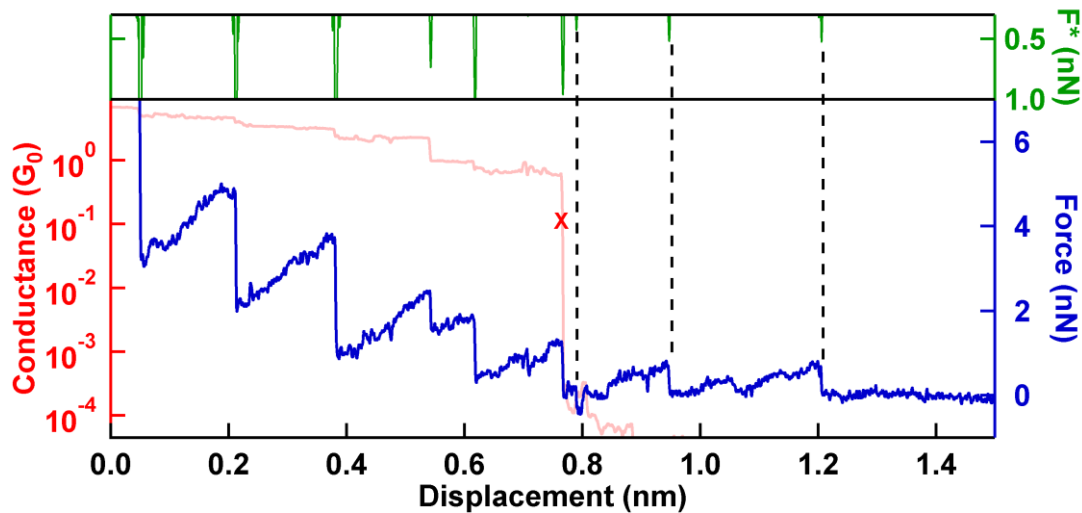
Figure 2.11. Sample trace demonstrating force-based analysis technique in a (*E*)-3,3'-di-(methylthio)stilbene single-molecule junction. The rupture from 1 G_0 is shown by the red ×. Dashed lines are provided as visual guides to the force events identified through *F**, the auxiliary force trace (green) within a 1 nm displacement from the 1 G_0 rupture location.

F* shows clearly defined spikes at the positions where there are large changes in the force, and is much less sensitive to random noise compared to the original data, due to the averaging. We note that due to high frequency noise in the raw force trace, a simple numerical derivative cannot reliably identify the location of these sharp drops in force. We classify every spike of *F** that corresponds to a change in force greater than 0.3 nN (which is ∼ 2× the experimental noise level of the force data) as a significant force event, and use this threshold to consistently analyze all data collected here for all three molecule types. *F** is used to identify all the significant force events within a 1 nm elongation beyond the 1 G_0 point-contact rupture. Figure 2.11 demonstrates

the high sensitivity of F^* to significant force events which are heuristically identified in the force data. It also demonstrates the insensitivity of F^* towards high frequency noise in the force data. The algorithm then identifies the last force event as the rupture of the molecular junction, irrespective of the conductance. Once identified, this molecular rupture location can be used as the origin to construct the displacement-preserving conductance and force 2D histogram centered at the rupture location of the molecular junction, as described before in Section 2.5, even though there is no identifiable molecular rupture location obtainable from the conductance data.

2.8   References

1.   B. Xu and N.J. Tao, *Measurement of Single-Molecule Resistance by Repeated Formation of Molecular Junctions.* Science, 2003. **301**(5637): p. 1221-1223.

2.   B.Q. Xu, X.Y. Xiao, and N.J. Tao, *Measurements of single-molecule electromechanical properties.* Journal of the American Chemical Society, 2003. **125**(52): p. 16164-16165.

3.   A.I. Yanson, G.R. Bollinger, H.E. van den Brom, N. Agrait, and J.M. van Ruitenbeek, *Formation and manipulation of a metallic wire of single gold atoms.* Nature, 1998. **395**(6704): p. 783-785.

4.   L. Venkataraman, J.E. Klare, I.W. Tam, C. Nuckolls, M.S. Hybertsen, and M.L. Steigerwald, *Single-molecule circuits with well-defined molecular conductance.* Nano Letters, 2006. **6**(3): p. 458-462.

5.   P.E. Marszalek, W.J. Greenleaf, H.B. Li, A.F. Oberhauser, and J.M. Fernandez, *Atomic force microscopy captures quantized plastic deformation in gold nanowires.* Proceedings of the National Academy of Sciences of the United States of America, 2000. **97**(12): p. 6282-6286.

6.   J.L. Hutter and J. Bechhoefer, *Calibration of Atomic-Force Microscope Tips.* Review of Scientific Instruments, 1993. **64**(7): p. 1868-1873.

7.   G. Rubio-Bollinger, S. Bahn, N. Agraït, K. Jacobsen, and S. Vieira, *Mechanical Properties and Formation Mechanisms of a Wire of Single Gold Atoms.* Physical Review Letters, 2001. **87**(2): p. 026101.

8.   M.R. Sørensen, M. Brandbyge, and K.W. Jacobsen, *Mechanical deformation of atomic-scale metallic contacts: Structure and mechanisms.* Physical Review B, 1998. **57**(6): p. 3283-3294.

9. G. Rubio, N. Agraït, and S. Vieira, *Atomic-Sized Metallic Contacts: Mechanical Properties and Electronic Transport.* Physical Review Letters, 1996. **76**(13): p. 2302-2305.

10. M. Frei, *Force and Conductance Spectroscopy of Single Molecule Junctions (Ph.D. Thesis)*, 2012, Columbia University: United States -- New York.

11. Y.S. Park, A.C. Whalley, M. Kamenetska, M.L. Steigerwald, M.S. Hybertsen, C. Nuckolls, and L. Venkataraman, *Contact chemistry and single-molecule conductance: A comparison of phosphines, methyl sulfides, and amines.* Journal of the American Chemical Society, 2007. **129**(51): p. 15768-15769.

12. N. Agraït, A.L. Yeyati, and J.M. van Ruitenbeek, *Quantum properties of atomic-sized conductors.* Physics Reports, 2003. **377**(2-3): p. 81-279.

13. F. Tavazza, L.E. Levine, and A.M. Chaka, *Elongation and breaking mechanisms of gold nanowires under a wide range of tensile conditions.* Journal of Applied Physics, 2009. **106**(4): p. 043522.

14. M. Frei, S.V. Aradhya, M. Koentopp, M.S. Hybertsen, and L. Venkataraman, *Mechanics and chemistry: single molecule bond rupture forces correlate with molecular backbone structure.* Nano Letters, 2011. **11**(4): p. 1518-1523.

15. M. Frei, S.V. Aradhya, M.S. Hybertsen, and L. Venkataraman, *Linker dependent bond rupture force measurements in single-molecule junctions.* Journal of the American Chemical Society, 2012. **134**(9): p. 4003-6.

16. S. Ahn, S.V. Aradhya, R.S. Klausen, B. Capozzi, X. Roy, M.L. Steigerwald, C. Nuckolls, and L. Venkataraman, *Electronic transport and mechanical stability of carboxyl linked single-molecule junctions.* Phys Chem Chem Phys, 2012. **14**(40): p. 13841-5.

17. E.S. Tam, J.J. Parks, W.W. Shum, Y.-W. Zhong, M.E.B. Santiago-Berríos, X. Zheng, W. Yang, G.K.L. Chan, H.c.D. Abruña, and D.C. Ralph, *Single-Molecule Conductance of Pyridine-Terminated Dithienylethene Switch Molecules.* ACS Nano, 2011. **5**(6): p. 5115-5123.

18. M. Kamenetska, S.Y. Quek, A.C. Whalley, M.L. Steigerwald, H.J. Choi, S.G. Louie, C. Nuckolls, M.S. Hybertsen, J.B. Neaton, and L. Venkataraman, *Conductance and Geometry of Pyridine-Linked Single-Molecule Junctions.* Journal of the American Chemical Society, 2010. **132**(19): p. 6817-6821.

19. S.Y. Quek, M. Kamenetska, M.L. Steigerwald, H.J. Choi, S.G. Louie, M.S. Hybertsen, J.B. Neaton, and L. Venkataraman, *Mechanically controlled binary conductance switching of a single-molecule junction.* Nature Nanotechnology, 2009. **4**(4): p. 230-234.

20. M.S. Hybertsen, L. Venkataraman, J.E. Klare, A.C. Whalley, M.L. Steigerwald, and C. Nuckolls, *Amine-linked single-molecule circuits: systematic trends across molecular families.* Journal of Physics-Condensed Matter, 2008. **20**(37).

21. R. Parameswaran, J.R. Widawsky, H. Vázquez, Y.S. Park, B.M. Boardman, C. Nuckolls, M.L. Steigerwald, M.S. Hybertsen, and L. Venkataraman, *Reliable Formation of Single Molecule Junctions with Air-Stable Diphenylphosphine Linkers.* Journal of Physical Chemistry Letters, 2010. **1**(14): p. 2114-2119.

22. M. Kamenetska, M. Koentopp, A. Whalley, Y. Park, M. Steigerwald, C. Nuckolls, M. Hybertsen, and L. Venkataraman, *Formation and Evolution of Single-Molecule Junctions.* Physical Review Letters, 2009. **102**(12): p. 126803.

23. J.H.G. Huisstede, B.D. van Rooijen, K.O. van der Werf, M.L. Bennink, and V. Subramaniam, *Dependence of silicon position-detector bandwidth on wavelength, power, and bias.* Optics Letters, 2006. **31**(5): p. 610-612.

3

Electronic transport and mechanical stability of carboxyl linked

single-molecule junctions

Nanoscale interfacial physical properties become a dominant factor in determining its various functionalities in single-molecule junctions. Mechanical information at these length scales can help address a multitude of properties regarding the interplay between structure, mechanics and electronics of these junctions. Here we characterize electron transport across Au-molecule-Au junctions of heterogeneous carboxyl and methylsulfide terminated saturated and conjugated molecules and find that the stability of the carboxyl binding is comparable to that of the methylsulfide linker. Further, we find that the binding occurs through the formation of COO^--Au bond. By establishing reliable, in-situ junction formation, these experiments provide a new approach to probe electronic properties of carboxyl groups at the single molecule level.

The work presented in this chapter was performed in collaboration with Dr. Seokhoon Ahn, Dr. Michael Steigerwald and members of Prof. Colin Nuckolls' group.

The development of molecular-scale electronics requires an understanding of the relationship between the structure and charge transport properties of single molecules[1-3]. A molecular junction consists of a molecule bound between two electrodes via terminal functional groups that provide both the electronic and mechanical links[4-7]. The measured conductance of the molecule depends not only on the molecular backbone structure, but also on the choices of the electrode metal and the chemical link group. Specifically, the link group directly affects the type and strength of the metal-molecule interaction, in addition to details such as steric effects. Together, the backbone and the linking groups control both the junction mechanics as well as the electronic level alignment between the metal and molecule[8, 9]. Many different chemical links have been used experimentally for attaching molecules to Au electrodes including thiols[5, 8, 10, 11], amines[12-14], methyl sulfides[6, 15], fullerenes[16], paracyclophanes[17] , phosphines[6, 18], cyanides[19], and covalent gold-carbon links[20, 21]. The links dictate the metal-molecule contact geometry, whose variation can result in significant changes in conductance from junction to junction, particularly if thiol links are used[11, 22, 23]. Although electronic measurements of alkanes terminated with carboxylic acid groups have been carried out[13], electronic and mechanical properties of conjugated systems have not been reported so far, despite the attractive chemical modification opportunities afforded by the COOH group[24, 25]. In part, this can be attributed to the practical challenges arising from the low solubility of dicarboxylic acids in most non-polar organic solvents as well as non-trivial adsorption behavior on gold surfaces[3].

Here, we overcome these challenges by studying compounds with one carboxylic link and one methyl sulfide (SMe) link; the SMe group has reliable molecular junction formation properties[6, 15]. We measure electronic and mechanical properties of saturated and conjugated molecules terminated with both COOH and SMe linkers. Through conductance measurements

across Au-molecule-Au junctions, we find that both SMe and COOH terminations are comparable in terms of their electronics. In addition, we find evidence of binding of the COOH group to gold through a carboxylate-gold (COO$^-$-Au) bond. Using an atomic force microscope, we also carry out single-molecule bond rupture measurements[26, 27]. We find that these asymmetrically terminated molecular junctions rupture at 0.6 ± 0.1 nN. This force is comparable to the bond rupture force of di-SMe terminated molecules[27, 28], which indicates that the bond between the acid group and gold electrodes is also mechanically comparable to the Au-SMe bond.

3.1 Systematic trends in conductance for saturated backbones

The molecules used in this study, (methylthio)acetic acid (**A1**) (Aldrich), 3-(methylthio)propionic acid (**A2**) (Alfa Aesar), 4-(methylsulfanyl)butanoic acid (**A3**) (Ryan Scientific), 4-(methylsulfanyl)pentanoic acid (**A4**) (Ryan Scientific), and 4-(methylthio)benzoic acid (**B1**) (Aldrich) were purchased and used without further purification. 1,4-bis(methylthio)benzene (**B2**) was synthesized by the procedure of Engman *et al.*[29, 30]. Methyl 4-(methylthio)benzoate (**B3**) was synthesized from 4-(methylthio)benzoic acid by the procedure of Ikeda *et al.*[31].

Molecular conductance measurements are carried out using a modified scanning tunneling microscope[5] where a gold tip (cleaved Au wire, 0.25 mm diameter, 99.998%, Alfa Aesar) and a gold coated mica substrate are brought in and out of contact in a 0.1 to 1 mM tetradecane solution of the target molecule (Figure 3.1a). The current between the tip and substrate is measured at an applied bias of 450 mV as a function of the relative tip/sample displacement to yield a conductance (current/voltage) versus displacement trace. When a clean Au contact is
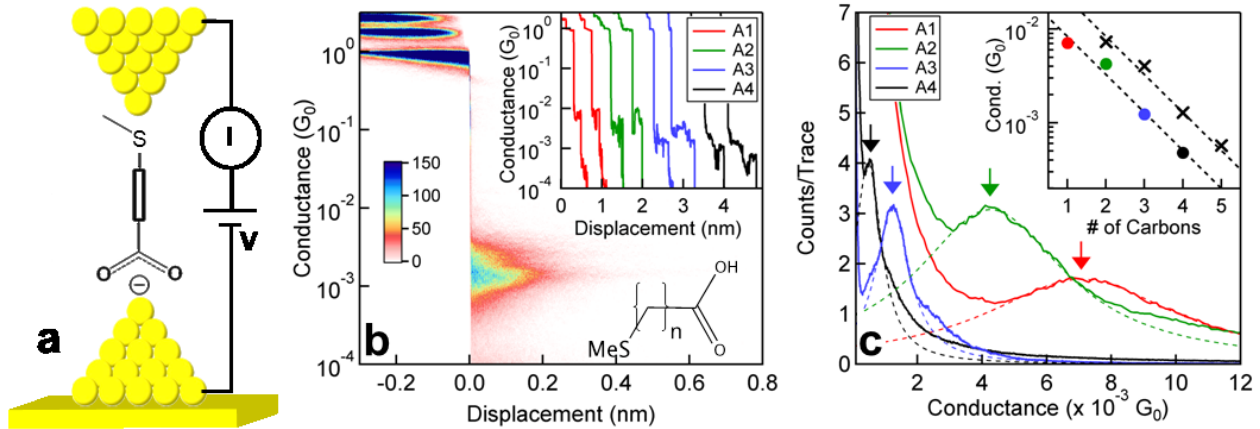
Figure 3.1. Conductance measurements of COOH/SMe terminated alkane molecules. (a) Schematic illustration of the Au-molecule-Au junction. (b) A 2D conductance-displacement histogram of compiled from over 10,000 individual **A3** traces measured at a bias of 450 mV. Inset: Sample conductance traces of molecules A1-A4. (c) 1D conductance histograms (linear bins, bin-size of 10^{-4} G_0 for **A1** and **A2**, and 10^{-5} G_0 for **A3** and **A4**). Inset: Semi-logarithmic plot of the variation of the most frequently measured conductance with the number of carbon atoms in the molecule (• = SMe/COOH linkers, × = SMe/SMe linkers).

pulled and broken, the conductance traces show steps at integral multiples of G_0 ($G_0 = 2e^2/h$, the quantum of conductance), indicating that the cross-section of the contact is reduced down to that of a few and, eventually, a single atomic chain of Au[32]. When the Au single atom chain is broken in the absence of molecules, the conductance either decreases exponentially with the electrode displacement due to tunneling across the gap between the two Au electrodes, or it drops from G_0 to below our experimental detection limit due to the broken ends of the electrode snapping back as the contacts relax[33, 34]. When measurements are carried out with a series of alkanes with 1-4 methylene groups terminated by a COOH group and a SMe group (**A1-A4**), conductance traces show additional plateaus at characteristic values lower than 1 G_0 (see Figure 3.1b inset). These plateaus are seen if the molecules present in the solution bridge the gap between the electrodes, with the terminal groups forming a bond to the Au electrodes, as illustrated in Figure 3.1a.

Figure 3.1b shows a two-dimensional conductance histogram[16, 35] created from 10,000 measurements with **A3**, where all traces are aligned along the displacement axis at the point where the single Au atom contact breaks. We see clear peaks at negative displacements with a conductance around 1, 2 and 3 G_0, characteristic of Au quantum point contacts. In addition, at positive displacements, we see a distinct conductance signature at around 10^{-3} G_0 indicating that molecular junctions are formed immediately following the rupture of the Au single-atom contact. This two-dimensional histogram also shows that these molecular conductance features extend to about 0.2 nm, in good agreement with previous measurements of alkanes terminated with amine or methyl sulfide groups[34]. The well-defined distribution of the conductance plateaus indicate that the carboxylic group binds selectively to under-coordinated Au atoms, again analogous to amine and methyl sulfide groups[6, 12]. These results together demonstrate that stable single molecule junctions can be reliably formed in-situ using carboxylic acid linkages.

The variation of conductance with the length of the molecule can reveal information about the electronic structure of the junction[2, 36, 37]. We quantify the trends in conductance systematically as a function of the number of methylene groups in the backbone by creating one-dimensional conductance histograms of all measured traces for each compound (Figure 3.1c). By fitting the molecular conductance feature in these histograms to a Lorentzian function, we determine the location of the peak in these histograms for each molecule. The peak positions correspond to the most frequently measured conductance of the respective molecule, and are observed to decrease with increasing molecular backbone length. These conductance values are plotted on a semi-logarithmic scale against the number of carbon atoms in each molecule in the inset of Figure 3.1c. We note that the number of carbon atoms counted does not include the carbon atom in the COOH group, therefore n=1 for **A1** and so on. From a linear fit to this data,

we find that the conductance for this series decreases exponentially with increasing molecular length ($G = R_c^{-1} e^{-\beta n}$), where G is the conductance, R_c is the contact resistance, n is the number of carbon atoms in the chain and β is the decay constant. We obtain a decay constant, β, of 0.9 ± 0.1/methylene group in good agreement with past measurements on a series of alkane molecules with a variety of terminal groups[5, 6, 11, 13, 38, 39]. The contact resistance (obtained by extrapolating this fit to zero carbon atoms) is 600 kΩ. For comparison, we include conductance values determined from measurements of alkanes terminated with SMe groups on both ends (×, inset of Figure 3.1c)[6]. Interestingly, we find that the conductance and conductance decay constant of this **An** series is almost the same as that of the SMe-$(CH_2)_n$-SMe compounds (which have a decay constant of 0.9 ± 0.1/methylene) if we consider that the **An** series has an extra carbon atom within the linker which does not participate in the bonding. Based on this consideration, the contact resistance of the bonding group becomes 240 kΩ (~ 600 × e$^{-0.9}$ kΩ), where the contact resistance of SMe-$(CH_2)_n$-SMe molecules is 270 kΩ[6]. From this, we infer that the electronic coupling between a COOH group and the Au electrode is similar to that of the SMe-Au linkage.

3.2 Conductance of aromatic backbones

Having established the reliable formation of molecular junctions with COOH linked alkane molecules, we now turn to aromatic systems that have long been known for enhanced electron transfer through solution-based experiments and Marcus-type electron transfer models[40]. We focus on the prototypical conjugated molecule, 4-(methylthio)benzoic acid (**B1**), with SMe and COOH links on opposite ends and measured in a tetradecane solution. The conductance histogram, generated using logarithmic bins, is shown in Figure 3.2 (brown trace). We see a

broad molecular conductance feature, indicating that the conductance of **B1** changes from junction to junction, and could depend on the orientation of the molecule in the junction[30]. Crucially, we find that the most frequently measured conductance for **B1** is 3× higher than the saturated **A4** molecule, despite its comparable length. This enhanced conductance clearly demonstrates the more efficient electron transport through the delocalized π-system, at the single molecule level. However, in comparison to its symmetrically linked analogue, **B2**
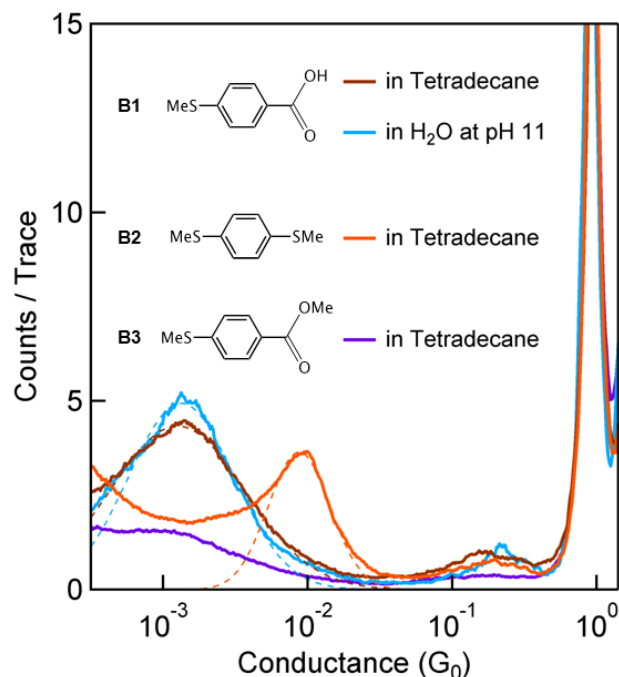
Figure 3.2. Conductance measurements with COOH/SMe terminated aromatic molecules. 1D conductance histograms (logarithmic bins, 100 bins/decade) of **B1** in tetradecane (brown) and in water at pH 11 (light blue), and of **B2** (orange) and **B3** (violet) in tetradecane. Measurements were carried out at an applied bias of 450 mV.

(orange trace in Figure 3.2), we note that the conductance of **B1** is smaller, indicating perhaps a reduced coupling due to the additional C atom between the phenyl ring and Au electrode.

3.3 Binding mechanism and mechanical stability of carboxyl linkers

We exploit the chemical modifications afforded by the carboxyl group to probe the binding mechanism between the acid group and the Au electrode. First, we perform the experiment in the presence of water at a pH of 11 (NaOH base). An apiezon wax coated Au tip is used to minimize the ionic current between the tip and substrate in the presence of the basic solution[41]. At pH 11, we see the clear molecular conductance feature at the same location ($\sim 1.3 \times 10^{-3}$ G_0) as the experiments performed in tetradecane (light blue trace in Figure 3.2). Considering the acidic

nature of **B1** (pK_a = 4.28), we expect the carboxyl group to be completely deprotonated at pH 11. Therefore, the absence of any changes in the conductance signature indicates that the molecule binds to the electrode through a COO⁻-Au bond[3, 13]. We also perform the experiment in an acidic solution (pH 1-3), but no identifiable conductance signature is observed. This could be due to the reduced solubility of **B1** in the strongly acidic solution or due to the fact that **B1** is not deprotonated in the low pH solution. To determine if the deprotonation is indeed necessary for bond formation, we perform conductance measurements of methyl 4-(methylthio)benzoate (**B3**), where the hydrogen of the carboxylic group is replaced with a methyl group. As indicated by Figure 3.2 (violet trace), we do not observe a clear conductance feature with **B3**. These measurements therefore indicate that the immobilized methyl group blocks the formation of molecular junctions, giving conclusive evidence for a COO⁻-Au binding mechanism. In addition, this result supports a binding mechanism based on COO⁻-Au bond through the negatively charged oxygen atoms, rather than C-Au interactions. This also provides the reason why the carbon atom of the carboxyl group appears to act like an additional atom in the tunneling equation for the alkane series, as discussed above.

In order to test the bond strength between **B1** and Au electrodes, we carry out simultaneous conductance and force measurements on single-molecule junctions following methods previously described in Frei *et al*.[26]. Briefly, we use a custom-built conductive atomic force microscope (AFM) and form single-molecule junctions between a gold-coated commercial AFM cantilever (NanoAndMore Inc) and a gold-on-mica substrate. Conductance is measured across the tip/sample junction at constant bias of 75 mV. The force is measured simultaneously by monitoring the deflection of a laser focused on the back of the cantilever. Figure 3.3a displays a sample conductance trace measured in a 1 mM tetradecane solution of **B1**, where we see the

characteristic conductance plateau around $\sim 10^{-3}$ G_0. Figure 3.3b reveals the simultaneously-measured force trace having a characteristic saw tooth pattern that is attributed to reversible (elastic) and irreversible (plastic) deformations during conductance plateaus and drops[42]. The conductance and force trace shown in the insets of Figure 3.3 have been offset along the displacement axis so that the end of the molecular conductance plateau occurs at zero displacement.

To determine, with statistical significance, the single-molecule junction rupture force, we collect thousands of simultaneous conductance and force traces and analyze this data by using a two-dimensional histogram technique, detailed in Chapter 2[26]. Briefly, the conductance traces are analyzed to select those that have a conductance plateau within the conductance range determined from the histogram shown in Figure 3.2, and by requiring a conductance drop of a factor of 5 immediately following the plateau. Although the molecular conductance features are easily recognizable, the short length of **B1** molecule results in a relatively infrequent ($\sim 8\%$) formation of single-molecule junctions. These selected conductance traces and the simultaneously measured force traces are then overlaid after aligning each to a common point along the displacement axis (as shown in insets of Figure 3.3a,b). All force traces are also aligned along the force axis by adding a constant offset to the entire trace such that the force at the end of the conductance plateau is zero. Figure 3.3a,b show the 2D conductance and force histograms, respectively, presenting the statistical representation of all the selected traces. A statistically averaged rupture force is then determined from the profile of the two-dimensional force histogram (black overlaid trace in Figure 3.3b). The magnitude of the sharp drop in this profile at zero-displacement corresponds to the average bond rupture force. For measurements with clean gold, we have shown that the rupture force of a gold single-atomic junction is 1.4 ±

0.2 nN. Applying the same methodology to Au-**B1**-Au junctions, we obtain a rupture force of 0.6 ± 0.1 nN. This force is comparable to that required to rupture the Au-NH$_2$ and Au-SMe bond[26, 27], indicating that the COO$^-$-Au binding strength is not very different from that of the SMe-Au donor-acceptor bond.
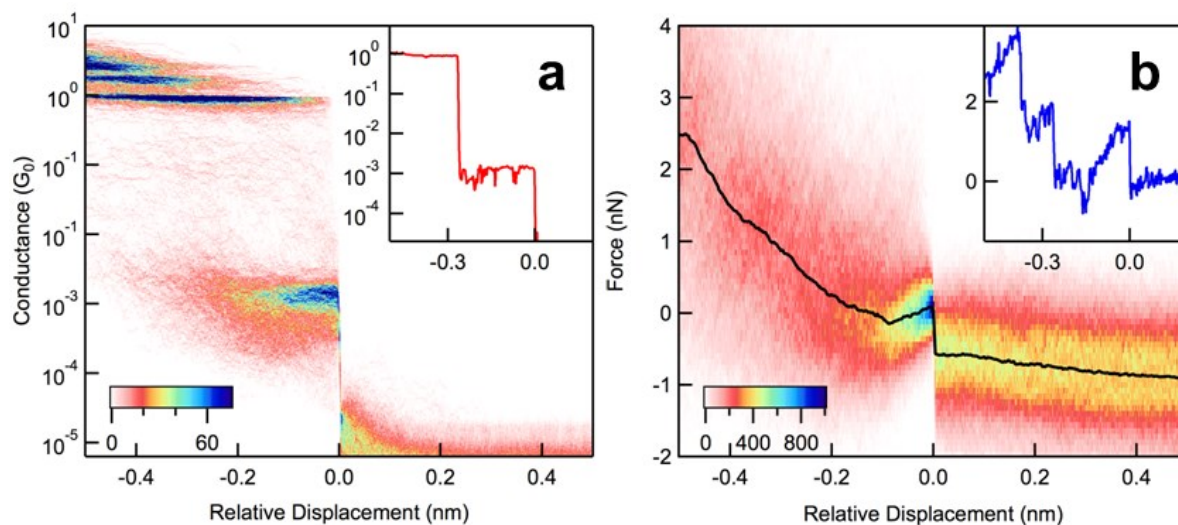
Figure 3.3. Force measurements with molecule B1. (a) 2D conductance-displacement histogram of **B1** measured in the conducting AFM setup. Inset: Sample conductance trace, offset such that the drop from the molecular conductance plateau occurs at zero displacement. (b) 2D force-displacement histogram constructed from simultaneously measured force across **B1** junctions. The statistically averaged force profile (black line) is overlaid. Inset: Sample force trace, measured simultaneously with the conductance trace shown in inset of Figure 3.3a.

In conclusion, we have experimentally probed the electronic transport through saturated and conjugated molecules with carboxyl linkages. We have shown that the carboxylic acid linker forms mechanically stable single-molecule junction, with a rupture force similar to other well-characterized linkers.[26-28] Just as in the case of thiol linkers (SH), the hydrogen in the COOH linkers plays a critical role in its binding mechanism to Au electrodes. Taken together, these measurements establish the possibility of using COOH as a mechanically stable and electronically conducting linker group, and open up interesting avenues to a broad range of chemical modifications to tune interfacial electron transfer.

3.4 References

1.   C. Joachim and M.A. Ratner, *Molecular electronics: some views on transport junctions and beyond.* Proceedings of the National Academy of Sciences of the United States of America, 2005. **102**(25): p. 8801-8.

2.   A. Nitzan and M.A. Ratner, *Electron Transport in Molecular Wire Junctions.* Science, 2003. **300**(5624): p. 1384-1389.

3.   W.K. Paik, S.B. Han, W. Shin, and Y.S. Kim, *Adsorption of carboxylic acids on gold by anodic reaction.* Langmuir, 2003. **19**(10): p. 4211-4216.

4.   M.A. Reed, C. Zhou, C.J. Muller, T.P. Burgin, and J.M. Tour, *Conductance of a molecular junction.* Science, 1997. **278**(5336): p. 252-254.

5.   B. Xu and N.J. Tao, *Measurement of Single-Molecule Resistance by Repeated Formation of Molecular Junctions.* Science, 2003. **301**(5637): p. 1221-1223.

6.   Y.S. Park, A.C. Whalley, M. Kamenetska, M.L. Steigerwald, M.S. Hybertsen, C. Nuckolls, and L. Venkataraman, *Contact chemistry and single-molecule conductance: A comparison of phosphines, methyl sulfides, and amines.* Journal of the American Chemical Society, 2007. **129**(51): p. 15768-15769.

7.   M. Kiguchi, O. Tal, S. Wohlthat, F. Pauly, M. Krieger, D. Djukic, J.C. Cuevas, and J.M. van Ruitenbeek, *Highly conductive molecular junctions based on direct binding of benzene to platinum electrodes.* Physical Review Letters, 2008. **101**(4).

8.   V.B. Engelkes, J.M. Beebe, and C.D. Frisbie, *Length-dependent transport in molecular junctions based on SAMs of alkanethiols and alkanedithiols: Effect of metal work function and applied bias on tunneling efficiency and contact resistance.* Journal of the American Chemical Society, 2004. **126**(43): p. 14287-14296.

9.   M.S. Hybertsen, L. Venkataraman, J.E. Klare, A.C. Whalley, M.L. Steigerwald, and C. Nuckolls, *Amine-linked single-molecule circuits: systematic trends across molecular families.* Journal of Physics-Condensed Matter, 2008. **20**(37).

10.   E. Lörtscher, J.W. Ciszek, J. Tour, and H. Riel, *Reversible and controllable switching of a single-molecule junction.* Small, 2006. **2**(8-9): p. 973-977.

11.   C. Li, I. Pobelov, T. Wandlowski, A. Bagrets, A. Arnold, and F. Evers, *Charge transport in single Au / alkanedithiol / Au junctions: coordination geometries and conformational degrees of freedom.* J Am Chem Soc, 2008. **130**(1): p. 318-26.

12. L. Venkataraman, J.E. Klare, I.W. Tam, C. Nuckolls, M.S. Hybertsen, and M.L. Steigerwald, *Single-molecule circuits with well-defined molecular conductance.* Nano Letters, 2006. **6**(3): p. 458-462.

13. F. Chen, X.L. Li, J. Hihath, Z.F. Huang, and N.J. Tao, *Effect of anchoring groups on single-molecule conductance: Comparative study of thiol-, amine-, and carboxylic-acid-terminated molecules.* Journal of the American Chemical Society, 2006. **128**(49): p. 15874-15881.

14. M. Kiguchi, S. Miura, T. Takahashi, K. Hara, M. Sawamura, and K. Murakoshi, *Conductance of single 1,4-benzenediamine molecule bridging between Au and Pt electrodes.* Journal of Physical Chemistry C, 2008. **112**(35): p. 13349-13352.

15. J.S. Meisner, M. Kamenetska, M. Krikorian, M.L. Steigerwald, L. Venkataraman, and C. Nuckolls, *A Single-Molecule Potentiometer.* Nano Letters, 2011. **11**(4): p. 1575-1579.

16. C.A. Martin, D. Ding, J.K. Sørensen, T. Bjørnholm, J.M. van Ruitenbeek, and H.S.J. van der Zant, *Fullerene-based anchoring groups for molecular electronics.* Journal of the American Chemical Society, 2008. **130**(40): p. 13198-13199.

17. S.T. Schneebeli, M. Kamenetska, Z.L. Cheng, R. Skouta, R.A. Friesner, L. Venkataraman, and R. Breslow, *Single-Molecule Conductance through Multiple pi-pi-Stacked Benzene Rings Determined with Direct Electrode-to-Benzene Ring Connections.* Journal of the American Chemical Society, 2011. **133**(7): p. 2136-2139.

18. R. Parameswaran, J.R. Widawsky, H. Vázquez, Y.S. Park, B.M. Boardman, C. Nuckolls, M.L. Steigerwald, M.S. Hybertsen, and L. Venkataraman, *Reliable Formation of Single Molecule Junctions with Air-Stable Diphenylphosphine Linkers.* Journal of Physical Chemistry Letters, 2010. **1**(14): p. 2114-2119.

19. A. Mishchenko, L.A. Zotti, D. Vonlanthen, M. Burkle, F. Pauly, J.C. Cuevas, M. Mayor, and T. Wandlowski, *Single-Molecule Junctions Based on Nitrile-Terminated Biphenyls: A Promising New Anchoring Group.* Journal of the American Chemical Society, 2011. **133**(2): p. 184-187.

20. Z.L. Cheng, R. Skouta, H. Vázquez, J.R. Widawsky, S. Schneebeli, W. Chen, M.S. Hybertsen, R. Breslow, and L. Venkataraman, *In situ formation of highly conducting covalent Au-C contacts for single-molecule junctions.* Nature Nanotechnology, 2011. **6**(6): p. 353-357.

21. W. Chen, J.R. Widawsky, H. Vázquez, S.T. Schneebeli, M.S. Hybertsen, R. Breslow, and L. Venkataraman, *Highly Conducting π-Conjugated Molecular Junctions Covalently Bonded to Gold Electrodes.* Journal of the American Chemical Society, 2011. **133**(43): p. 17160-17163.

22. J. Ulrich, D. Esrail, W. Pontius, L. Venkataraman, D. Millar, and L.H. Doerrer, *Variability of conductance in molecular junctions.* Journal of Physical Chemistry B, 2006. **110**(6): p. 2462-2466.

23. X.L. Li, J. He, J. Hihath, B.Q. Xu, S.M. Lindsay, and N.J. Tao, *Conductance of single alkanedithiols: Conduction mechanism and effect of molecule-electrode contacts.* Journal of the American Chemical Society, 2006. **128**(6): p. 2135-2141.

24. H.J. Himmel, K. Weiss, B. Jager, O. Dannenberger, M. Grunze, and C. Woll, *Ultrahigh vacuum study on the reactivity of organic surfaces terminated by OH and COOH groups prepared by self-assembly of functionalized alkanethiols on Au substrates.* Langmuir, 1997. **13**(19): p. 4943-4947.

25. A. Cossaro, M. Puppin, D. Cvetko, G. Kladnik, A. Verdini, M. Coreno, M. de Simone, L. Floreano, and A. Morgante, *Tailoring SAM-on-SAM Formation.* Journal of Physical Chemistry Letters, 2011. **2**(24): p. 3124-3129.

26. M. Frei, S.V. Aradhya, M. Koentopp, M.S. Hybertsen, and L. Venkataraman, *Mechanics and chemistry: single molecule bond rupture forces correlate with molecular backbone structure.* Nano Letters, 2011. **11**(4): p. 1518-1523.

27. M. Frei, S.V. Aradhya, M.S. Hybertsen, and L. Venkataraman, *Linker dependent bond rupture force measurements in single-molecule junctions.* Journal of the American Chemical Society, 2012. **134**(9): p. 4003-6.

28. S.V. Aradhya, J.S. Meisner, M. Krikorian, S. Ahn, R. Parameswaran, M.L. Steigerwald, C. Nuckolls, and L. Venkataraman, *Dissecting contact mechanics from quantum interference in single-molecule junctions of stilbene derivatives.* Nano Letters, 2012. **12**(3): p. 1643-7.

29. L. Engman and J.S.E. Hellberg, *A General Procedure for the Synthesis of Methylthio-Substituted, Methylseleno-Substituted and Methyltelluro-Substituted Aromatic-Compounds.* Journal of Organometallic Chemistry, 1985. **296**(3): p. 357-366.

30. Y.S. Park, J.R. Widawsky, M. Kamenetska, M.L. Steigerwald, M.S. Hybertsen, C. Nuckolls, and L. Venkataraman, *Frustrated Rotations in Single-Molecule Junctions.* Journal of the American Chemical Society, 2009. **131**(31): p. 10820-10821.

31. A. Ikeda, K. Terada, M. Shiotsuki, and F. Sanda, *Synthesis of Polymers Bearing Proline Moieties in the Side Chains and Their Application as Catalysts for Asymmetric Induction.* Journal of Polymer Science Part a-Polymer Chemistry, 2011. **49**(17): p. 3783-3796.

32. H. Ohnishi, Y. Kondo, and K. Takayanagi, *Quantized conductance through individual rows of suspended gold atoms.* Nature, 1998. **395**(6704): p. 780-783.

33. A.I. Yanson, G.R. Bollinger, H.E. van den Brom, N. Agrait, and J.M. van Ruitenbeek, *Formation and manipulation of a metallic wire of single gold atoms.* Nature, 1998. **395**(6704): p. 783-785.

34. M. Kamenetska, M. Koentopp, A. Whalley, Y. Park, M. Steigerwald, C. Nuckolls, M. Hybertsen, and L. Venkataraman, *Formation and Evolution of Single-Molecule Junctions.* Physical Review Letters, 2009. **102**(12): p. 126803.

35. S.Y. Quek, M. Kamenetska, M.L. Steigerwald, H.J. Choi, S.G. Louie, M.S. Hybertsen, J.B. Neaton, and L. Venkataraman, *Mechanically controlled binary conductance switching of a single-molecule junction.* Nature Nanotechnology, 2009. **4**(4): p. 230-234.

36. K. Moth-Poulsen and T. Bjornholm, *Molecular electronics with single molecules in solid-state devices.* Nature Nanotechnology, 2009. **4**(9): p. 551-556.

37. A. Salomon, D. Cahen, S. Lindsay, J. Tomfohr, V.B. Engelkes, and C.D. Frisbie, *Comparison of electronic transport measurements on organic molecules.* Advanced Materials, 2003. **15**(22): p. 1881-1890.

38. H.B. Akkerman and B. de Boer, *Electrical conduction through single molecules and self-assembled monolayers.* Journal of Physics: Condensed Matter, 2008. **20**(1): p. 013001.

39. D.J. Wold, R. Haag, M.A. Rampi, and C.D. Frisbie, *Distance dependence of electron tunneling through self-assembled monolayers measured by conducting probe atomic force microscopy: Unsaturated versus saturated molecular junctions.* Journal of Physical Chemistry B, 2002. **106**(11): p. 2813-2816.

40. J. Halpern and L.E. Orgel, *The Theory of Electron Transfer between Metal Ions in Bridged Systems.* Discussions of the Faraday Society, 1960. **29**: p. 32-41.

41. L.A. Nagahara, T. Thundat, and S.M. Lindsay, *Preparation and Characterization of Stm Tips for Electrochemical Studies.* Review of Scientific Instruments, 1989. **60**(10): p. 3128-3130.

42. P.E. Marszalek, W.J. Greenleaf, H.B. Li, A.F. Oberhauser, and J.M. Fernandez, *Atomic force microscopy captures quantized plastic deformation in gold nanowires.* Proceedings of the National Academy of Sciences of the United States of America, 2000. **97**(12): p. 6282-6286.

4

Dissecting contact mechanics from conductance pathways in single-molecule junctions of stilbene derivatives

Electronic factors in molecules such as quantum interference and cross-conjugation can lead to dramatic modulation and suppression of conductance in single-molecule junctions. Probing such effects at the single-molecule level requires simultaneous measurements of independent junction properties, as conductance alone cannot provide conclusive evidence of junction formation for molecules with low conductivity. Here, we study the mechanics of a set of stilbene derived single-molecule junctions by measuring the force across the junctions even when no clear low-bias conductance is measured. Comparing the results from these molecules, our experiments provide the first direct systematic study of the interplay between contact mechanics and the distinctively quantum mechanical nature of electronic transport in single-molecule junctions.

This work was performed in collaboration with Dr. Jeffrey Meisner and other members of Prof. Nuckolls' group; DFT calculations were performed by Dr. Michael Steigerwald.

Understanding and controlling the electronic properties of molecular wires is fundamentally important for molecular electronics[1, 2]. The scanning tunneling microscope (STM) based break junction approach gives a deep insight into the structure-conductance relationship in single-molecule junctions because it provides a statistical interpretation over an ensemble of measurements[3-5]. However, in these studies only one physical property - the junction conductance - is measured. This limits the interpretation of the results in junctions where the conductance is either very small or ill-defined. Theory predicts that there will be large modulations in single molecule conductance for systems exhibiting quantum interference, such as variously substituted aromatic molecules and cross-conjugated molecular wires[6-12]. For example, theoretical calculations have predicted that a benzene ring bound to metal electrodes with linker groups at the 1 and 3 positions (*meta* to each other) should have a conductance that is five orders of magnitude lower than that of a 1,4-linked benzene[6]. To determine, from low-bias conductance measurements alone, whether such effects are present is difficult because the conductance of the *meta*-substituted molecules is often below the experimental noise limit of the instruments. At high biases, non-equilibrium effects, junction heating and inelastic processes cannot be ruled out[13-15]. Furthermore, a statistical approach is needed to demonstrate the robustness of interference phenomenon by rigorously accounting for experimental details such as junction formation probability, binding strength, junction-to-junction variation and junction structure.

Here we overcome these critical challenges by simultaneously measuring force and conductance across single molecule junctions using a conducting atomic force microscope setup[16, 17]. We study three molecular backbones: 4,4'-di(methylthio)stilbene (**1**), 1,2-(bis(4-methylthio)phenyl)ethane (**2**) and 3,3'-di(methylthio)stilbene (**3**). These molecules are chosen

since the longer stilbene backbones, rather than benzene backbones discussed above, form molecular junctions more frequently and the thiomethyl (SMe) terminal groups provide reliable mechanical and electrical contact to the Au electrodes[18, 19]. We exploit the high binding probabilities and reliable contact properties to acquire and analyze large datasets comprised of thousands of individual junctions to probe the robustness of interference effects, in each case. The *para*-positioned linker groups in **1** effectively couple across the π-system and provide a conducting single-molecule junction. In **2** the mechanical linkages between the metal and the molecule are the same as in **1**, but conjugation is broken due to the saturated bridge, which results in lower junction conductance. In **3**, the mechanical linkers are moved to the *meta*-position but the conjugated bridge is retained, as in **1**. There is no measurable single molecule conductance feature in **3**. We use the simultaneously measured force data to independently obtain signatures of junction formation and rupture. We quantitatively determine the elongation length and rupture force for each of the three molecules, irrespective of their conductance. In contrast to the conductance, we find that the rupture force is insensitive to the linker group placement. We are able to demonstrate, for the first time, that the *meta* substituted **3** forms mechanically stable Au-molecule-Au junctions but does not show a measurable conductance, and theoretical calculations point to quantum mechanical interference as the origin of this behavior. These measurements enable us not only to investigate junctions of non-conducting molecules, but more generally allow us to deconvolute electronic effects from mechanical evolution in single-molecule junctions.

4.1 Experimental setup and measurements of force and conductance

Simultaneous measurements of single-molecule conductance and force are carried out using a custom-built conductive atomic force microscope (AFM) which has been described in

detail previously[17] (see also Chapter 2). Molecular junctions are formed between an Au-coated

AFM cantilever and an Au-on-mica substrate schematically represented in Figure 2.9a.
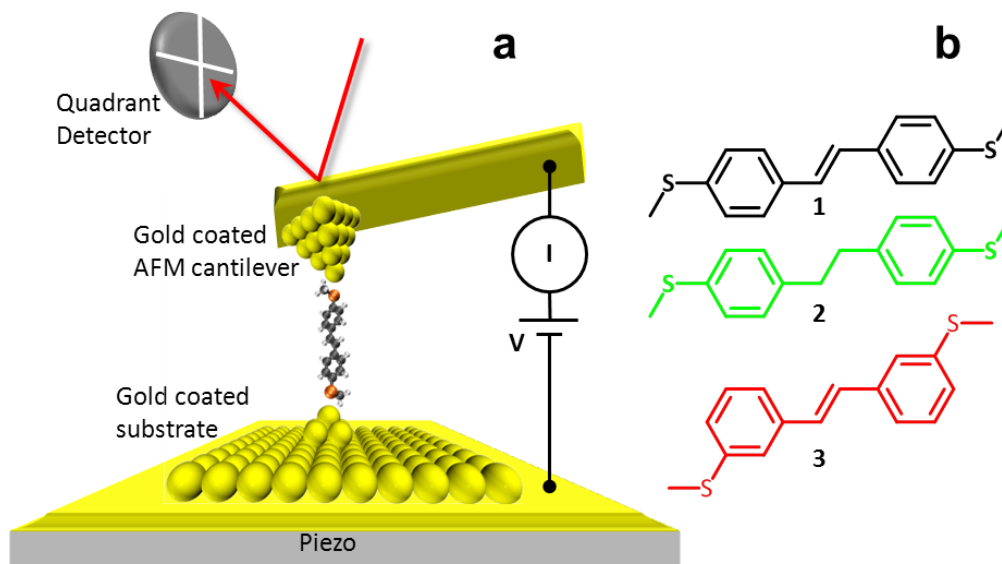
Figure 4.1. Experimental setup and molecular structures. (a) Schematic of AFM apparatus and (b) chemical structures of molecules **1-3**.

Conductance is determined by measuring current through the junction at an applied bias of 75

mV. Simultaneous measurements of cantilever deflection relate to the force applied across the

junction. The AFM is operated in ambient conditions at room temperature. Dilute solutions (0.1

mM) of the target molecules (**1-3**, Figure 2.9b) in 1,2,4-trichlorobenzene are deposited on the

substrate. For each measurement, the tip is brought into contact with the substrate until a

conductance greater than 5 G_0 ($G_0 = 2e^2/h$, the quantum of conductance) is achieved, and then

retracted at a constant velocity of 18 nm/s while both conductance and cantilever deflection are

continuously recorded. During this elongation, the Au contact thins down to a single atom point

contact, clearly identified by a conductance plateau of 1 G_0. In the absence of molecules the Au

contact ruptures to a broken junction when elongated further. However, in a solution of

molecules, molecular junctions are frequently formed after the rupture of the 1 G_0 plateau.

Figure 4.2 displays simultaneously measured force and conductance traces obtained while breaking Au point contacts without molecules (Figure 4.2a) or with **1** and **3** (Figure 4.2b,c respectively). We see a stepwise decrease in conductance (red) while the simultaneously
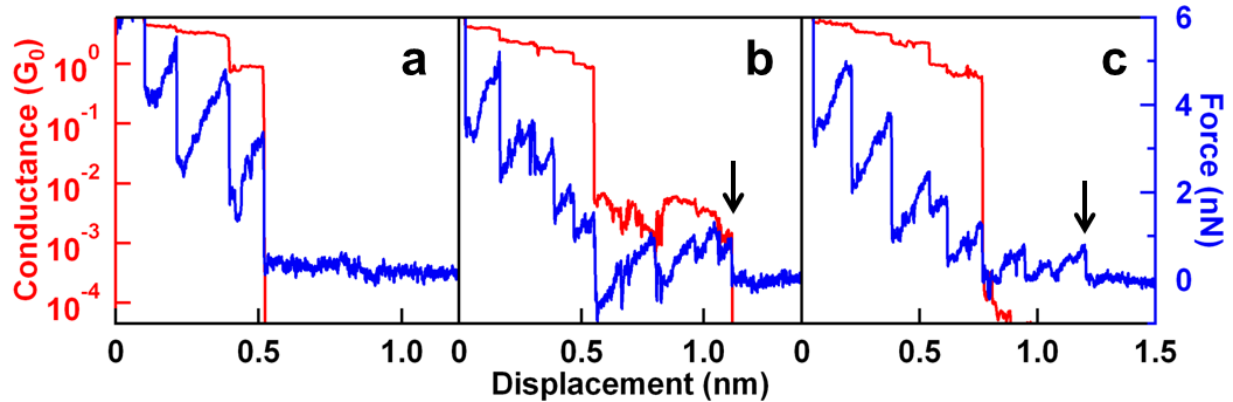
Figure 4.2. Sample experimentally measured traces. Sample traces of simultaneously measured conductance (red, left axis) and force (blue, right axis) for (a) Au-Au junctions (b) Au-**1**-Au and (c) Au-**3**-Au single molecule junctions. Downward arrows indicate the final force event identifying junction rupture.

measured force (blue) has a characteristic saw-tooth pattern with alternating linear ramps (elastic loading) and abrupt drops (structural rearrangement or bond rupture) in force[17, 20]. After the rupture of the Au single-atom contact in the absence of molecules (identified by its characteristic 1 G_0 conductance plateau), no further features are seen in either conductance or force. The conductance drops below the measurable level (~10^{-5} G_0), and the force stays constant because there is no more a load on the cantilever, as seen in Figure 4.2a. When an Au point contact is broken in the presence of **1** or **2**, a single-molecule junction with a characteristic conductance feature is formed ~90 % of the time[18, 19]. This additional plateau is seen in the conductance traces immediately following the rupture of the Au contact, as illustrated in Figure 4.2b (red trace) for an individual measurement with **1**. The simultaneously acquired force traces (blue) also show additional saw-tooth features. In this trace, we see that the 1 G_0 ruptures at ~0.5 nm along the displacement axis and the molecular junction ruptures after an additional elongation of about

0.6 nm. Once this molecular junction has ruptured, no more conductance or force features are seen in measurements with **1** or **2**. In contrast, measurements with **3** do not exhibit any well-defined conductance plateau, however a majority of the measured traces show multiple force features after the rupture of the Au-contact as illustrated in Figure 4.2c. Such force features are similar in magnitude to those seen in measurements of **1** and **2**.

4.2   Statistical analyses without relying on molecular conductance features

For each molecule (**1-3**) we analyze 7000 simultaneously measured conductance and force traces using an automated algorithm detailed in the Chapter 2, section 2.7. We use these large datasets to obtain statistically significant information because the atomic-scale structure varies from junction to junction. We begin by locating the displacement when the Au point contact ruptures in the conductance traces. This is the point in the trace when conductance drops below 1 G_0. Focusing on the simultaneously acquired force trace, we analyze a 1 nm-long segment of this trace (~ S-S distance for the three molecules) beyond the 1 G_0 rupture point to locate the final junction rupture event, i.e., the last abrupt force drop. The distance between the 1 G_0 rupture location and this final force event defines the molecular junction elongation length. For conducting molecules (Figure 4.2b), we observe that molecular junctions form immediately after the rupture of the Au point contacts and therefore junction elongation length is equivalent to the conductance plateau length which has been used in previous studies to characterize single-molecule junction mechanics[16, 18, 21]. It is important to note that we are able to identify molecular junction rupture events through force data and do not require a well-defined conductance plateau to obtain the elongation length.

Two-dimensional conductance and force histograms are now generated using the location of the final force event as the origin along the displacement axis[18]. For conductance, individual traces are offset laterally such that this same rupture location is the origin of the displacement axis. The 2D conductance histograms have linear bins along the displacement axis (x-axis, 500 bins/nm) and logarithmic bins along the conductance axis (y-axis, 200 bins/decade) [22]. For force data, individual traces are offset both laterally as above and vertically such that the force value at the origin is zero. The 2D force histograms have linear bins along displacement (x, 500 bins/nm) and force (y, 12.5 bins/nN) axes. Every vertical section of this 2D force histogram is fit with a Gaussian and its peak is used to determine a statistically averaged force profile for the entire dataset[17]. Since there is no selection based on conductance, every trace with a significant force event after Au rupture (> 85% of measured traces in each case) is analyzed.

In Figure 4.2b, we display an individual force and conductance measurement with **1**. We see a clear conductance plateau after the rupture of Au point contacts. The simultaneously acquired force traces shows several saw-tooth features indicating multiple structural changes in the junction, ultimately rupturing after ~0.6 nm of elongation[23]. The final force event (downward arrow in Figure 4.2b) occurs at exactly the same displacement as the conductance drop. Figure 4.3a shows the 2D conductance histogram for **1** representing 6788 of the 7000 individual traces for which a significant force event was found after 1 G_0 rupture. Although only force data was used to identify and set the zero displacement at the molecular junction rupture point, we observe that the conductance also drops sharply to the instrument noise level at zero-displacement, demonstrating the reliability of this force-based alignment procedure. A conductance profile of this histogram shows a clear peak at 1.3×10^{-3} G_0 (Figure 4.3d, black trace), which compares well with the 1D conductance histograms created from all the measured
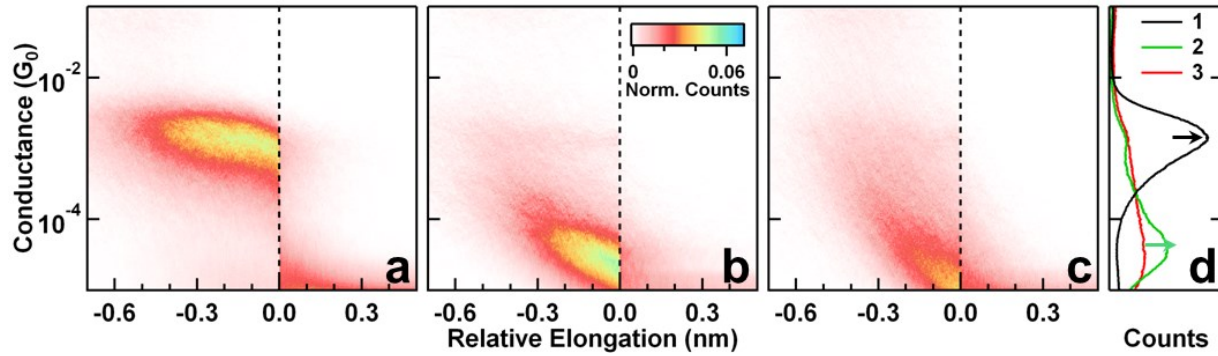
Figure 4.3. Statistical analysis of conductance. Displacement-preserving 2D conductance histograms (a, b, c) for **1**, **2** and **3**, respectively and profiles of conductance before rupture (d). The histograms represent more than 85% of the 7000 measured traces which show a significant force event beyond Au rupture, in each case. The abrupt jump in conductance at the displacement origin (dashed vertical lines provided as a visual guide) for **1** and **2** shows that bond rupture coincides with conductance drops. Arrows indicate the most frequently measured conductance value from the conductance profiles of **1** and **2**.

traces (see Section 4.4). We see that the *para*-linked molecule **1** forms junctions with relatively high, well-defined conductance, as observed for other fully-conjugated molecular wires. The 2D force histogram created from the simultaneously acquired force traces is shown in Figure 4.4, along with the statistically averaged force profile. This force profile shows an abrupt drop of 0.5 nN at zero displacement, corresponding to the force required to rupture this junction[17].
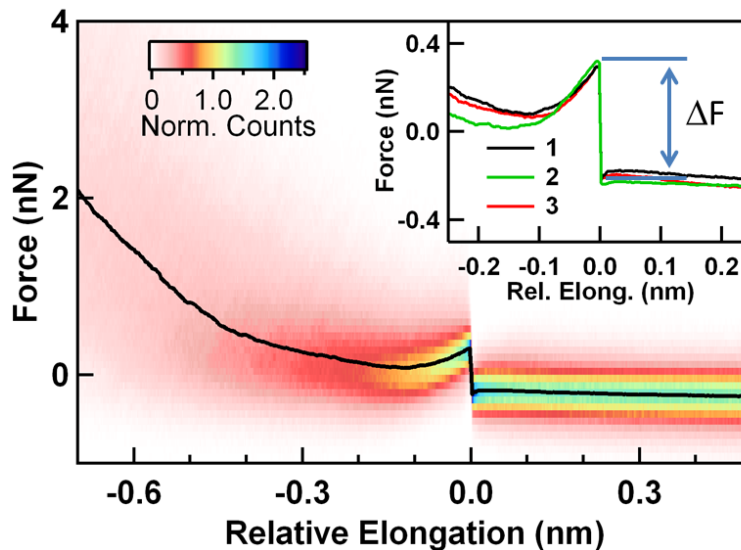
Figure 4.4. Statistical analysis of force. 2D force histogram for molecule **1** with the averaged force profile overlaid. Inset: Statistically averaged force profiles for molecular junctions of **1**, **2**, and **3** in black, green and red, respectively.

Molecule **2** shows similar behavior in conductance and force. The 2D conductance histogram (Figure 4.3b, from 6332 traces), shows a clear conductance feature at a significantly lower value of 3.2×10^{-5} G_0. This result is intuitively understood as arising from the lowered communication between the aromatic rings due to the ethane bridge at the center, even though the *para*-positions of the linkers is identical to **1**. From the statistically averaged force profile (Inset, Figure 4.4, green trace), we find that these junctions also rupture at a force of 0.5 nN and show a loading and rupture behavior similar to **1**.

Qualitatively different behavior is found in junctions of **3**. We do not see clear conductance plateaus in individual traces, as shown in Figure 4.2c. Individual force traces, however, do show saw-tooth signatures typical of junction structure evolution and bond rupture, and are analogous to force measurements of **1** and **2**. This is representative of the loading and rupture event of the molecular junction in individual traces. The 2D conductance histogram (Figure 4.3c), constructed from all traces that show a clear bond rupture event in the force data, shows a broad conductance feature slightly above the noise level as seen in the profile in Figure 4.3d (red trace). This can be ascribed to the small, but non-zero contribution to conductance from the sigma channel, through-space tunneling between the electrodes and possibly dispersive interactions between the molecular π-orbitals and the Au electrodes[9, 24]. The averaged force profile centered at the rupture event generated from 5965 traces is shown in the inset of Figure 4.4 (red trace). Clearly, there are a statistically significant number of traces that have rupture events after the G_0 plateau, a fraction similar to **1** and **2**, which could not be identified by conductance data alone. The bond rupture force for these junctions is also 0.5 nN. Therefore, we conclude that single-molecule junctions of **3** are formed, but do not show clear conductance plateaus and have a significantly lower conductance, confirming the theoretical predictions of a

low conductance due to interference effects. It is important to note that the character of the conductance we observe for **3** is qualitatively very different from that seen in **1** or **2**, as is further evidenced in the conventional linear and logarithmically binned conductance histograms (Section 4.4).

Taken together, the force profiles for **1**, **2** and **3** illustrate that bond rupture forces are approximately the same for all three molecular junctions, independent of the linker position. The rupture force depends on the specific interaction of the Au-SMe donor-acceptor bond in each molecule, and the apparent insensitivity of the rupture force to the linker position, within our experimental force resolution, can be explained by the similar local structure near the Au-SMe bonds for **1-3**.

The independent analysis of force and conductance allows us to study the mechanical aspects of junction evolution even in the absence of conductance plateaus. In particular, the amount of elongation sustained by the junction before rupture – the junction elongation length - gives information about the geometry of the Au-molecule-Au junction. In general, the molecule in the junction can sample multiple binding sites during elongation before achieving the idealized vertical Au-molecule-Au junction geometry[18]. The junction elongation length scales with the molecular S-S distance, but is smaller than the molecule length, because of a non-zero gap that is opened when the Au point contact is broken[22]. Histograms of elongation lengths are constructed from individual traces and have a Gaussian distribution (Section 4.4). The peak values obtained from these distributions for **1-3** are presented in Table 4.1. The plateau lengths of **1** and **3** are in accordance with their respective S-S distances. However, a relatively smaller plateau length is observed for **2**. This could be due to non-planar configurations accessible to the ethane bridge in **2**, which are not allowed in either **1** or **3** due to the central C=C double bond.

These measured elongation lengths give us further confirmation of the junction formation, independent of conductance[3, 25].

Table 4.1. Conductance, elongation length and rupture force for single molecule junctions with molecules **1-3**.

Molecule	Experimental Measurements			DFT
	Conductance (G_0)	Elongation Length (nm)	Rupture Force (nN)	S-S distance [a] (nm)
1	1.3×10^{-3}	0.42	0.5	1.31
2	3.2×10^{-5}	0.32	0.5	1.29
3 [b]	-	0.31	0.5	1.17

a - B3LYP/6-31G** level of theory

b - non-conductive molecule **3** did not show well-defined peak in conductance profiles.

4.3 DFT calculations and discussion of results

Having established the similar mechanical stability for **1-3**, we are able to make direct comparisons between the chemical structures and the corresponding conductances. We can unambiguously conclude that **2** is less conducting than **1** due to broken conjugation, while **3** forms mechanically stable yet electrically insulating junctions. **1** and **3** are essentially planar structures with all sp^2-carbon atoms and with similar molecular lengths; however, the *meta*-positioned linker groups effectively turn off the conductance.

To better understand these results, we have examined the electronic structures of the organic molecules bonded to an Au dimer (which represents one of the Au electrodes) through an Au-S donor-acceptor bond. We use a dimer of Au atoms to avoid complications attendant to the unpaired spin occupying the valence 6s orbital of a single Au atom. We attach the candidate organic molecule to just one "electrode" in order to appreciate what the second electrode sees as

it encounters the metal-bound organic. In effect this is a simplified model for the chemical state of the system prior to the charge transfer. We performed DFT calculations of the electronic structures of these model systems at the B3LYP/6-31G** level[26]. The highest occupied molecular orbital (HOMO) from the geometry-optimized structures, Au_2-**1**, Au_2-**2** and Au_2-**3**, are shown in Figure 4.5. The HOMO of **1** extends across the entire π-space of the molecule in
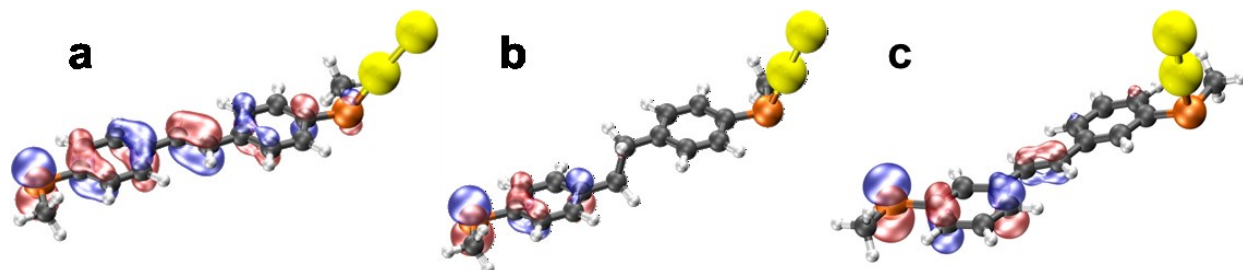
Figure 4.5. Theoretical calculations. DFT optimized structures and isosurface plots of the HOMO of (a) Au_2-**1**, (b) Au_2-**2** and (c) Au_2-**3**.

contrast to that of **2** and **3**. Significantly, in **1**, the HOMO connects both the terminal sulfur atoms and provides a clear electronic conduit between the sulfur groups. In contrast, in **2**, one side of the molecule doesn't communicate with the other which is a direct result of the saturated ethane bridge. In addition, rotation around these sp^3-carbons increases the conformational freedom in the molecular junction. Therefore, a broad peak is expected in the conductance histograms without retarding the rupture force. In **3**, we observe that although the HOMO extends across the bridge, it does not have significant amplitude on the sulfur atom at the *meta* position. This finding is consistent with observations from various related approaches, such as organic reaction kinetics[27, 28], Hammett coefficients[29], and even classic organic arrow-pushing conventions, which predict a node at the *meta*-position[30]. For direct experimental evidence, Daub and coworkers electrochemically quantified the charge-transport kinetics between *meta*- and *para*-

(styryl)stilbenes[31]. However, this area has recently received more theoretical attention due to the possibility of studying these effects at the single-molecule level[6-12].

In summary, single-molecule junctions of stilbene derivates with *para* and *meta*-linked stilbenes have been formed using a conducting-AFM approach that allows for measurements of single-molecule mechanics through force, independent of conductance. We have found that despite great differences in their conductance values, each molecule assembles into single-molecule junctions that are mechanically stable. Our results show that both *para*- and *meta*-linkers provide similar mechanical stability to the junctions yet radically change the conductance. For these reasons the *para*-linker groups behave as typical electro-mechano contacts, while *meta*-linkers disrupt the conduction acting primarily as mechanical contacts. By quantitatively accounting for the contact mechanics, these results represent the first direct proof that quantum interference is an inherent property arising from the molecular structure, and is not quenched by microscopic junction-to-junction variations. This two-property measurement capability extends our understanding of single-molecule junction properties to such low-conductive and insulating systems as simple molecular connectors and dielectrics materials. Moreover, this approach provides a means to design and study new molecular switches and devices that utilize quantum interference.

4.4   Supporting information

Figure 4.6 compares the conductance and step length of molecule **1-3**. In the conductance histogram (Figure 4.6a), the conductance feature for **1** is prominent in both the linearly and logarithmically binned histograms, while **3** has no discernable feature in either representations.

The peak positions of the step length distributions (Figure 4.6b) for each of the molecules 1-3 is

tabulated in Table 4.1.
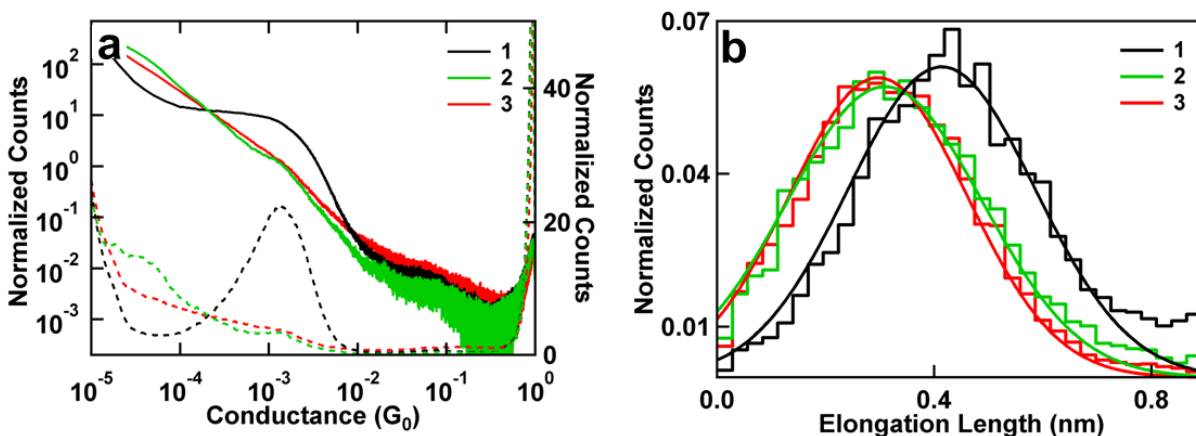
Figure 4.6. Conductance and step length histograms. (a) Histograms of conductance for all the measured traces for molecules **1**-**3**. Solid lines present a log-log plot of linearly binned conductance histograms with bin size = 10^{-5} G_0 and dashed lines present the logarithmically binned conductance histograms with 100 bins/decade. (b) Elongation length distributions for molecules **1**-**3**, normalized by total number of traces (**1**-6788, **2**-6332 and **3**-5965) for each case (0.03 nm/bin). Gaussian fits to the histograms are overlaid.

4.5   References

1.   A. Nitzan and M.A. Ratner, *Electron Transport in Molecular Wire Junctions.* Science, 2003. **300**(5624): p. 1384-1389.

2.   C. Joachim, J.K. Gimzewski, and A. Aviram, *Electronics using hybrid-molecular and mono-molecular devices.* Nature, 2000. **408**(6812): p. 541-548.

3.   B. Xu and N.J. Tao, *Measurement of Single-Molecule Resistance by Repeated Formation of Molecular Junctions.* Science, 2003. **301**(5637): p. 1221-1223.

4.   L. Venkataraman, J.E. Klare, I.W. Tam, C. Nuckolls, M.S. Hybertsen, and M.L. Steigerwald, *Single-molecule circuits with well-defined molecular conductance.* Nano Letters, 2006. **6**(3): p. 458-462.

5.   C. Li, I. Pobelov, T. Wandlowski, A. Bagrets, A. Arnold, and F. Evers, *Charge transport in single Au / alkanedithiol / Au junctions: coordination geometries and conformational degrees of freedom.* J Am Chem Soc, 2008. **130**(1): p. 318-26.

6.   G.C. Solomon, D.Q. Andrews, T. Hansen, R.H. Goldsmith, M.R. Wasielewski, R.P.V. Duyne, and M.A. Ratner, *Understanding quantum interference in coherent molecular conduction.* Journal of Chemical Physics, 2008. **129**(5): p. 054701.

7.   T. Markussen, R. Stadler, and K.S. Thygesen, *The Relation between Structure and Quantum Interference in Single Molecule Junctions.* Nano Letters, 2010. **10**(10): p. 4260-4265.

8.   Y. Tsuji, A. Staykov, and K. Yoshizawa, *Orbital Views of Molecular Conductance Perturbed by Anchor Units.* Journal of the American Chemical Society, 2011. **133**(15): p. 5955-5965.

9.   S.-H. Ke, W. Yang, and H.U. Baranger, *Quantum-Interference-Controlled Molecular Electronics.* Nano Letters, 2008. **8**(10): p. 3257-3261.

10. D.M. Cardamone, C.A. Stafford, and S. Mazumdar, *Controlling quantum transport through a single molecule.* Nano Letters, 2006. **6**(11): p. 2422-2426.

11. T. Markussen, R. Stadler, and K.S. Thygesen, *Graphical prediction of quantum interference-induced transmission nodes in functionalized organic molecules.* Physical Chemistry Chemical Physics, 2011. **13**(32): p. 14311-14317.

12. M. Ernzerhof, *Simple orbital theory for the molecular electrician.* Journal of Chemical Physics, 2011. **135**(1): p. 014104.

13. M. Mayor, H.B. Weber, J. Reichert, M. Elbing, C. von Hänisch, D. Beckmann, and M. Fischer, *Electric current through a molecular rod - Relevance of the position of the anchor groups.* Angewandte Chemie-International Edition, 2003. **42**(47): p. 5834-5838.

14. M. Taniguchi, M. Tsutsui, R. Mogi, T. Sugawara, Y. Tsuji, K. Yoshizawa, and T. Kawai, *Dependence of Single-Molecule Conductance on Molecule Junction Symmetry.* Journal of the American Chemical Society, 2011. **133**(30): p. 11426-11429.

15. D. Fracasso, H. Valkenier, J.C. Hummelen, G.C. Solomon, and R.C. Chiechi, *Evidence for Quantum Interference in SAMs of Arylethynylene Thiolates in Tunneling Junctions with Eutectic Ga-In (EGaIn) Top-Contacts.* Journal of the American Chemical Society, 2011. **133**(24): p. 9556-9563.

16. B.Q. Xu, X.Y. Xiao, and N.J. Tao, *Measurements of single-molecule electromechanical properties.* Journal of the American Chemical Society, 2003. **125**(52): p. 16164-16165.

17. M. Frei, S.V. Aradhya, M. Koentopp, M.S. Hybertsen, and L. Venkataraman, *Mechanics and chemistry: single molecule bond rupture forces correlate with molecular backbone structure.* Nano Letters, 2011. **11**(4): p. 1518-1523.

18. M. Kamenetska, M. Koentopp, A. Whalley, Y. Park, M. Steigerwald, C. Nuckolls, M. Hybertsen, and L. Venkataraman, *Formation and Evolution of Single-Molecule Junctions.* Physical Review Letters, 2009. **102**(12): p. 126803.

19. Y.S. Park, A.C. Whalley, M. Kamenetska, M.L. Steigerwald, M.S. Hybertsen, C. Nuckolls, and L. Venkataraman, *Contact chemistry and single-molecule conductance: A comparison of phosphines, methyl sulfides, and amines.* Journal of the American Chemical Society, 2007. **129**(51): p. 15768-15769.

20. G. Rubio, N. Agraït, and S. Vieira, *Atomic-Sized Metallic Contacts: Mechanical Properties and Electronic Transport.* Physical Review Letters, 1996. **76**(13): p. 2302-2305.

21. A.I. Yanson, G.R. Bollinger, H.E. van den Brom, N. Agrait, and J.M. van Ruitenbeek, *Formation and manipulation of a metallic wire of single gold atoms.* Nature, 1998. **395**(6704): p. 783-785.

22. S.Y. Quek, M. Kamenetska, M.L. Steigerwald, H.J. Choi, S.G. Louie, M.S. Hybertsen, J.B. Neaton, and L. Venkataraman, *Mechanically controlled binary conductance switching of a single-molecule junction.* Nature Nanotechnology, 2009. **4**(4): p. 230-234.

23. Y.S. Park, J.R. Widawsky, M. Kamenetska, M.L. Steigerwald, M.S. Hybertsen, C. Nuckolls, and L. Venkataraman, *Frustrated Rotations in Single-Molecule Junctions.* Journal of the American Chemical Society, 2009. **131**(31): p. 10820-10821.

24. J.S. Meisner, M. Kamenetska, M. Krikorian, M.L. Steigerwald, L. Venkataraman, and C. Nuckolls, *A Single-Molecule Potentiometer.* Nano Letters, 2011. **11**(4): p. 1575-1579.

25. F. Chen, J. Hihath, Z. Huang, X. Li, and N.J. Tao, *Measurement of single-molecule conductance.* Annual review of physical chemistry, 2007. **58**: p. 535-564.

26. *Jaguar*, 2011, Schrödinger, LLC: New York, NY.

27. B.T. King, J. Kroulik, C.R. Robertson, P. Rempala, C.L. Hilton, J.D. Korinek, and L.M. Gortari, *Controlling the Scholl reaction.* Journal of Organic Chemistry, 2007. **72**(7): p. 2279-2288.

28. T. Michinobu, C. Boudon, J.P. Gisselbrecht, P. Seiler, B. Frank, N.N.P. Moonen, M. Gross, and F. Diederich, *Donor-substituted 1,1,4,4-tetracyanobutadienes (TCBDs): New chromophores with efficient intramolecular charge-transfer interactions by atom-economic synthesis.* Chemistry-a European Journal, 2006. **12**(7): p. 1889-1905.

29. C. Hansch, A. Leo, and R.W. Taft, *A Survey of Hammett Substituent Constants and Resonance and Field Parameters.* Chem. Rev., 1991. **91**(2): p. 165-195.

30.   L. Pauling, *The nature of the chemical bond and the structure of molecules and crystals: an introduction to modern structural chemistry*. 3rd ed. 1960: Cornell University Press, Ithaca, NY.

31.   M. Mayor, M. Buschel, K.M. Fromm, J.M. Lehn, and J. Daub, *Electron transfer through bridging molecular structures*. Ann. N.Y. Acad. Sci., 2002. **960**: p. 16-28.

5

Van der Waals interactions in metal-organic interfaces at the

single-molecule level

The forces of attraction between atoms and molecules come in different varieties and strengths. One of the most ubiquitous forms of attraction in nature is called the van der Waals force, representing non-specific interactions with more subtle underpinnings than specific chemical bonding between atoms. We use our experimental approach of measuring conductance and force simultaneously in single-molecule junctions to characterize van der Waals forces at the metal-molecule interface at the level of individual molecules, which has so far been challenging to perform quantitatively with either theoretical or experimental approaches.

The work described in this chapter was conducted in collaboration with Dr. Mark Hybertsen who performed all the theoretical calculations.

Van der Waals interaction, and its subtle interplay with chemically specific interactions and surface roughness at metal-organic interfaces, is critical to the understanding of structure-function relations in diverse areas including catalysis, molecular electronics and self-assembly [1-3]. However, van der Waals interactions remain challenging to characterize directly at the fundamental, single-molecule level both in experiments and in first principles calculations with accurate treatment of the non-local, London dispersion interactions. In particular, for metal-organic interfaces, efforts to date have largely focused on model systems consisting of adsorbed molecules on flat metallic surfaces with minimal specific chemical interaction [4-9]. Here we show, through measurements of single-molecule mechanics, that pyridine derivatives [10, 11] can bind to nano-structured Au electrodes through an additional binding mechanism beyond the chemically specific N-Au donor-acceptor bond. Using density functional theory simulations we show that van der Waals interactions between the pyridine ring and Au electrodes can play a key role in the junction mechanics. These measurements thus provide the first quantitative characterization of van der Waals interactions across metal-organic interfaces at the single-molecule level.

5.1 Experimental setup

In this work we probe bond rupture forces and junction stiffness in single molecule junctions using a home-built conducting atomic force microscope (AFM). Single-molecule junctions are formed with 4,4'-bipyridine (BP) or 1,2-bis(4-pyridyl)ethylene (BPE) molecules bound between a Au substrate and a Au coated cantilever (Figure 5.1a). Measurements of current through the junction at under an applied bias determine the junction conductance while simultaneous measurements of cantilever deflection relate to the force applied across the junction (see methods). Figure 5.1b shows the simultaneously measured conductance (upper panel) and
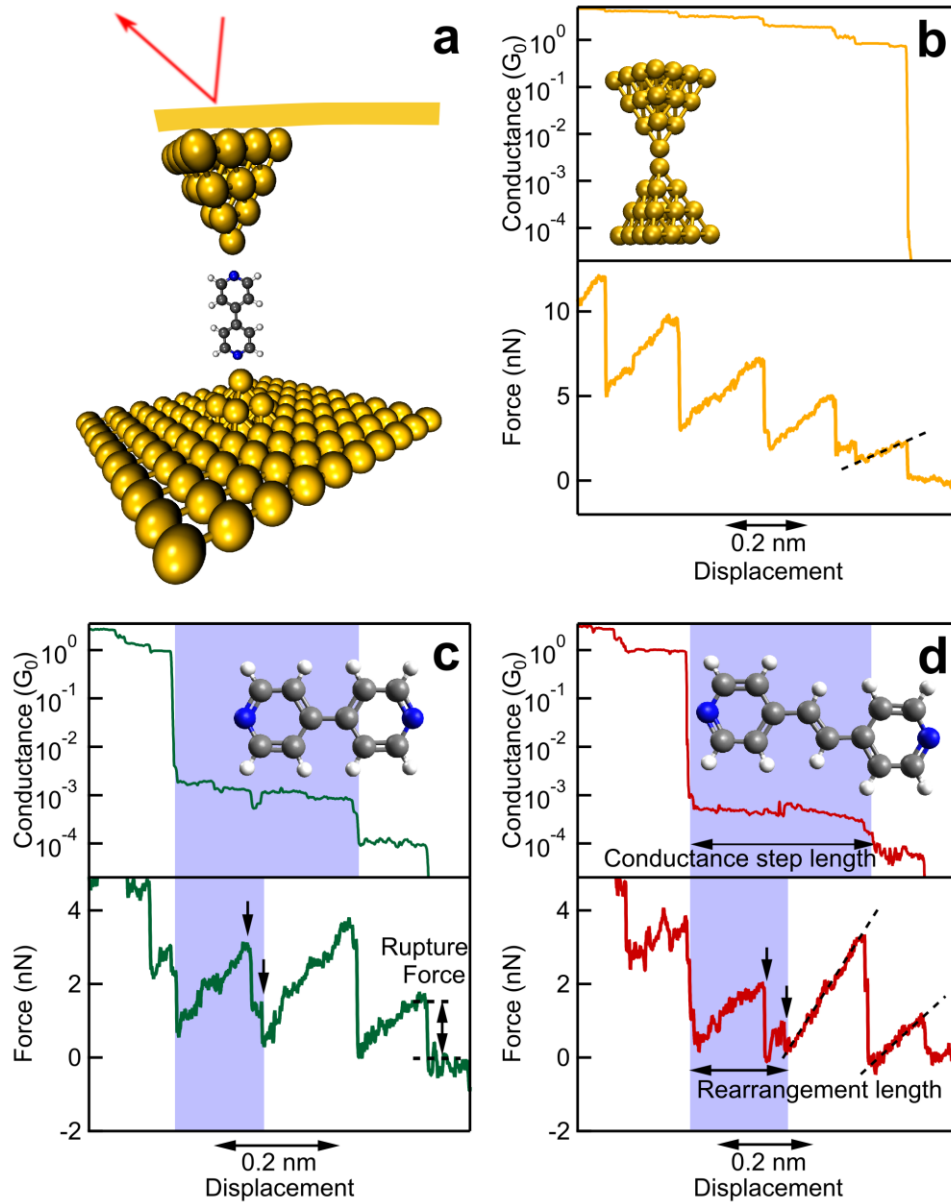
Figure 5.1. Simultaneous measurement of single molecule conductance and force. (a) Schematic representation of a BP junction formed between a gold coated AFM cantilever and a flat gold substrate. Experimentally measured conductance (upper panel) and corresponding simultaneously acquired force (lower panel) sample traces during junction elongation for clean Au (b), BP (c) and BPE (d) junctions. Shaded areas in upper panels represent high conductance molecular regimes. In lower panels, the shaded areas represent structural rearrangements within high conductance junctions that are clearly identified by abrupt force fluctuations (downward pointing arrows). Rupture force is the drop in force when the junction ruptures to an open junction, and stiffness is the slope of fitted lines.

force (lower panel) during the evolution of a Au quantum point-contact under elongation. The

conductance traces shows plateaus at integer multiples of G_0 ($2e^2/h$, quantum of conductance) as

the Au point-contact thins and ruptures. When the same measurements are carried out in the presence of BP or BPE molecules on the Au substrate, additional conductance plateaus are seen in the traces at conductance values that are characteristic of a single Au-molecule-Au junction. Previous work has shown that pyridine terminated molecules bind to the gold electrodes in two distinct geometries, each with a characteristic conductance dictated primarily by the separation between the two electrodes [10-12]. A high conducting junction (BP_H or BPE_H) is formed when the electrode separation is smaller than the length of the molecule. Upon elongation, this junction can rearrange to form a low-conducting junction (BP_L or BPE_L). The upper panels of Figure 5.1c,d show the conductance evolution of an Au point-contact in the presence of BP and BPE as a function of elongation. We see a plateau around $1G_0$, followed by a sequence of two plateaus at lower conductance values indicating that the Au single-atomic contact ruptures to form a BP_H or BPE_H junction, which rearranges to a BP_L or BPE_L plateau. The distance over which the junction remains in the high conducting state is highlighted in the upper panels of Figure 5.1c and Figure 5.1d, and defines the high conductance step length. Statistically, we find signatures of the high conductance junctions in ~80% of the measured traces, and these features always precede the low conductance junctions, when present. BP_H and BPE_H can also rupture upon elongation without switching to their respective low conductance states. Once the Au-molecule-Au junction is fully ruptured, no current is measured between the tip and surface.

The simultaneously acquired force traces (lower panels of Figure 5.1b-d) show repeated saw-tooth patterns, where each linear force ramp is indicative of elastic stretching of the junction with its characteristic stiffness (the slope of this ramp), while the drops in forces correspond to abrupt events involving bond rupture and junction rearrangements[13-16]. These force traces also clearly demonstrate typical rupture events that occur when the BP_H (BPE_H) junction

switches to a BP_L (BPE_L) junction. Although most abrupt force drops coincide with changes in conductance, we find that structural rearrangements frequently occur during the elongation of the BP_H and BPE_H junctions, without significant conductance variations, as illustrated in Figure 5.1c,d. Several distinct load-rupture saw-tooth events are seen in these force traces during the span of one BP_H/BPE_H conductance plateau. The distance over which these junctions rearrange before the final load/rupture event is highlighted in the lower panels of Figure 5.1c,d and defines the rearrangement length. While it has been common to assume that a conductance plateau corresponds to the stretching of a single bonding motif[17, 18], these observations demonstrate that conductance plateaus can span a sequence of local junction structures[19]. Here the simultaneously measured force provides an independent local probe of structural rearrangement.

5.2   Rupture forces, junction stiffness and structural rearrangements

We measure and analyze thousands of individual force and simultaneously acquired conductance measurements to determine junction rupture forces (force drops in individual traces) and junction stiffness (slope of the force ramps). We use conductance as the fingerprint and focus on three distinct regimes during junction elongation: a) Au single-atomic contacts, b) low conducting BP_L or BPE_L junctions and c) high conducting BP_H or BPE_H junctions that rupture to an open junction (see methods section for details). Histograms of force and stiffness values for these three cases are shown in Figure 5.2a and Figure 5.2b, respectively. We find that Au single-atomic contacts rupture with an average force of 1.5 nN and have an average effective stiffness of 8 N/m in excellent agreement with previously published results[13-15]. The errors in the peak positions of force and stiffness are dominated by the experimental uncertainty of AFM cantilever calibrations (see Chapter 2, Section 2.6). The widths of the distributions, on the other hand, are representative of intrinsic junction to junction variations that are found even in measurements

carried out at 4.2K in vacuum[13, 14]. The rupture force and stiffness are extremely sensitive to the details of the sampled potential energy landscapes[15, 16]. The measurements of sufficiently large datasets, as presented here, provide a statistically meaningful comparison between junctions that are different both chemically and physically.
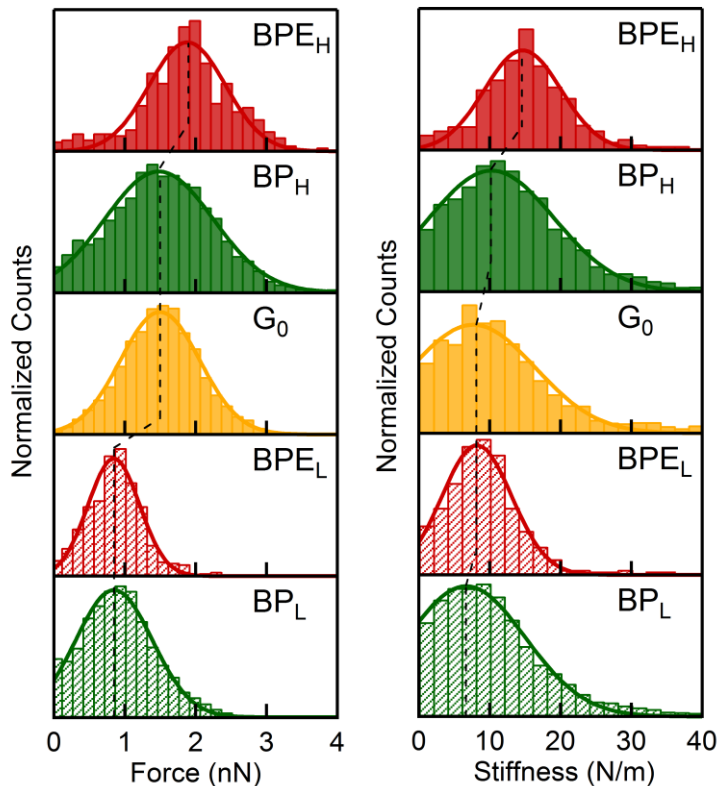
Figure 5.2. Rupture force and stiffness of single molecule junctions. Histograms of (a) rupture forces and (b) effective stiffness for BPL (shaded green; mean rupture force $F_{rup}= 0.85 \pm 0.01$ nN, mean stiffness $K_{junc} = 6.7 \pm 0.1$ N/m, number of measurements represented N = 7763), BPE_L (shaded red; $F_{rup} = 0.85 \pm 0.01$ nN, $K_{junc} = 8.2 \pm 0.1$ N/m, N = 501), Au (yellow; $F_{rup} = 1.50 \pm 0.01$ nN, $K_{junc} = 7.7 \pm 0.3$ N/m, N = 2346), BP_H (green; $F_{rup} = 1.48 \pm 0.01$ nN, $K_{junc} = 10.2 \pm 0.2$ N/m, N = 4118) and BPE_H (red; $F_{rup} = 1.88 \pm 0.02$ nN, $K_{junc} = 14.6 \pm 0.2$ N/m, N = 530) junctions. Dashed lines connecting the peaks of the distributions are provided as visual guides.

The low conducting BP_L and BPE_L junctions both rupture at ~0.8 nN in excellent agreement with previously published experimental measurements[14, 20] and adiabatic trajectory calculations performed with density functional theory (DFT) based methods for BP_L

junctions[14, 16]. These junctions typically show a single load-rupture saw-tooth in force, and exhibit a shorter conductance step (95th percentile length is ~ 0.1 nm) than the high conducting junctions, consistent with the stretching and rupture of the N-Au bond. Both the BP_L and BPE_L junctions have a similar stiffness (7 N/m and 8 N/m respectively), close to that of Au single-atomic contacts (8 N/m). Junction stiffness, in a simplified picture, corresponds to the effective spring constant of the entire metal-molecule-metal junction, where each bond can be modeled as a spring. Within this picture, the stiffness of a Au-molecule-Au junction, where the molecule is bonded to only one Au atom on each electrode apex, can only be equal to or smaller than that of an Au single-atomic contact. The stiffness measurements for BP_L and BPE_L are therefore consistent with geometries where the molecule bridges the apex of both electrodes through the formation of an Au-N donor-acceptor bond[11, 14, 16]. In contrast, the high-conducting BP_H and BPE_H junctions have an average rupture force of 1.5 nN and 1.9 nN which is equal to or larger than that of the single Au atomic contact. Although the average value for the BP_H junction is similar to that for the single Au contact, the larger average rupture force measured with BPE_H rules out an explanation of these experimental measurements based on Au-Au bond rupture. Since both molecules have the same terminal groups, the significantly larger rupture forces measured here for the high-conducting junctions demonstrate a binding mechanism that goes beyond the specific Au-N bond interaction. The measured stiffness for BP_H and BPE_H junctions are 10 N/m and 15 N/m respectively, both higher than the stiffness of the single Au atom contacts. Considered within the spring model discussed above, these large stiffness values imply significantly different molecule-electrode interactions involving additional binding mechanism.

To understand better the structure of these high-conductance junctions we focus now on the structural rearrangement signatures measured in the force trace within BP_H and BPE_H

junctions. We see saw-tooth features in addition to the final force drop due to rupture or switching of the junction to the low conducting state (lower panels of Figure 5.1c and Figure 5.1d). These additional events in force indicate that these high conductance junctions undergo a sequence of structural rearrangements, with little impact on the conductance. The final stable high conductance structure exists only over a relatively small fraction of the conductance plateau, given by the difference between the conductance step length and the rearrangement length as defined above. In Figure 5.3, we show histograms of the conductance step lengths and the rearrangement lengths for BP_H and BPE_H junctions. These distributions, which are peaked at 0.15 nm and 0.26 nm for BP_H and BPE_H respectively, show that a large fraction of the high conductance steps (~88% of BP_H and ~95% of BPE_H) undergo structural rearrangements. Although these rearrangements could be due to chain formation in the Au electrodes[21], the high stiffness measured in these structures rules out this explanation. This shows that the molecule is changing its attachment point on the electrode under stress and/or causes the motion of local Au atoms[22], consistent

Figure 5.3. Structural rearrangements in high-conducting junctions. Conductance step length and rearrangement length distributions for (a) BPE_H and (b) BP_H junctions show that only a small fraction of junctions are comprised of a single stable structure during elongation (counts near zero rearrangement length). Dashed lines are Gaussian fits to the non-zero portions of rearrangement length distributions.

with the fact that the rearrangement length scales with the length of the molecule[19].

Taken together, the rupture force, stiffness and rearrangement length measurements allow us to deduce a model for junction formation and evolution as illustrated in Figure 5.4a. An Au
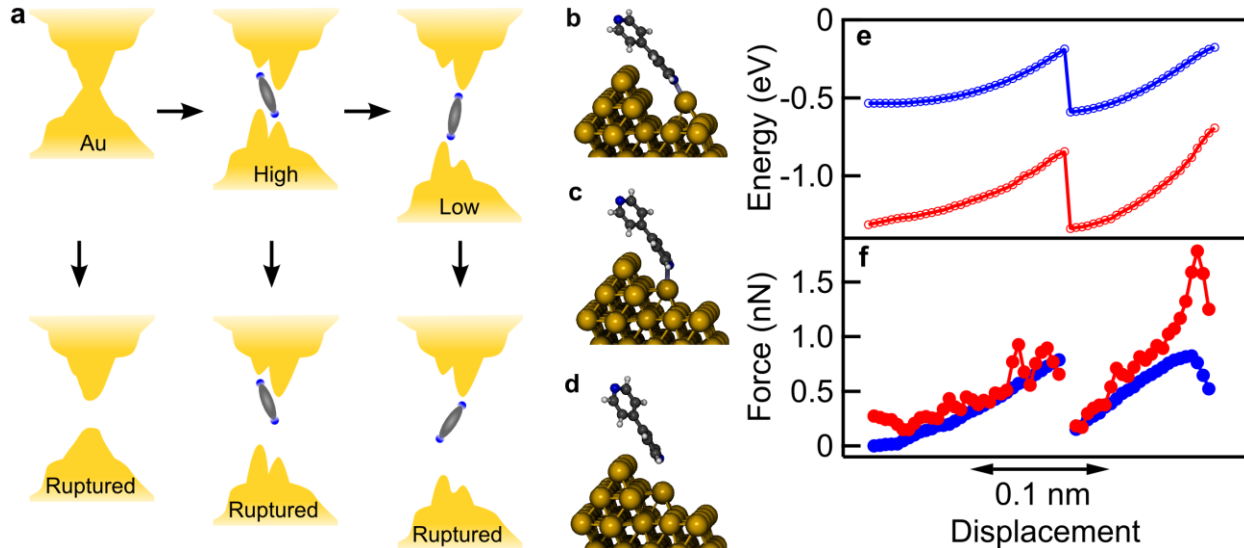
Figure 5.4. Structural evolution during junction elongation. (a) Schematic of structural evolution pathways deduced from experimental observations. In addition to rupture, the high conductance junctions show structural rearrangement and switching to the low conductance structures. (b) Model structure suitable for DFT calculations in which the BP adopts a tilted configuration due to constraints of junction formation and in which significant contribution from dispersion interactions of the aromatic ring with the atomic-scale roughness can be probed. (c) Upon elongation, a structural rearrangement event that retains the specific Au-N bond is accompanied by a large force drop. (d) Further elongation of the final stable structure results in the rupture of the Au-N bond. Calculated energies (e) and forces (f) with (red) and without (blue) inclusion of dispersion effects demonstrates the significant contributions from dispersion interactions. The electrode reference energy is taken to be the final electrode structure in (d). The binding energy relative to the initial electrode structure in (b) is 0.45 eV stronger giving an initial binding energy prior to rearrangement of 1.8 eV.

quantum point-contact is first formed between two electrode surfaces. Upon rupture, the electrode surfaces present both undercoordinated Au sites that support specific N-Au donor-acceptor bonds, as well as larger Au structures[23] that interact with the pyridine rings through non-specific van der Waals (vdW) interactions (both electrostatic and non-local London dispersion interactions). These conditions are optimal for the formation of a high-conducting junction. As this junction evolves under stress, it can either rupture or switch into the low-

conducting junction. This is consistent with past work where it was shown that the high-conducting junction results when the electrode separation is smaller than the molecule length, while low-conducting junctions appear to occur with the molecule bridging the apex atoms on the electrodes[11].

5.3   Density functional theory simulations and comparison to experiment

To understand the mechanics in more detail, we use DFT-based calculations to explore several bonding scenarios while also including the role of the dispersion interactions, the non-local correlation contribution not captured in typical DFT implementations, within the DFT-D2 approach[24] (see Section 5.4). We first consider the impact of dispersion interactions on the mechanics of low-conducting junctions. Previous DFT based calculations have focused on the chemically specific N-Au donor-acceptor bond in idealized BP_L junctions.[14, 16] We revisit several prototypical structures for BP bound to a single Au-atom (see Section 5.4) and compare DFT results with those that include dispersion interactions. We find that the inclusion of the dispersion interactions leads to small increases in the bond rupture force (less than 0.2 nN). In these geometries the specific chemical interaction of the donor-acceptor bond dominates and hence gradient corrected DFT calculations[25] without dispersion interactions are sufficient to characterize the binding.

To model the high-conducting geometry we consider an electrode surface that is illustrated in Figure 5.4b, where the rough electrode surface is modeled by an asperity consisting of a two-atom high ridge. The BP molecule is bonded to an adatom near a two-layer ridge. The tilt of the BP molecule backbone models the constraint of bonding to the other electrode (implicit here and simulated by control of the position of the upper N atom). The chemical N-Au donor-

acceptor bond strength is found to be about 1 eV. In addition, due to the proximity of the ridge structure, the dispersion interaction contributes an additional 0.8 eV to the binding energy. The junction elongation is simulated by moving the molecule vertically upwards in increments of 0.01 Å followed by a relaxation with the upper (unbound) N fixed (Figure 5.4b-f). After an elongation of 0.16 nm there is an abrupt structural rearrangement: the molecule pulls the adatom to an adjacent hollow site while maintaining the Au-N bond intact (Figure 5.4c). The calculated force drop for this event is about 0.8 nN, consistent with the force drops accompanying structural rearrangements in the experiment (Figure 5.1c,d). As the junction is elongated, the ring passes the edge of the asperity and the loss of vdW interaction energy contributes significantly to the maximum sustained force of 1.8 nN (Figure 5.4d), in good agreement with the experimental results. The dispersion contributions account for 1 nN for this specific trajectory. Overall, the contribution of non-specific, vdW interactions (electrostatic plus dispersion) to the maximum sustained force is sensitive to the interplay between the local N-Au bond elongation during rupture and the coordination of the ring to the ridge structure; the vdW contribution is likely between 0.4 to 1 nN.

The key results of the calculations are twofold: (1) in the low-conductance BP_L junctions, the dispersion contribution is minimal and (2) in the high-conductance BP_H junctions, both chemically specific Au-N and vdW interactions need to be considered together to explain the experimentally measured rupture forces. For junctions with the longer BPE molecule, the specific chemical interactions are similar to BP, but the increased length can lead to more optimized vdW interactions of the pyridine rings with Au structures, longer sequences of structural rearrangement and to even larger rupture force and stiffness compared to BP, as observed in the experiment. Finally, the constrained geometry in Figure 5.4c results in the N-Au

bond being at a substantial angle to the plane of the pyridine ring, consistent with a link structure that was previously proposed to explain the high conductance junction[11]. In addition, the proximity of the C atoms in the pyridine ring to the top of the ridge structure (3.5 Å) facilitates enhanced electronic coupling[26] and is therefore expected to contribute to the higher conductance[22]. We have ruled out any appreciable mechanical stabilization due to specific Au-C bonding through control measurements with 4-phenylpyridine and 4-styrylpyridine molecules (see Section 5.4). These molecules have the same molecular structure as BP and BPE respectively, except there is a nitrogen atom on only one side of the molecule to form specific N-Au bonds. Neither of these molecules show well-defined conductance plateaus and force measurements with 4-styrylpyridine do not show any force saw-tooth events beyond the Au G_0 rupture. These results demonstrate that there are no independently formed Au-C bonds that are comparable in strength to the chemical Au-N interactions seen in these systems.

In summary, we have used an atomic force microscope to probe the interplay between specific Au-N and non-specific van der Waals interactions between the surface structure on the Au electrode and two pyridine terminated molecules. Our results provide a unique quantitative measurement of the relative importance of these two types of interfacial interactions at the single-molecule level, in a regime where they are of comparable magnitude. These results will have particular impact on the drive to develop accurate theoretical treatment of van der Waals interactions at metal-molecule interfaces currently in a nascent stage, and especially to go beyond the simplest model systems of ideal, flat surfaces towards the treatment of nanostructured metals that are critical to many areas of research and future technological applications.

5.4 Supporting information

DFT Calculations: The BP interaction with the Au electrode was modeled with a periodic slab geometry consisting of three monolayers of (111) oriented Au plus ad-structures and the molecule. The surface unit cell for the ridge plus adatom structure illustrated in Figure 5.4 was 5×5. The vertical distance between the upper N atom and the bottom Au layer in the periodic supercell was at least 13 Å. During simulation, the two back layers atoms in the Au slab were held fixed with a bulk lattice parameter of 4.13 Å. All other degrees of freedom were relaxed until all forces were less than 0.01 eV/Å for each structure. We focus on one side of the junction, considering only one N-Au link bond, and fix the position of the other N atom in the BP molecule to define a specific value of elongation. The junction was elongated in steps of 0.01 Å by shifting the BP molecule relative to the slab. Data is recorded for every 0.05 or 0.1 Å of shift with a force criterion for structural relaxation enforced. Most of the calculations to date in the literature consider molecules on flat metal surfaces. We find a strong influence of the additional Au-Au interactions on the ad-structures (pyramid and ridge). Therefore, we use a perturbative approach, as has been done in other studies involving undercoordinated metal structures[27].

To estimate the role of van der Waals interactions in the bond rupture process, the semi-empirical Grimme DFT-D2 approach[24] to correct the PBE version of the generalized gradient approximation[28] as implemented in the VASP package[29] has been employed. Several estimates for the C6 coefficient for Au appear in the literature[7, 30, 31] ranging from 220 to 615 eV-$Å^6$. We use $C_6 = 422$ eV-$Å^6$ with $R_0 = 1.772$ Å. The additional Au-Au interaction is relatively strong. As noted in the context of the recently revised Tkatchenko-Scheffler semiempirical scheme, the effect of screening is important in the metal[8]. In the DFT-D2 approach, we limit the range of the d^{-6} interactions with a relatively short cut-off (6 Å). The bulk fcc lattice

parameter for Au is calculated to be 4.13 Å with these parameters in the DFT-D2 scheme, about 1% larger than experiment. The generalized gradient approximation (PBE) gives 4.17 Å, indicative of the extra attractive interaction in the DFT-D2 scheme. The periodic slabs in the supercell geometry employed assure more than 10 Å separation between the tip of the molecule and the first layer of Au in the next cell above. The lateral cells employed (4x5 and 5x5) for the bipyridine studies assure that the interaction between the additional dipole associated to the N-Au donor-acceptor bond in the primary cell and those in the periodic replicas contribute less than 0.05 eV to the binding energy. This conservative estimate is based on our prior analysis of ammonia bonding to an Au adatom[32] and $1/d^{-3}$ scaling. Finally, the use of a 3 ML Au slab is consistent with the relatively short cut-off used in the DFT-D2 approach. Further, single point calculations indicate that an additional Au layer has a minimal impact on the binding energy (<0.05 eV).

For calibration, we considered the adsorption energy of benzene flat on the Au(111) surface. We found a relatively reasonable adsorption energy, 0.88 eV, with the benzene at 3.0 Å above the plane of the surface. These results are close to those reported for benzene on Ag(111) (0.81 eV and 2.93 Å) using the new Tkatchenko-Scheffler scheme. Application of an approach based on the van der Waals Density Functional approach[33] gave weaker binding (0.42 eV and 3.7 Å)[34]. A desorption energy of 0.64 eV has been estimated from temperature programmed desorption (TPD) experiments[35]. There is some evidence that the standard choice of prefactor (1×10^{13} s^{-1}) is too small for larger molecules[8, 36]. With values as high as 1×10^{18} s^{-1}, the estimated desorption energy could be as large as 0.88 eV. This test suggests that the DFT-D2 approach overestimates van der Waals interactions involving Au for this parameter set. For a

single ring, the error could be as much as 0.24 eV, depending on the interpretation of the TPD experiments.

Our previously published calculations of adiabatic trajectories for 4,4'-bipyridine were based on pyramidal cluster models for the tips (20 Au atoms for each tip) and designed to simulate the low conductance configuration in the experiments; dispersion interactions were not considered[14]. When focusing on a single link bond to the apex of a symmetric pyramid and with the backbone of the BP oriented vertically, a maximum sustained force of 1.11 nN was calculated (Table 5.1). Here we perform similar calculations with a slab model plus a small pyramidal tip (4 atom) in a 4×5 surface unit cell. These trajectories are calculated with steps of 0.1 Å or 0.2 Å and structure relaxation to a force criterion of 0.03 eV/Å at each step. The backbone is initially tilted about 20 degrees from normal and a similar force results (Table 5.1). For a single adatom tip, the binding energy is larger and the maximum sustained force increases to 1.5 nN (Figure 5.5). Interestingly, for this modest backbone tilt angle, there is a step in the trajectory where the adatom jumps to an adjacent hollow site. This illustrates that details of the Au atomic structure near the link bond point affect binding energy and hence maximum sustained force, as one would expect on general grounds. When the dispersion interaction is included as a perturbative correction using the structure optimized with PBE only, the maximum sustained force increases slightly (0.14 nN and 0.18 nN for the 4 atom pyramid and the adatom respectively). As a comparison, a trajectory for the adatom tip was also computed with the dispersion interaction included in the geometry optimization. The binding energy and maximum force are very similar, although the adatom does not shift due to its stronger adhesion to the surface within the Grimme scheme.

Table 5.1. Comparison of binding energy and maximum sustained force for a series of link-electrode structures and computational approaches.

Configuration / Theory	Binding Energy (eV)	Maximum Force (nN)
Pyramid model / PBE	0.75	1.11
Slab + 4 atom tip / PBE	0.81	1.12
Slab + adatom tip / PBE	0.97	1.5
Slab + 4 atom tip / PBE + vdW (geo PBE)	0.96	1.26
Slab + adatom tip / PBE + vdW (geo PBE)	1.16	1.68
Slab + adatom tip / PBE + vdW (geo PBE+vdW)	1.14	1.69
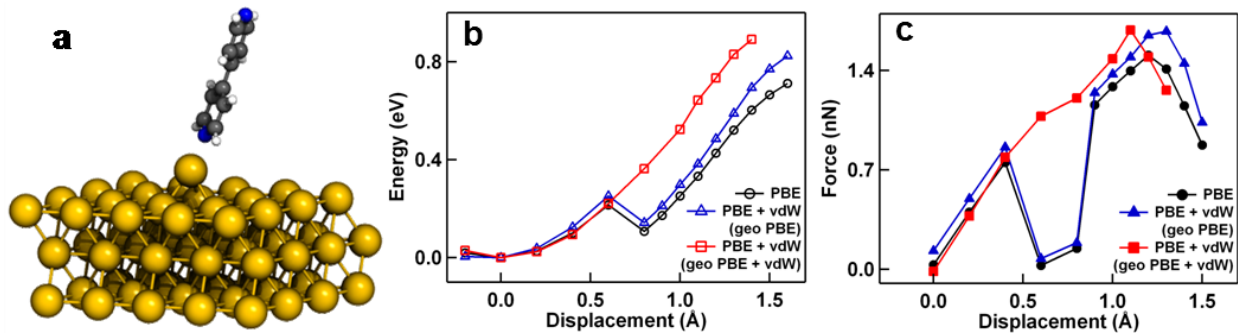
Figure 5.5. DFT adatom geometry calculations. (a) Relaxed structure near minimum energy for the adatom tip model. Energy (b) and force (b) versus elongation (zero taken from the minimum energy point) with three approximations: PBE, PBE+vdW (geometry optimization with PBE), and PBE+vdW (geometry optimization with PBE including vdW forces).

Control experiments: We have carried out control measurements with 4-phenyl-pyridine (PP) and 4-styryl pyridine (SP) (obtained from Sigma Aldrich). These are analogous to BP and BPE, respectively, except that they have a pyridine group on only one end and a phenyl group on the other end. The conductance measurements with these compounds did not show well-defined conductance plateaus and no clear peaks appear in the linear binned conductance histograms

(Figure 5.6a). This demonstrates that no well-defined conducting junctions are formed with molecules that have only one pyridine link. Force measurements from the longer compound (SP)
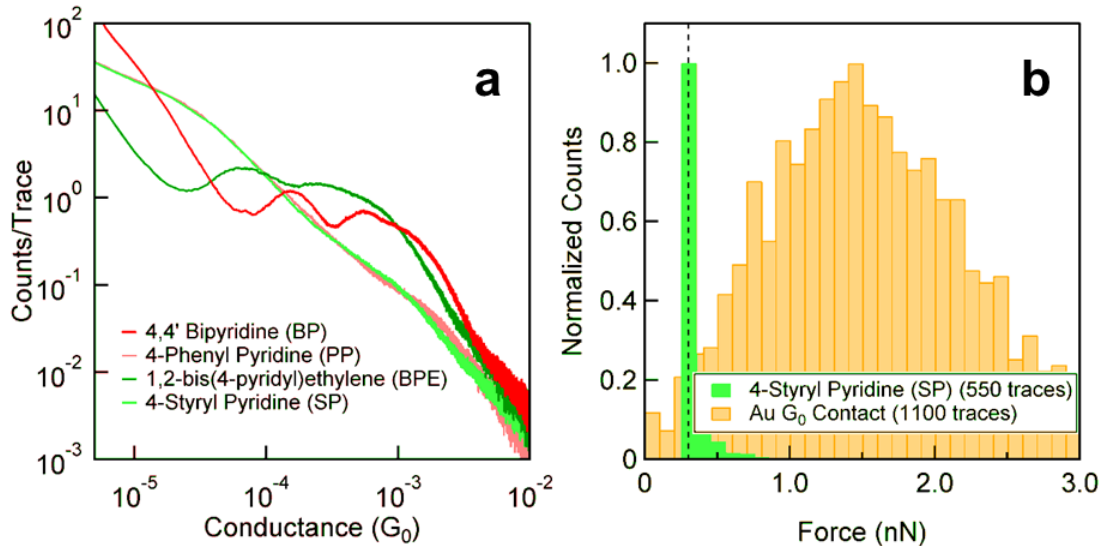
Figure 5.6. Force and conductance data from control experiments. (A) Conductance histogram for BP, PP, BPE, and SP generated from over 6000 traces, using linear bins of width 10^{-6} G_0. (B) Histogram of forces measured in the presence of SP for the G_0 single atom contact (in yellow) and for the largest force event greater or equal to a preset threshold value of 0.3 nN (dashed line) measured beyond the G_0 contact rupture.

do not show any saw-tooth rupture events beyond the Au G_0 rupture. Using a force event detection algorithm as detailed in our previous work[37] (see also Chapter 2, Section 2.7), the rupture force distribution in Figure 5.6b shows that a negligible fraction of traces have force events beyond the set threshold value of 0.3 nN (~2× standard deviation of instrument noise). If specific Au-C interaction were the sole reason for the observed large rupture force of BPE, their presence would be expected to result in a measurable rupture force for SP. Finally these control measurements with SP show that in this case, non-specific vdW interactions are not sufficient to form junctions with well-defined conductance plateaus or force events at room temperature.

Force summary: Table 5.2 summarizes the mean values of measured forces and stiffness for Au G_0, BP_H and BP_L junctions, including BP_H-BP_L switching. The switching force is defined as the difference between the force value just before rupture of the BP_H junction and the value just after switching to the BP_L junction (for instance in Figure 5.1c). The non-zero switching force implies that the high and low conductance structures are indeed significantly different, and that the switching between these two states involves an abrupt structural change. We note that the relatively large starting forces indicate that, on average, the junctions form under a non-zero tensile stress. We also observe that there is only slight difference in rupture force and stiffness between those BP_H junctions that rupture and those that switch to the low conductance state, indicating that their binding is not significantly different.

Table 5.2. Summary of forces and stiffness of various Au and BP junction evolution scenarios.

Scenario	Rupture Force (nN)	Stiffness (N/m)	Starting Force (nN)	Switching Force (nN)
Au G_0–rupture	1.50 ± 0.01	7.7 ± 0.3	1.07 ± 0.01	
BP_H–rupture	1.48 ± 0.01	10.2 ± 0.2	0.73 ± 0.01	
BP_L–rupture	0.85 ± 0.01	6.7 ± 0.1	0.52 ± 0.01	
BP_H–switch–BP_L	1.31 ± 0.02	9.3 ± 0.2		0.60 ± 0.02

5.5 References

1. J.K. Norskov, T. Bligaard, J. Rossmeisl, and C.H. Christensen, *Towards the computational design of solid catalysts.* Nature Chemistry, 2009. **1**(1): p. 37-46.

2.   K. Moth-Poulsen and T. Bjornholm, *Molecular electronics with single molecules in solid-state devices.* Nature Nanotechnology, 2009. **4**(9): p. 551-556.

3.   L. Bartels, *Tailoring molecular layers at metal surfaces.* Nature Chemistry, 2010. **2**(2): p. 87-95.

4.   F. Cunha, N.J. Tao, X.W. Wang, Q. Jin, B. Duong, and J. DAgnese, *Potential-induced phase transitions in 2,2'-bipyridine and 4,4'-bipyridine, monolayers on Au(111) studied by in situ scanning tunneling microscopy and atomic force microscopy.* Langmuir, 1996. **12**(26): p. 6410-6418.

5.   T. Wandlowski, K. Ataka, and D. Mayer, *In situ infrared study of 4,4 '-bipyridine adsorption on thin gold films.* Langmuir, 2002. **18**(11): p. 4331-4341.

6.   G. Mercurio, E.R. McNellis, I. Martin, S. Hagen, F. Leyssner, S. Soubatch, J. Meyer, M. Wolf, P. Tegeder, F.S. Tautz, and K. Reuter, *Structure and Energetics of Azobenzene on Ag(111): Benchmarking Semiempirical Dispersion Correction Approaches.* Physical Review Letters, 2010. **104**(3): p. 036102.

7.   K. Tonigold and A. Gross, *Adsorption of small aromatic molecules on the (111) surfaces of noble metals: A density functional theory study with semiempirical corrections for dispersion effects.* Journal of Chemical Physics, 2010. **132**(22): p. 224701.

8.   V.G. Ruiz, W. Liu, E. Zojer, M. Scheffler, and A. Tkatchenko, *Density-Functional Theory with Screened van der Waals Interactions for the Modeling of Hybrid Inorganic-Organic Systems.* Physical Review Letters, 2012. **108**(14): p. 146103.

9.   G. Li, I. Tamblyn, V.R. Cooper, H.-J. Gao, and J.B. Neaton, *Molecular adsorption on metal surfaces with van der Waals density functionals.* Physical Review B, 2012. **85**(12): p. 121409.

10.   E.S. Tam, J.J. Parks, W.W. Shum, Y.-W. Zhong, M.E.B. Santiago-Berríos, X. Zheng, W. Yang, G.K.L. Chan, H.c.D. Abruña, and D.C. Ralph, *Single-Molecule Conductance of Pyridine-Terminated Dithienylethene Switch Molecules.* ACS Nano, 2011. **5**(6): p. 5115-5123.

11.   S.Y. Quek, M. Kamenetska, M.L. Steigerwald, H.J. Choi, S.G. Louie, M.S. Hybertsen, J.B. Neaton, and L. Venkataraman, *Mechanically controlled binary conductance switching of a single-molecule junction.* Nature Nanotechnology, 2009. **4**(4): p. 230-234.

12.   W. Hong, D.Z. Manrique, P. Moreno-García, M. Gulcur, A. Mishchenko, C.J. Lambert, M.R. Bryce, and T. Wandlowski, *Single Molecular Conductance of Tolanes: Experimental and Theoretical Study on the Junction Evolution Dependent on the Anchoring Group.* Journal of the American Chemical Society, 2011. **134**(4): p. 2292-2304.

13. G. Rubio-Bollinger, S. Bahn, N. Agraït, K. Jacobsen, and S. Vieira, *Mechanical Properties and Formation Mechanisms of a Wire of Single Gold Atoms.* Physical Review Letters, 2001. **87**(2): p. 026101.

14. M. Frei, S.V. Aradhya, M. Koentopp, M.S. Hybertsen, and L. Venkataraman, *Mechanics and chemistry: single molecule bond rupture forces correlate with molecular backbone structure.* Nano Letters, 2011. **11**(4): p. 1518-1523.

15. M.R. Sørensen, M. Brandbyge, and K.W. Jacobsen, *Mechanical deformation of atomic-scale metallic contacts: Structure and mechanisms.* Physical Review B, 1998. **57**(6): p. 3283-3294.

16. R. Stadler, K. Thygesen, and K. Jacobsen, *Forces and conductances in a single-molecule bipyridine junction.* Physical Review B, 2005. **72**(24): p. 241401.

17. Z.F. Huang, B.Q. Xu, Y.C. Chen, M. Di Ventra, and N.J. Tao, *Measurement of current-induced local heating in a single molecule junction.* Nano letters, 2006. **6**(6): p. 1240-1244.

18. M. Tsutsui, M. Taniguchi, and T. Kawai, *Atomistic Mechanics and Formation Mechanism of Metal-Molecule-Metal Junctions.* Nano letters, 2009. **9**(6): p. 2433-2439.

19. M. Kamenetska, S.Y. Quek, A.C. Whalley, M.L. Steigerwald, H.J. Choi, S.G. Louie, C. Nuckolls, M.S. Hybertsen, J.B. Neaton, and L. Venkataraman, *Conductance and Geometry of Pyridine-Linked Single-Molecule Junctions.* Journal of the American Chemical Society, 2010. **132**(19): p. 6817-6821.

20. B.Q. Xu, X.Y. Xiao, and N.J. Tao, *Measurements of single-molecule electromechanical properties.* Journal of the American Chemical Society, 2003. **125**(52): p. 16164-16165.

21. A.I. Yanson, G.R. Bollinger, H.E. van den Brom, N. Agrait, and J.M. van Ruitenbeek, *Formation and manipulation of a metallic wire of single gold atoms.* Nature, 1998. **395**(6704): p. 783-785.

22. J.S. Meisner, M. Kamenetska, M. Krikorian, M.L. Steigerwald, L. Venkataraman, and C. Nuckolls, *A Single-Molecule Potentiometer.* Nano Letters, 2011. **11**(4): p. 1575-1579.

23. H. Ohnishi, Y. Kondo, and K. Takayanagi, *Quantized conductance through individual rows of suspended gold atoms.* Nature, 1998. **395**(6704): p. 780-783.

24. S. Grimme, *Semiempirical GGA-type density functional constructed with a long-range dispersion correction.* Journal of Computational Chemistry, 2006. **27**(15): p. 1787-1799.

25. A. Bilic, J.R. Reimers, and N.S. Hush, *Adsorption of pyridine on the gold(111) surface: Implications for ̆alligator clips"for molecular wires.* Journal of Physical Chemistry B, 2002. **106**(26): p. 6740-6747.

26. S.T. Schneebeli, M. Kamenetska, Z.L. Cheng, R. Skouta, R.A. Friesner, L. Venkataraman, and R. Breslow, *Single-Molecule Conductance through Multiple pi-pi-Stacked Benzene Rings Determined with Direct Electrode-to-Benzene Ring Connections.* Journal of the American Chemical Society, 2011. **133**(7): p. 2136-2139.

27. A.K. Kelkkanen, B.I. Lundqvist, and J.K. Norskov, *Van der Waals effect in weak adsorption affecting trends in adsorption, reactivity, and the view of substrate nobility.* Physical Review B, 2011. **83**(11): p. 113401.

28. J.P. Perdew, K. Burke, and M. Ernzerhof, *Generalized gradient approximation made simple.* Physical Review Letters, 1996. **77**(18): p. 3865-3868.

29. G. Kresse and J. Furthmuller, *Efficient iterative schemes for ab initio total-energy calculations using a plane-wave basis set.* Physical Review B, 1996. **54**(16): p. 11169-11186.

30. J. Sławińska, P. Dabrowski, and I. Zasada, *Doping of graphene by a Au(111) substrate: Calculation strategy within the local density approximation and a semiempirical van der Waals approach.* Physical Review B, 2011. **83**(24): p. 245429.

31. K. Toyoda, I. Hamada, K. Lee, S. Yanagisawa, and Y. Morikawa, *Density functional theoretical study of pentacene/noble metal interfaces with van der Waals corrections: Vacuum level shifts and electronic structures.* Journal of Chemical Physics, 2010. **132**(13).

32. M.S. Hybertsen, L. Venkataraman, J.E. Klare, A.C. Whalley, M.L. Steigerwald, and C. Nuckolls, *Amine-linked single-molecule circuits: systematic trends across molecular families.* Journal of Physics-Condensed Matter, 2008. **20**(37).

33. M. Dion, H. Rydberg, E. Schroder, D.C. Langreth, and B.I. Lundqvist, *Van der Waals Density Functional for General Geometries.* Physical Review Letters, 2004. **92**(24): p. 246401.

34. J. Wellendorff, A. Kelkkanen, J.J. Mortensen, B.I. Lundqvist, and T. Bligaard, *RPBE-vdW Description of Benzene Adsorption on Au(111).* Topics in Catalysis, 2010. **53**(5-6): p. 378-383.

35. D. Syomin, J. Kim, B.E. Koel, and G.B. Ellison, *Identification of adsorbed phenyl (C6H5) groups on metal surfaces: Electron-induced dissociation of benzene on Au(111).* Journal of Physical Chemistry B, 2001. **105**(35): p. 8387-8394.

36. R.Z. Lei, A.J. Gellman, and B.E. Koel, *Desorption energies of linear and cyclic alkanes on surfaces: anomalous scaling with length.* Surface Science, 2004. **554**(2-3): p. 125-140.

37. S.V. Aradhya, J.S. Meisner, M. Krikorian, S. Ahn, R. Parameswaran, M.L. Steigerwald, C. Nuckolls, and L. Venkataraman, *Dissecting contact mechanics from quantum interference in single-molecule junctions of stilbene derivatives.* Nano Letters, 2012. **12**(3): p. 1643-7.

6

Correlating structure, conductance and mechanics

of silver atomic-scale contacts

While Au single atomic contacts have been well-studied, Ag remains challenging to study experimentally. Here we measure the conductance and force across silver atomic-scale contacts and find two additional conductance features at ~0.4 G_0 and ~1.3 G_0, beyond the 1 G_0 feature corresponding to the single atomic contact. Using a conductance cross-correlation technique, we distinguish three different atomic-scale structural motifs and analyze their rupture forces and stiffness. Combined with previous studies, our results allow us to assign the ~0.4 G_0 conductance feature to an Ag-O-Ag contact and the ~1.3 G_0 feature to an Ag-Ag single-atom contact with an oxygen atom in parallel. Utilizing complementary information from force and conductance, we thus demonstrate the correlation of conductance with the structural evolution at the atomic scale.

This work was performed in collaboration with Prof. Andras Halbritter, with experimental support from Dr. Michael Frei.

The electronic properties of metal single-atom contacts have been studied extensively using the mechanically controlled break-junction technique and the scanning tunneling microscope based break-junction technique[1]. The most commonly studied metal in such measurements is gold (Au) due to its chemical stability in ambient conditions, and its relative ease in metallizing various surfaces. Electronic measurements with a series of other metals have been carried out under ultra-high or high-vacuum conditions[2-8]; however, there are very few studies of the mechanical properties of these nanoscale wires and point-contacts for metals other than Au[9]. In this chapter, we present simultaneous force and conductance measurements of silver (Ag) atomic contacts and compare their properties with Au contacts. Whereas Au atomic contacts show a clear 1 G_0 ($G_0 = 2e^2/h$, the quantum of conductance) feature corresponding to the formation of single atomic contacts even under ambient conditions, Ag shows additional features at ~0.4 G_0 and ~1.3 G_0. Such conductance features have been observed in previous experimental studies[10-12], and theoretical investigations[13-16] have provided detailed insight into their structural origin. In particular, molecular O_2 is known to dissociate into atomic O and adsorb to undercoordinated Ag atoms, even at temperatures as low as 105 K[17-19]. An oxygen atom can therefore be expected to bond to the highly reactive Ag atomic-size contact, and bridge an Ag-Ag contact either in parallel or in series as Ag-O-Ag. Such events are more pronounced in Ag compared to Au, due to its higher reactivity[11, 20]. Measurements with Ag point contacts therefore present richer possibilities in structure and evolution under elongation when compared with Au single atomic contacts and also open up the possibility to study in-situ reactions that could lead to the formation of novel single-molecule junctions[21].

In this study, we measure, simultaneously, the electronic and mechanical properties of Ag point contacts using a custom atomic force microscope to probe the formation and evolution of

Ag contacts under ambient conditions. We measure thousands of junctions to carry out a statistical analysis in a robust manner. We find that during the thinning of Ag point contacts under junction elongation, there are not only conductance plateaus due to Ag single-atom contacts (with conductance of ~1 G_0), but also plateaus at ~0.4 G_0 and ~1.3 G_0 which we assign to the presence of atomic oxygen impurities. Although we cannot rule out the presence of other impurities in our experiments, our observed experimental evidence is consistent with previous experimental[10-12] and theoretical[13-16] studies which attribute these conductance features to atomic oxygen in Ag contacts. We use a cross-correlation technique[22, 23] to study the mutual conditional occurrence of these three conductance features in a statistically robust manner. The insights from these cross-correlations allow us to employ a simple algorithm to sort junctions based on their structures into three distinct groups: (a) junctions with a single Ag-atom contact (Ag-SAC) (b) a single Ag-atom contact with a parallel oxygen atom bridge (AgO-P) and (c) a single-Ag-atom contact incorporating an oxygen atom in series (AgO-S). We deduce the structural evolution pathways for these junctions and analyze the force data to quantify the mechanics of the three distinct contacts. We find that the 1 G_0 conductance features, which arise from Ag single atomic contacts, have a rupture force of 1 nN and a stiffness of 8 N/m. The 0.4 G_0 features, which are attributed to the configuration with an oxygen atom in series, have slightly lower rupture forces (0.8 nN) but have a stiffness (8 N/m) comparable to that of the single Ag-atom contact. In contrast, structures with oxygen in parallel (with a conductance of ~1.3 G_0) show a significantly higher rupture force (1.7 nN) and a higher stiffness (14 N/m). Together, these quantitative results not only represent the first direct measurement of the mechanics of Ag point-contacts, but also allow us to unambiguously conclude that the Ag-O bonds are comparable in strength to the Ag-Ag bonds and can mechanically stabilize them when in parallel.

6.1 Conductance features

We carry out simultaneous conductance and force measurements using an atomic force microscope based break-junction method (AFM-BJ). To gather larger statistics on conductance correlations, we also carry out conductance measurements alone in a scanning tunneling microscope based break-junction setup (STM-BJ)[24]. The AFM experimental setup and analytical procedures are detailed in the Methods section, and have also been described in detail previously[25, 26]. Briefly, a Ag coated AFM cantilever and a freshly mechanically polished Ag substrate are repeatedly brought in and out of contact using a high resolution piezo positioner at a constant velocity. Conductance is measured across the tip/sample junction at constant bias of 25 mV. The force is measured simultaneously by monitoring the deflection of a laser focused on the back of the cantilever as schematically illustrated in Figure 6.1a. Figure 6.2b shows conductance (red) and force (blue) measurements from a typical Ag junction elongation and rupture. Conductance decreases stepwise as a function of displacement, similar to what is observed for Au point-contacts[1]. The simultaneously measured force traces show a typical saw tooth pattern
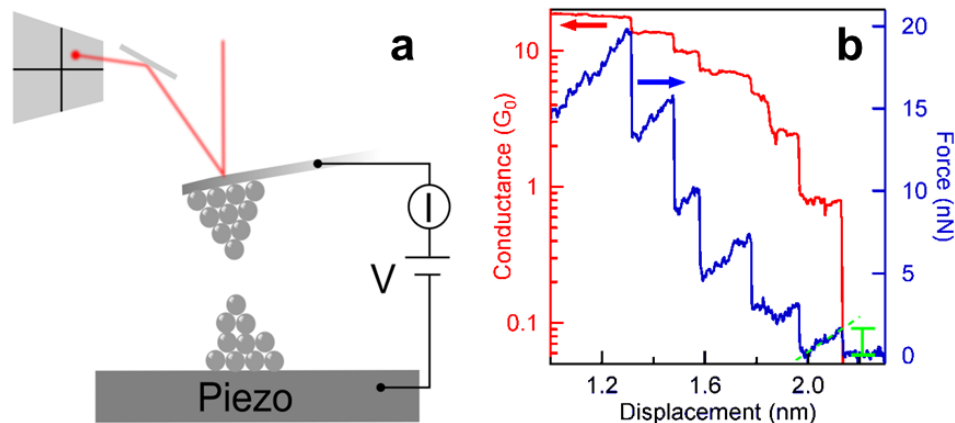
Figure 6.1. Experimental setup and sample simultaneously measured conductance and force data. (a) Schematic of the experimental setup used for simultaneous force and conductance measurements. (b) Sample trace showing the evolution of conductance (red, left axis) and force (blue, right axis) for an Ag point contact as a function of junction elongation. The drop in force at the end of the conductance step corresponds to the rupture force, while the slope of the force trace over the conductance plateau is related to the stiffness of the junction.

attributed to reversible (elastic) and irreversible (plastic) deformations[27].

To understand the details of the different conductance plateaus seen with these traces, we first collect a large data set of 10,000 Ag conductance traces with the STM-BJ setup as it is easier to gather large data sets with a Ag wire tip in the STM as opposed to using an Ag coated cantilever necessary for the AFM-BJ measurements. We analyze the conductance traces by creating a linear-binned histogram without data selection. Figure 6.2a compares 1D conductance histograms (normalized by the number of included traces) for Ag (grey) with that for Au (yellow). Both histograms reveal characteristic peaks at well-defined conductance values, although the peaks are more prominent for the Au measurements. As in Au, a 1 G_0 conductance plateau in Ag corresponds to a junction with a single conducting channel with unit transmission[8, 28-31]. However, it is known that Ag contacts do not form long single atomic chains[8, 28-31]; indeed, we see a reduced 1 G_0 peak as Ag plateaus are considerably shorter. Additionally, the Ag histogram peak does not show a clear peak around 1.8 G_0, unlike the Au histogram, but a peak around 2.5 G_0 is clearly visible. This higher conductance peak at ~2.5 G_0 has been attributed to a stable contact geometry with a triangular (3-atom) cross-section[8, 31]. The Ag measurements also show a large number of counts below 1 G_0, corresponding to larger through-space tunneling currents after junction rupture, indicating that the dynamics of the atomic-scale relaxation of Ag single-atom contacts immediately after rupture is different from Au contacts[12, 30, 32]. The presence of other adsorbates around the junction could also be responsible for the counts at lower conductance values in Ag junctions.

The Ag histogram in Figure 6.2a also shows a feature around 0.4 G_0 indicating that a frequent and stable configuration with that conductance is formed when Ag contacts are broken[10-12]. Since O_2 from the ambient environment can dissociate on under-coordinated
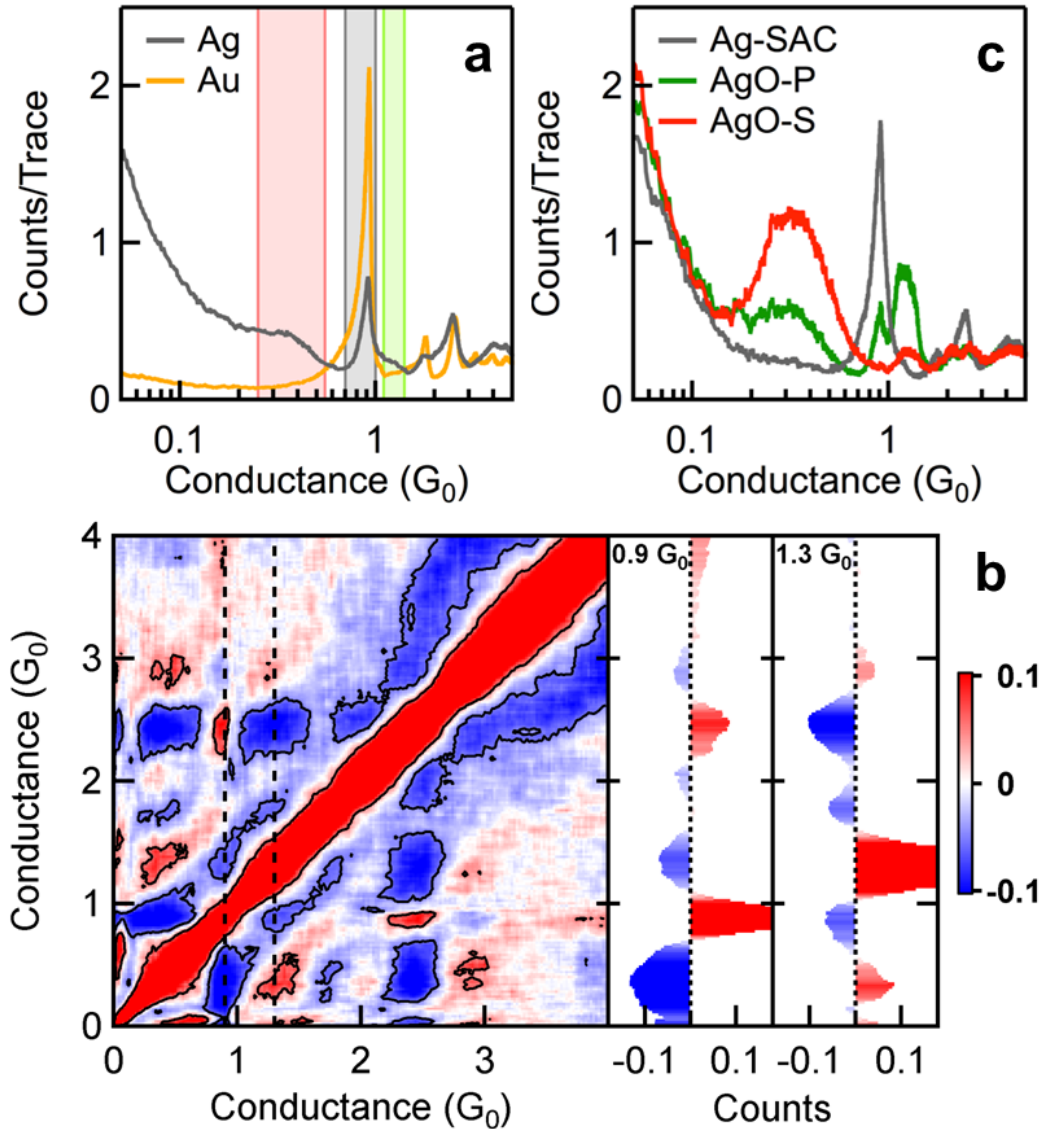
Figure 6.2. One-dimensional and two-dimensional cross-correlation conductance histograms. (a) One-dimensional conductance histograms (linearly binned, bin size 0.001 G_0) constructed without any data selection for 10,000 Ag (grey) traces; Au (gold) histogram is shown for comparison. These traces were measured with the STM-BJ setup. The highlighted regions indicate conductance ranges associated with AgO-S (red), Ag-SAC (grey) and AgO-P (green). (b) 2D cross-correlation histogram constructed without data selection for Ag traces. The panels on the right are profiles along the dotted lines shown on the cross-correlation histogram, at 0.9 G_0 and 1.3 G_0, respectively. The scale bar indicates the color scale used for the correlation values: red - positive, blue – negative and white – zero correlation. The black contours are at $\pm$ 0.05. (c) One-dimensional conductance histograms constructed from selected traces that have at least 80 data points in the Ag-SAC (grey, 3904 traces), AgO-S (red, 3345 traces) and AgO-P (green, 2501 traces) conductance ranges, respectively.

silver atoms[17-19], we can expect oxygen atoms to interact with the Ag point-contacts to form

Ag-O containing structures. Theoretically, Ag-single atom contacts with an O in series were

shown to have a conductance of ~0.4 G_0[13, 16]. Furthermore, it was shown experimentally that the 1 G_0 single atom contact feature in 1D conductance histograms was suppressed when traces showing 1.3 G_0 and 0.4 G_0 features were selectively analyzed[10]. These results highlight the need to better understand the structure and structural evolution basis for the observations. In what follows, we utilize the independently measured conductance and force data to determine the structural evolution pathway by first quantifying the correlations in the occurrence of different structures using conductance as their structural fingerprint and then analyzing the mechanical properties of each of these structures.

6.2   Correlations among conductance features

We first carry out a statistical correlation analysis for the measured conductance traces by constructing a two-dimensional cross-correlation histogram (Figure 6.2b), using a procedure detailed previously[22, 23] (see section 6.4). Briefly, the 2D cross-correlation histogram shows the correlation in either the occurrence or in the plateau lengths of different conductance features within individual traces. Positively (negatively) correlated regions indicate that two conductance values occur (do not occur) together in the same trace frequently[22]. In Figure 6.2b (right panel), we also plot a vertical profile of this 2D correlation plot taken at ~1 G_0 (corresponding to the dashed line at 0.9 G_0 on the cross-correlation histogram) where correlations between a 1 G_0 feature and those at other conductance values are elucidated. Along this line profile, the red, positively correlated region around 2.5 G_0 indicates that plateaus around 1 G_0 and 2.5 G_0 frequently occur together in the same trace. In contrast, the blue regions around 0.4 G_0 and 1.3 G_0, which we attributed to the presence of O in the junction, indicate that 1 G_0 plateaus are anti-correlated with plateaus at either of these values. Next, we consider a vertical section around 1.3 G_0 (corresponding to the dashed line at 1.3 G_0 on the cross-correlation histogram, Figure 6.2b).

Along this profile, the red regions around 0.4 G_0 indicate that the structures responsible for conductance plateaus at 1.3 G_0 and 0.4 G_0 are correlated.

A subtle, but important detail in the analysis of cross-correlation histograms is that the negative values in the cross-correlation histogram can stem from two reasons: a) anti-correlations in occurrence (occurrence of two conductance plateaus is mutually exclusive), or b) anti-correlations in plateau lengths (longer plateau length at one conductance value is accompanied by a shorter plateau length at the other conductance, and vice versa). To determine whether the anti-correlation between the 1 G_0 plateau and those at 1.3 G_0 and 0.4 G_0 is due to the an anti-correlation in their occurrence or anti-correlation in their plateau lengths, we construct conditional histograms[22, 23] from subsets of all measured traces, selecting for conductance features defined by the highlighted regions in Figure 6.2a. Specifically, we first select traces that have more than 80 data points (equivalent to a minimum plateau length of ~0.015 nm) within one of the three conductance ranges: 0.7 to 1.0 G_0 for Ag-SAC region, 0.25 to 0.55 G_0 for the AgO-S region and 1.1 to 1.4 G_0 for the AgO-P region. These conductance ranges and the plateau length cut-off are determined from a logarithmically binned conductance histogram as detailed in the Methods section. We then construct conditional 1D histograms (Figure 6.2c) of the selected traces, without any other selection criteria. We observe that by selecting for the Ag-SAC plateaus, both the AgO-S and AgO-P features are highly suppressed, whereas the 2.5 G_0 feature is retained. This indicates that clean Ag-SAC junctions occur when oxygen impurities are absent in the vicinity of the junction. This result is in agreement with the cross-correlation analysis in Figure 6.2a, and with data from Ag contacts measured in an oxygen-free high-vacuum environment[8]. Similarly, by selecting for AgO-S conductance there is a dramatic suppression of the Ag-SAC feature. This supports the finding from the cross-correlation analysis that AgO-S

and Ag-SAC junctions do not occur in the same trace. On the other hand, by selecting for the AgO-P conductance we note that the Ag-SAC feature is reduced, but not fully suppressed. This could imply that occasionally Ag-SACs occur after the AgO-P junction, with anti-correlated plateau length[22]. However, since the AgO-P and Ag-SAC conductance ranges are close, it is also possible that we when we select traces with AgO-P features, we inadvertently pick a trace with Ag-SAC plateau. This is because the tail of the 1 G_0 histogram peak extends above 1 G_0, as is most clearly visible for the Au data (Figure 6.2a).

These structural insights are summarized as a schematic illustration in Figure 6.3a, which
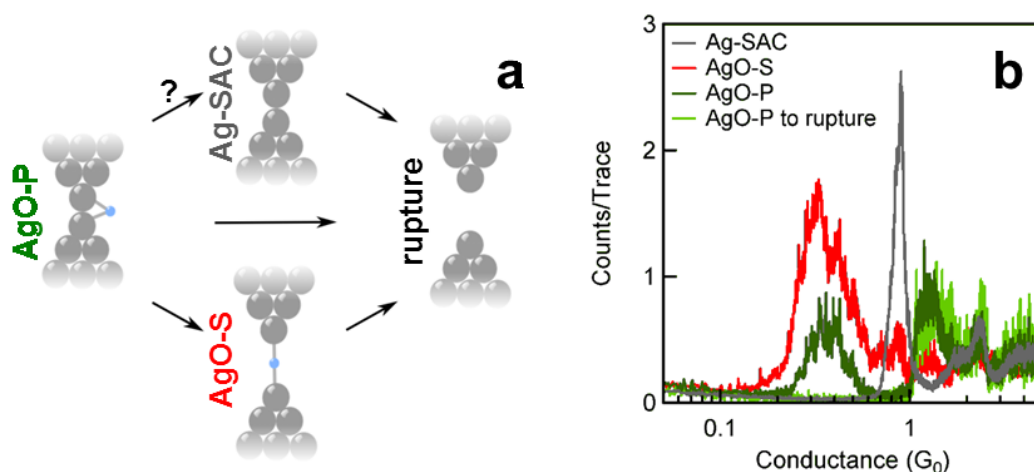
Figure 6.3. Junction evolution and conductance histograms of selected traces. (a) Schematic illustration of the three bonding motifs representing a clean Ag single atomic contact (Ag-SAC), Ag atomic contact with a series O bridge (AgO-S), Ag atomic contact with a parallel O bridge (AgO-P), and a ruptured junction. Arrows indicate the experimentally inferred structural evolution pathways. (b) One-dimensional conductance histograms constructed from selected AFM-BJ traces for Ag-SAC (grey, 955 traces), AgO-S (red, 355 traces), AgO-P (dark green, 214 traces), and AgO-P to rupture (light green, 90 traces).

shows the structural transition pathways for the Ag and Ag/O junctions. This scheme motivates the use of conductance features combined with simultaneous force measurements to quantify the mechanics of the various structural evolution scenarios of these atomic-scale junctions. Whereas AgO-S and Ag-SAC junctions rupture upon elongation, AgO-P junctions can rupture to an open

contact, or evolve into an AgO-S or, perhaps, into an Ag-SAC junction. In our analysis of forces, we treat these categories separately.

6.3   Mechanics of distinct structural motifs

We now analyze the data acquired using the AFM-BJ setup where we measure force simultaneously with conductance in 6,500 junctions. We first sort all measured traces to differentiate the structures based on the conductance features as detailed above. We further ensure that the Ag-SAC and AgO-S junctions rupture under elongation by selecting those traces where the conductance after rupture goes below 0.01 G_0 within 80 data points. For the AgO-P junctions, we only include traces which have less than 80 data points in the Ag-SAC conductance range (0.7 – 1.0 G_0) and fewer than 80 data points in the 0.01 – 0.25 G_0 conductance range as detailed above. With these requirements, we only include AgO-P junctions that evolve to AgO-S junctions or that rupture completely (Figure 6.3a). To characterize the subset of AgO-P junctions which rupture without evolving into an AgO-S structure, we select AgO-P junctions that have less than 80 data points in from 0.01 G_0 to 1.0 G_0 conductance range, thereby excluding Ag-SAC and AgO-S conductance features that could occur after the AgO-P conductance plateau. We note that not every conductance trace among the dataset (consisting of 6,500 simultaneous measurements of conductance and force) contains one of these structures of interest. Normalized conductance histograms from these selected subsets are shown in Figure 6.3b, which has the same peaks as those shown in Figure 6.2b, but very few counts in the low-conductance region, as traces that contribute to this region have been excluded in the selection. Peaks at 1 G_0, and 0.4 G_0 are seen in the Ag-SAC and AgO-S scenarios, analogous to those in Figure 6.2b. For the AgO-P junctions that rupture completely, a peak at 1.3 G_0 is observed. For the selection that includes

AgO-P junctions that evolve into an AgO-S junction, we see an additional conductance peak in the AgO-S range.

We can now analyze the simultaneously measured force data to determine rupture force and stiffness of individual junctions, for each of the four types of traces selected above (see section 6.4). We begin by locating the displacement range corresponding to the conductance plateau of interest (Figure 6.3b). We then obtain the rupture force by determining the force drop at the position where conductance plateau ends, *i.e.*, where the conductance drops abruptly below the plateau level (as illustrated in Figure 6.1b). We determine the stiffness of the junction by extracting the slope of the force ramp prior to the sharp drop (dotted line, Figure 6.1b). Since the force trace shows additional features during the course of a conductance plateau due to atomic-scale rearrangement, we use an automated algorithm[26] to isolate the final force event and use the slope of this segment to reliably obtain the stiffness of the junction (Chapter 2). This measured stiffness is the stiffness of the entire junction and also includes the stiffness of the cantilever. To determine the junction stiffness, we correct the measured value using a series spring model for the measured spring constant[33] of the AFM cantilever (~50 N/m) for each junction. Histograms of rupture force and stiffness are shown in Figure 6.4a,b along with Gaussian fits used to determine the mean rupture force and stiffness for each junction type. The results are from this analysis are summarized in Table 6.1.

We first observe that the measured rupture force for Ag-SACs (1 nN) is significantly smaller than that of an Au single-atom contact (1.5 nN)[25-27]. This is in excellent agreement with previous theoretical calculations that have consistently found a lower rupture force of ~1 nN for Ag-SACs compared to ~1.5 nN for Au[14, 34-37]. The stiffness of Ag-SACs of 8 N/m is the

same as that measured for Au[26, 27], perhaps reflecting their similar bulk Young's modulus of

Ag and Au (~80 GPa)[38].
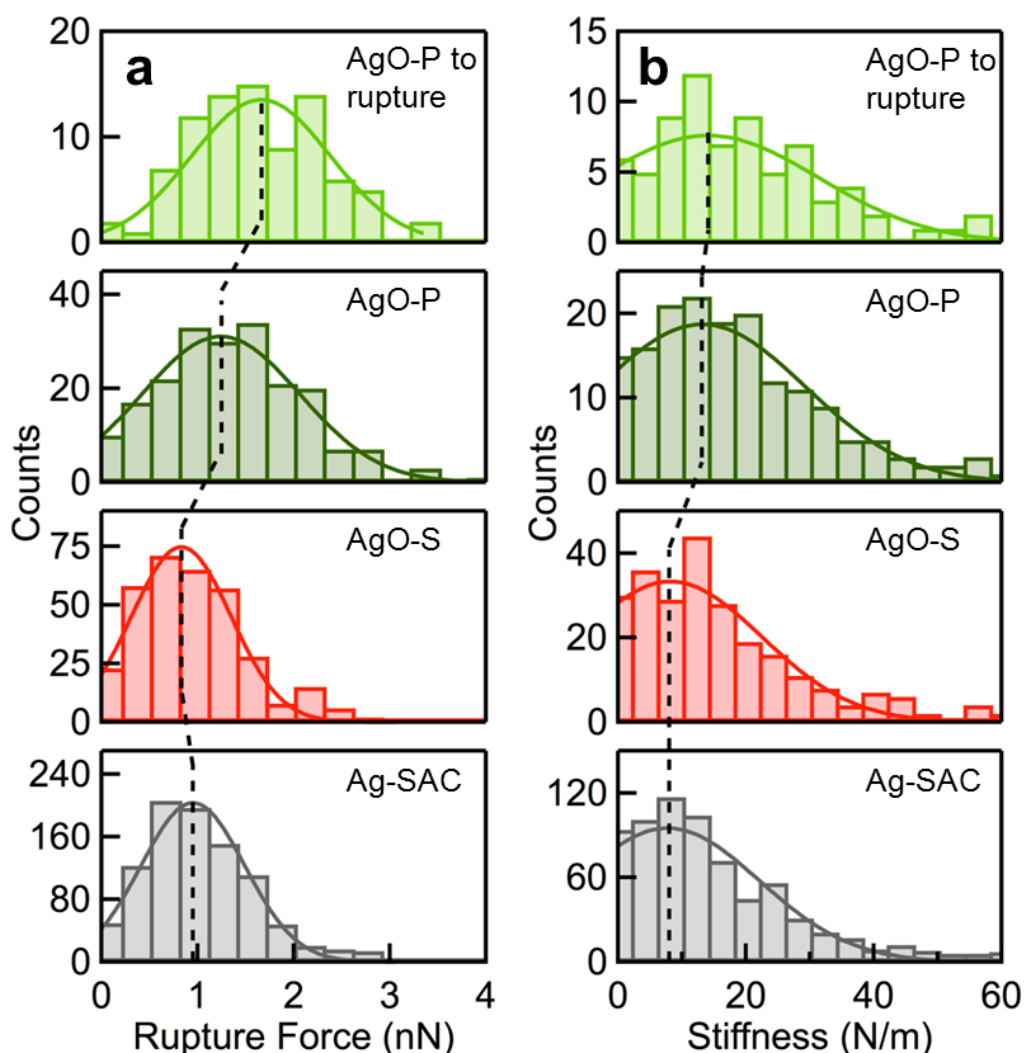
Figure 6.4. Rupture force and junction stiffness histograms. (a) Histograms of rupture force and (b) stiffness for Ag-SAC (grey), AgO-S (red), AgO-P (dark green) and AgO-P to rupture (light green). Gaussian fits are overlaid as solid curves and the dashed lines are provided as visual guides connecting the peak values.

The AuO-S junctions have slightly smaller rupture force (0.8 nN) than Ag-SAC junctions,

and stiffness (8 N/m) equal to the Ag-SAC junctions, within experimental error. Representing the

interatomic bonds as springs in a simplified model, in a AgO-S junction, the two Ag-O bonds are

in series with the Ag electrodes, and thus its stiffness and rupture force can only be smaller than or equal to that of an Ag-SAC (Figure 6.3a). Theoretical calculations indicate that the Ag-O bond strength might be comparable to the Ag-Ag bond in the Ag-SAC case[14, 34]. Experimentally, the observation of enhanced formation of monatomic Ag wires in low temperature break junction experiments (< 40 K) in the presence of oxygen also supports the idea that Ag-O bonds are comparable in strength to Ag-Ag bonds[11, 12]. Our experimental results thus present a quantitative measurement of the Ag-O bonding strength.

Table 6.1. Most frequently measured force and stiffness. Sample size for each case and standard errors in the fit are also shown.

Type	# of traces	Force (nN)	Stiffness (N/m)
Ag-SAC	955	0.95 ± 0.02	7.7 ± 0.5
AgO-S	344	0.83 ± 0.03	8.2 ± 0.8
AgO-P	215	1.24 ± 0.06	13.1 ± 1.2
AgO-P to rupture	90	1.66 ± 0.09	14.1 ± 2.1

For the AgO-P junctions that rupture completely, we obtain a rupture force (stiffness) of 1.7 nN (14 N/m) when the junction ruptures to an open contact. However, if the AgO-P junctions that evolve to AgO-S junctions are included, the rupture force and stiffness are found to be 1.2 nN and 13 N/m respectively. The rupture force for an AgO-P junction is thus much larger than for Ag-SAC and AgO-S. This strongly indicates that the oxygen atom is stabilizing the junction in AgO-P junctions. In an AgO-P configuration (Figure 6.3a) we expect the Ag-O bonds to be in parallel to the Ag-Ag bonds; such a junction will be stiffer than Ag-SAC and if it ruptures upon elongation, we expect a larger rupture force than that of an Ag-SAC. The stiffness and rupture

force results obtained here provide conclusive evidence that the 1.3 G_0 junctions are indeed those that have an O in a parallel configuration. The fact that the stiffness of AgO-S junctions is almost the same as Ag-SAC junctions further demonstrates that the Ag-O bonds are comparable to Ag-Ag bonds in terms of their mechanical properties. On the other hand, the parallel Ag-O bonds in AgO-P junctions can be intuitively thought of as providing additional stabilization, as well as a parallel spring in the junction. Finally, we note a subtlety in interpreting the meaning of the measured rupture force of AgO-P junctions. The lower rupture force in AgO-P junctions which evolve into AgO-S structure is due to the fact that the junction does not rupture to an open contact. This prevents the AFM cantilever from relaxing completely and therefore the measured drop in force is smaller than the full value that is observed in the AgO-P junctions that rupture to a conductance below the 0.01 G_0 cut-off. Therefore, in this context, the measured forces correspond to the difference between the maximum sustained force by AgO-P junctions and the initial force sustained by the succeeding AgO-S junction. However, the measured stiffness is approximately the same (within experimental error) for AgO-P junctions, whether considering only the subset of junctions that ruptures or including junctions that evolve into AgO-S structures as well, since the basic AgO-P structure is the same, irrespective of the evolution scenarios.

In conclusion, we have studied the electric and mechanical behavior of Ag junctions in ambient conditions. These measurements show conductance features of clean Ag-SACs as well as Ag contacts that include O impurities. Using a selection process based on the cross-correlations among the conductance of various junction structures, we are able to analyze different junction structures separately. The results from the force measurements allow us to rigorously quantify the mechanics of Ag-SAC, AgO-S and AgO-P structures, adding significantly to our understanding of the behavior of atomic-size junctions of Ag, and their contrast with Au.

We expect the experimental methods and results presented here to enable progress in the study of single molecule junctions with Ag electrodes.

6.4 Supporting information

Figure 6.5 shows the logarithmically binned one-dimensional conductance histogram of 10,000 Ag traces measured with the STM-BJ setup, which visualizes the same data represented in Figure 6.2a in the main text. In the logarithmically binned histogram the peaks in the conductance data, as well as their minima, appear more clearly. This allows us to define the conductance ranges for the Ag-SAC (0.7 G_0 – 1.0 G_0), AgO-S (0.25 G_0 – 0.55 G_0) and AgO-P (1.0 G_0 – 1.4 G_0), as highlighted by the shaded regions in Figure 6.5.
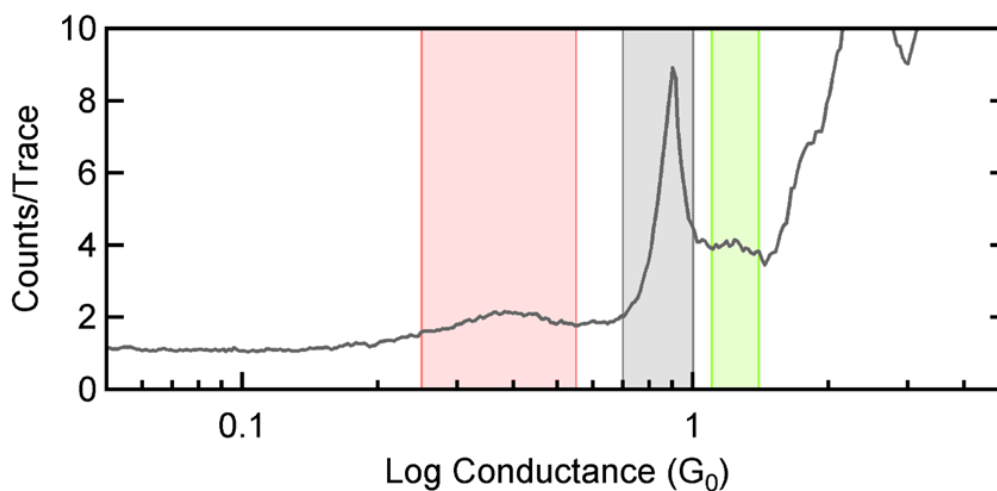
Figure 6.5. Logarithmically binned one-dimensional histogram. Histogram constructed from STM measurements of (10,000 traces, 167 bins per decade). Ag-SAC (grey), AgO-S (red) and AgO-P (green) conductance ranges are highlighted.

Figure 6.6 shows additional sample traces for each of the cases discussed in the main text. Figure 6.6a represents an Ag-SAC junction that ruptures after the 1 G_0 conductance plateau. Conductance features at 1.8 G_0 and 2.5 G_0 are also observed before the 1 G_0 plateau.
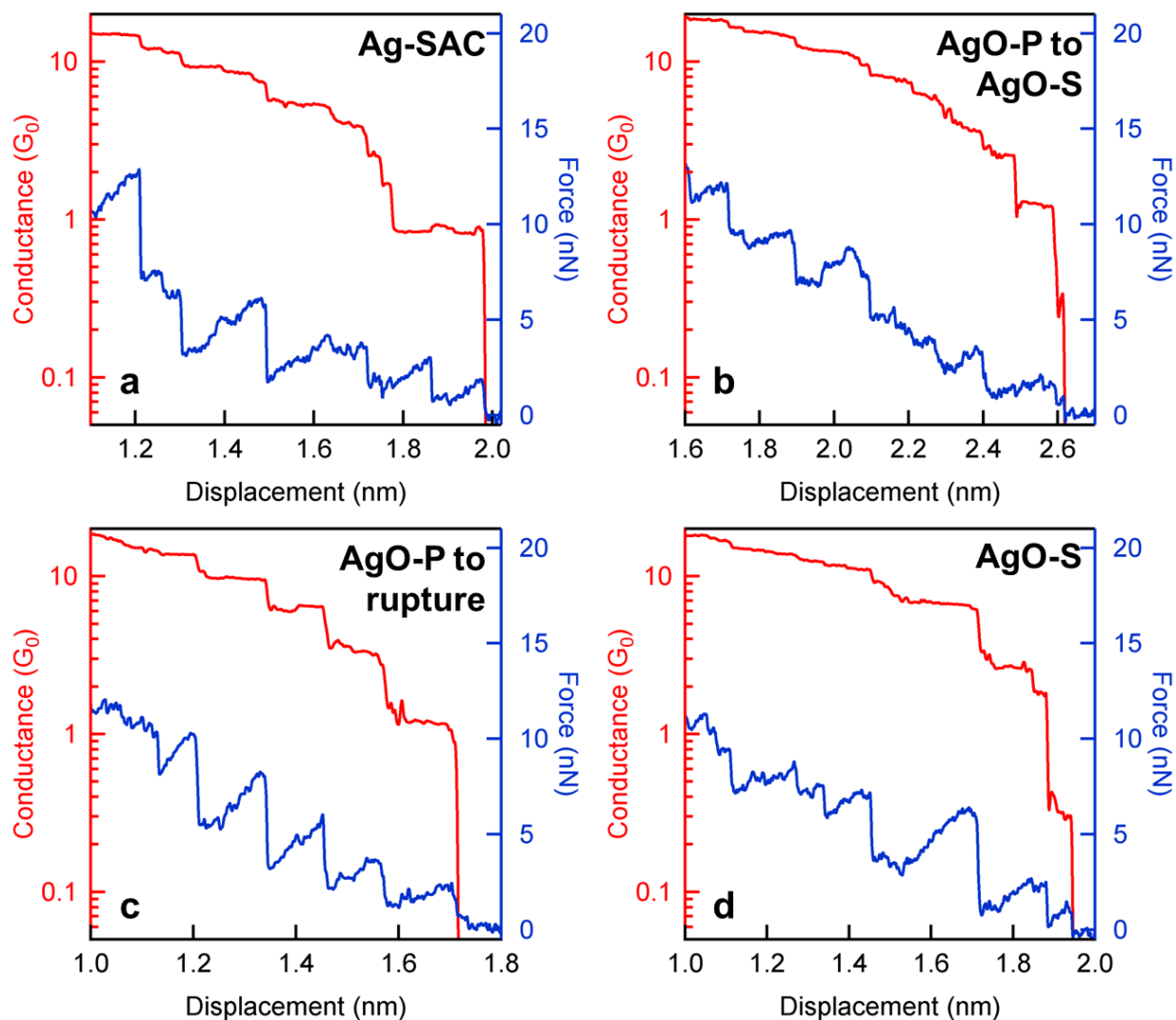
Figure 6.6. Additional sample traces. Sample traces showing the simultaneously measured conductance (red, left axis) and force (blue, right axis): Ag-SAC (a), AgO-P to AgO-S (b), AgO-P to rupture (c) and AgO-S (d).

Figure 6.6b,c represent AgO-P (with a plateau at ~1.3 G_0) junctions. In addition to the AgO-P conductance plateau, an additional feature at ~0.3 G_0 that can be ascribed to an evolution into AgO-S structure is also observed in Figure 6.6b (AgO-P to AgO-S scenario). However, in Figure 6.6c the AgO-P junction is completely ruptured upon elongation (AgO-P to rupture). Therefore, traces such as those in Figure 6.6b and Figure 6.6c are included in AgO-P, but only traces such as Figure 6.6c are included in AgO-P to rupture scenario. Finally, Figure 6.6d shows a representative AgO-S junction, with a plateau at ~0.3 G_0, where we also note the absence of any

conductance feature at 1 G_0 corresponding to the Ag-SAC, which reflects the anti-correlation between 1 G_0 and 0.4 G_0 features observed in the cross-correlation analysis presented in the main text (Figure 6.2b).

We follow the methods of Halbritter *et al.*[22, 23] to perform the conductance cross-correlation analysis. We create the 2D cross-correlation histogram shown in Figure 6.2b within the main text with bins of size 0.01 G_0 spanning 0 to 4 G_0. The value of each bin in the 2D conductance is:

$$C_{i,j} = \frac{\left\langle \delta N_i(r) * \delta N_j(r) \right\rangle_r}{\sqrt{\left\langle \left[\delta N_i(r)\right]^2 \right\rangle_r \left\langle \left[\delta N_j(r)\right]^2 \right\rangle_r}}$$
<div align="right">**Eq. 6-1**</div>

where the subscripts *i, j* identify the bin in the horizontal and vertical axes, while *r* is an index representing each trace included in the calculation. The $\left\langle ... \right\rangle$ represent an average over all traces *r* and $\delta N \equiv N_i(r) - \left\langle N_i(r) \right\rangle_r$.

6.5 References

1.   N. Agraït, A.L. Yeyati, and J.M. van Ruitenbeek, *Quantum properties of atomic-sized conductors.* Physics Reports, 2003. **377**(2-3): p. 81-279.

2.   J.M. Krans, C.J. Muller, I.K. Yanson, T.C.M. Govaert, R. Hesper, and J.M. van Ruitenbeek, *One-Atom Point Contacts.* Physical Review B, 1993. **48**(19): p. 14721-14724.

3. J.M. Krans, J.M. van Ruitenbeek, V.V. Fisun, I.K. Yanson, and L.J. Dejongh, *The Signature of Conductance Quantization in Metallic Point Contacts.* Nature, 1995. **375**(6534): p. 767-769.

4. E. Scheer, N. Agrait, J.C. Cuevas, A.L. Yeyati, B. Ludoph, A. Martin-Rodero, G.R. Bollinger, J.M. van Ruitenbeek, and C. Urbina, *The signature of chemical valence in the electrical conduction through a single-atom contact.* Nature, 1998. **394**(6689): p. 154-157.

5. H. Oshima and K. Miyano, *Spin-dependent conductance quantization in nickel point contacts.* Applied Physics Letters, 1998. **73**(15): p. 2203-2205.

6. B. Ludoph, N. van der Post, E.N. Bratus', E.V. Bezuglyi, V.S. Shumeiko, G. Wendin, and J.M. van Ruitenbeek, *Multiple Andreev reflection in single-atom niobium junctions.* Physical Review B, 2000. **61**(12): p. 8561-8569.

7. J.L. Costa-Kramer, *Conductance quantization at room temperature in magnetic and nonmagnetic metallic nanowires.* Physical Review B, 1997. **55**(8): p. R4875-R4878.

8. V. Rodrigues, J. Bettini, A.R. Rocha, L.G.C. Rego, and D. Ugarte, *Quantum conductance in silver nanowires: Correlation between atomic structure and transport properties.* Physical Review B, 2002. **65**(15): p. 153402.

9. H. Masuda and T. Kizuka, *Structure, Electrical, and Mechanical Properties of Silver Nanocontacts.* Japanese Journal of Applied Physics, 2010. **49**(4): p. 045202.

10. D. den Boer, O.I. Shklyarevskii, M.J.J. Coenen, M. van der Maas, T.P.J. Peters, J.A.A.W. Elemans, and S. Speller, *Mechano-Catalysis: Cyclohexane Oxidation in a Silver Nanowire Break Junction.* Journal of Physical Chemistry C, 2011. **115**(16): p. 8295-8299.

11. W.H.A. Thijssen, D. Marjenburgh, R.H. Bremmer, and J.M. van Ruitenbeek, *Oxygen-enhanced atomic chain formation.* Physical Review Letters, 2006. **96**(2): p. 026806.

12. W.H.A. Thijssen, M. Strange, J.M.J.A. de Brugh, and J.M. van Ruitenbeek, *Formation and properties of metal-oxygen atomic chains.* New Journal of Physics, 2008. **10**: p. 033005.

13. H. Ishida, *Embedded Green-function calculation of the conductance of oxygen-incorporated Au and Ag monatomic wires.* Physical Review B, 2007. **75**(20): p. 205419.

14. S. Di Napoli, A. Thiess, S. Blugel, and Y. Mokrousov, *Modeling impurity-assisted chain creation in noble-metal break junctions.* Journal of Physics-Condensed Matter, 2012. **24**(13): p. 135501.

15. A. Thiess, Y. Mokrousov, S. Blugel, and S. Heinze, *Theory and application of chain formation in break junctions.* Nano Letters, 2008. **8**(8): p. 2144-2149.

16.   M. Strange, K.S. Thygesen, J.P. Sethna, and K.W. Jacobsen, *Anomalous conductance oscillations and half-metallicity in atomic Ag-O chains.* Physical Review Letters, 2008. **101**(9): p. 096804.

17.   N. Bonini, A. Kokalj, A. Dal Corso, S. de Gironcoli, and S. Baroni, *Structure and dynamics of oxygen adsorbed on Ag(100) vicinal surfaces.* Physical Review B, 2004. **69**(19): p. 195401.

18.   L. Vattuone, U. Burghaus, L. Savio, M. Rocca, G. Costantini, F.B. de Mongeot, C. Boragno, S. Rusponi, and U. Valbusa, *Oxygen interaction with disordered and nanostructured Ag(001) surfaces.* Journal of Chemical Physics, 2001. **115**(7): p. 3346-3355.

19.   M. Schmidt, P. Cahuzac, C. Brechignac, and H.P. Cheng, *The stability of free and oxidized silver clusters.* Journal of Chemical Physics, 2003. **118**(24): p. 10956-10962.

20.   P. Jelinek, R. Perez, J. Ortega, and F. Flores, *Ab initio study of evolution of mechanical and transport properties of clean and contaminated Au nanowires along the deformation path.* Physical Review B, 2008. **77**(11): p. 115447.

21.   Z.L. Cheng, R. Skouta, H. Vázquez, J.R. Widawsky, S. Schneebeli, W. Chen, M.S. Hybertsen, R. Breslow, and L. Venkataraman, *In situ formation of highly conducting covalent Au-C contacts for single-molecule junctions.* Nature Nanotechnology, 2011. **6**(6): p. 353-357.

22.   P. Makk, D. Tomaszewski, J. Martinek, Z. Balogh, S. Csonka, M. Wawrzyniak, M. Frei, L. Venkataraman, and A. Halbritter, *Correlation analysis of atomic and single-molecule junction conductance.* ACS Nano, 2012. **6**(4): p. 3411-3423.

23.   A. Halbritter, P. Makk, S. Mackowiak, S. Csonka, M. Wawrzyniak, and J. Martinek, *Regular Atomic Narrowing of Ni, Fe, and V Nanowires Resolved by Two-Dimensional Correlation Analysis.* Physical Review Letters, 2010. **105**(26): p. 266805.

24.   L. Venkataraman, J.E. Klare, I.W. Tam, C. Nuckolls, M.S. Hybertsen, and M.L. Steigerwald, *Single-molecule circuits with well-defined molecular conductance.* Nano Letters, 2006. **6**(3): p. 458-462.

25.   M. Frei, S.V. Aradhya, M. Koentopp, M.S. Hybertsen, and L. Venkataraman, *Mechanics and chemistry: single molecule bond rupture forces correlate with molecular backbone structure.* Nano Letters, 2011. **11**(4): p. 1518-1523.

26.   S.V. Aradhya, M. Frei, M.S. Hybertsen, and L. Venkataraman, *Van der Waals interactions at metal/organic interfaces at the single-molecule level.* Nature Materials, 2012. **11**(10): p. 872-876.

27.   G. Rubio-Bollinger, S. Bahn, N. Agraït, K. Jacobsen, and S. Vieira, *Mechanical Properties and Formation Mechanisms of a Wire of Single Gold Atoms.* Physical Review Letters, 2001. **87**(2): p. 026101.

28. R.H.M. Smit, C. Untiedt, A.I. Yanson, and J.M. van Ruitenbeek, *Common origin for surface reconstruction and the formation of chains of metal atoms.* Physical Review Letters, 2001. **87**(26): p. 266102.

29. B. Ludoph and J.M. van Ruitenbeek, *Conductance fluctuations as a tool for investigating the quantum modes in atomic-size metallic contacts.* Physical Review B, 2000. **61**(3): p. 2273-2285.

30. S. Kaneko, T. Nakazumi, and M. Kiguchi, *Fabrication of a Well-Defined Single Benzene Molecule Junction Using Ag Electrodes.* Journal of Physical Chemistry Letters, 2010. **1**(24): p. 3520-3523.

31. K. Hansen, E. Laegsgaard, I. Stensgaard, and F. Besenbacher, *Quantized conductance in relays.* Physical Review B, 1997. **56**(4): p. 2208-2220.

32. A.I. Yanson, G.R. Bollinger, H.E. van den Brom, N. Agrait, and J.M. van Ruitenbeek, *Formation and manipulation of a metallic wire of single gold atoms.* Nature, 1998. **395**(6704): p. 783-785.

33. J.L. Hutter and J. Bechhoefer, *Calibration of Atomic-Force Microscope Tips.* Review of Scientific Instruments, 1993. **64**(7): p. 1868-1873.

34. D. Cakir and O. Gulseren, *Effect of impurities on the mechanical and electronic properties of Au, Ag, and Cu monatomic chain nanowires.* Physical Review B, 2011. **84**(8): p. 085450.

35. S.R. Bahn and K.W. Jacobsen, *Chain Formation of Metal Atoms.* Physical Review Letters, 2001. **87**(26): p. 266101.

36. F.J. Ribeiro and M.L. Cohen, *Ab initio pseudopotential calculations of infinite monatomic chains of Au, Al, Ag, Pd, Rh, and Ru.* Physical Review B, 2003. **68**(3): p. 035423.

37. E.Y. Zarechnaya, N.V. Skorodumova, S.I. Simak, B. Johansson, and E.I. Isaev, *Theoretical study of linear monoatomic nanowires, dimer and bulk of Cu, Ag, Au, Ni, Pd and Pt.* Computational Materials Science, 2008. **43**(3): p. 522-530.

38. F. Cardarelli, *Materials handbook a concise desktop reference*, 2008, Springer: London.

7

Experimentally quantifying the binding energetics

of atomic-size junctions

The strength and characteristic length dependence of binding interactions at atomic scale is of fundamental importance to many areas of science. However, even with the tremendous advances in scanning probe microscopy, *ab-initio* calculations are typically relied upon to provide the quantitative insights about these energetics aspects. Here we present a general method to reconstruct binding energy curves of single atomic contacts and single-molecule junctions directly from experimental measurements, using a simplified model for their mechanics. We compare the results to density functional theory calculations and find striking agreement for each of the cases considered. Combined with the demonstrated feasibility of single-molecule experiment, this technique provides an approach to significantly expand the versatility of atomic force microscopy towards quantifying binding energetics at the atomic scale – without requiring vacuum conditions or low temperatures.

Density functional theory calculations in this chapter were performed by Dr. Mark Hybertsen.

Atomic-scale metallic and metal-molecule interfaces impact electrical, optical, mechanical and thermal properties of materials, and can dominate the behavior of nanoscale structures. Scanning probe microscopy techniques have enabled experimental probing of such interfaces in single-molecule junctions, focusing on the measurement of their electronic transport[1-3] and mechanics[4-6]. In particular, simultaneous measurements of conductance and force in single-atomic contacts and single-molecule junctions[7-11] provide intricate details of the relationship between structure, mechanics and transport. Most frequently, the experiments use an atomic force microscope (AFM) cantilever tip to either measure forces directly, or calculate forces from shifts in the resonance characteristics of the AFM cantilever. However, converting this information into the underlying potential energy profile is non-trivial. Frequently, theoretical simulations are invoked to provide the quantitative insights about the energetics, through which the experimental force data is then interpreted *a posteriori*[6-10]. On the other hand, several new theoretical developments are underway to capture effects like dispersive interactions that are crucial to such diverse structures as metal-organic interfaces, biological soft-matter and layered material like graphene[12-14]. However, for comparison to experiments these studies have had to rely on techniques like temperature programmed desorption which are only able to provide an estimate for the surface-averaged adsorption energy from ensembles of molecules. Therefore, there is a great need for general quantitative methods to directly obtain the potential energy profile from experimental data in single-molecule junctions, thereby enabling not only one-on-one comparison between theory and experiment, but also the benchmarking of new theoretical methods that are under development.

Here we present a technique that uses simultaneously measured force and conductance of atomic-size junctions to quantitatively characterize the binding energetics of atomic-size

junctions. We first introduce an intuitive and general parameterized form for the potential energy profiles of atomic-size junctions, characterizing their mechanics as a function of junction elongation. We use this parameterized form to obtain both binding energies and length scales for Au and Ag single atomic contacts and Au-molecule-Au single-molecule junctions of amine- and methylthio- terminated alkanes as well as pyridyl- terminated aromatic molecules. Additionally, we are able to experimentally characterize the significant contribution of van der Waals interactions at the Au-molecule interface, which remain especially difficult to accurately capture in *ab-initio* calculations. In each case, we find excellent agreement with density functional theory simulations of junction elongation. Finally, we obtain details of symmetric and asymmetric bond stretching through the mechanical evolution of these structures under elongation, which had so far remained concealed in experimental distributions. In general, this technique can enable the quantitative exploration of diverse interfaces of fundamental importance to many disciplines at the single-atomic and molecular scale.

7.1 Analytical model

As an illustrative example of the mechanics of single-molecule junctions, Figure 7.1 shows density functional theory (DFT) calculations simulating a single-molecule junction elongation, where the molecule is 1,4-bis(methylthio)butane, abbreviated **C4SMe**[15]. The elongation of the junction is performed as an adiabatic trajectory simulation by moving the Au electrodes apart in increments of 0.1 Å and minimizing the total energy at each step. The curve in Figure 7.1a (black circles) shows the total potential energy (U) as a function of the junction elongation (x). At large elongations, the energy profile exhibits an asymptotic approach toward the ruptured structure (in this case, a structure with the top Au-S donor acceptor bonds broken, with the bottom bond retained). The minimum of this curve represents a completely relaxed structure, and the

difference between this minimum value and the asymptotic value is defined as the binding energy (E_{bind}) of the junction. In addition, a length scale (L_{bind}) can be defined as the distance along the junction elongation axis between the energy minimum and the inflection point of the potential energy profile. The inflection point can be more readily identified in the corresponding force (F) profile shown in Figure 7.1b (black squares). We note that for clarity, we use a convention that the tensile force is positive, such that $F=dU/dx$, therefore the inflection point corresponds to the maximum force (F_{max}). Figure 7.1c shows the bond length of the top (red) and bottom (green) Au-S bonds, showing a dramatic increase in the top bond to the Au tip structure, while the bottom bond is minimally stretched. Snapshots of the junction structure at minimum energy, maximum force and rupture are also shown.
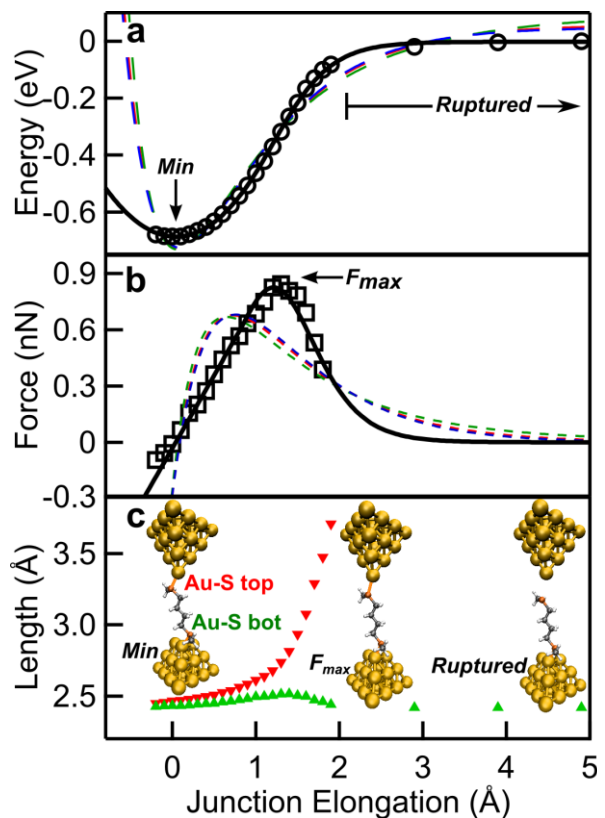
Figure 7.1. DFT calculations and model fits to C4SMe single-molecule junction. (a) DFT calculated energies (open circles) as a functon of elongation, along with hybrid model fit (solid black line). (b) Numerical derivative of the fitted hybrid curve (solid line) quantitatively reproduces the features of the force from calculations (open squares). Fits to the DFT energies, and their respective derivatives for Morse (dashed red), Lennard-Jones (dashed green) and universal binding curve (dashed blue) potentials are also shown for comparison in b and c. (c) Bond lengths for the top (red downward triangles) and bottom (green upward triangles) S-Au bonds from DFT, along with Energy minimized structures corresponding to minimum energy, maximum force and rupture.

Previous studies have attempted to model such potential energy curves using Morse $\left(U(x) \sim a\left(1-\exp^{-bx}\right)^2\right)$, Lennard-Jones $\left(U(x) \sim a\left[(b/x)^{12} - (b/x)^6\right]\right)$ or the so called universal

binding curve model potential $\left(U(x) \sim -a\,(1+bx)(e^{-bx})\right)$ [16-18]; each of these model potentials is

by two parameters a,b that characterizes the scales for energy and length. We show the least-squares fits to each of these model potentials to the potential energy profile, as well as their derivatives in Figure 7.1a,b (dashed red, green and blue, respectively). It is clearly seen that although these model potentials capture the general shape, they fail to quantitatively characterize the potential energy or the force profile calculated by the DFT calculations. This failure is not entirely surprising because the Morse and Lennard-Jones model potentials were created with an intent to model pairwise interactions[19, 20] and the universal binding curve was intended for bulk crystalline metallic interactions[21]. However, the mechanics of single atomic contacts and single-molecule junctions involves many-body interactions of the molecule and the several atoms on the electrodes in the immediate neighborhood of the junction.

To capture the essential mechanics of single atomic contacts and single-molecule junctions in an intuitive and analytically tractable fashion, we propose a new 2-parameter hybrid model potential (Figure 7.2a) that combines a harmonic segment $\left(U(x) = \dfrac{1}{2}K_{harm}\,x^2 + U_0\right)$ near the energy minima and a logistic segment $\left(U(x) = \dfrac{D}{1+e^{-x/r}}\right)$ towards the asymptotic region. Here, K_{harm} is a characteristic spring constant of the elastic junction elongation, U_0 is a constant with dimensions of energy and D, r
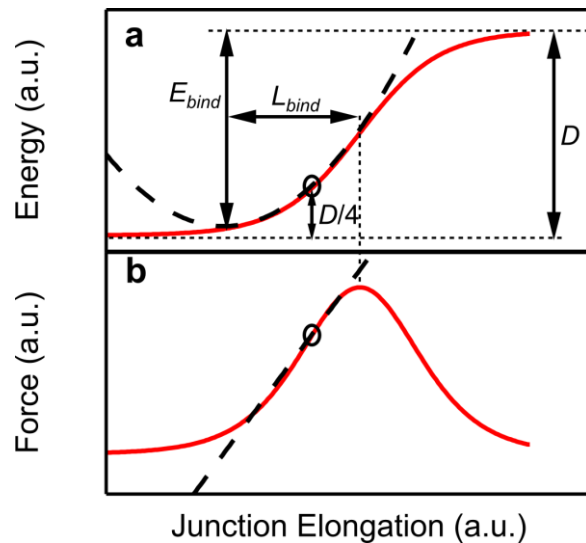
Figure 7.2. Hybrid model construction. (a) Separate harmonic (dashed black) and logistic (red) segments, showing key energy and length scale parameters. (b) The separate force profiles illustrate the linear elastic regime (dashed black) and rupture regime (red). The connection point is shown as a circle in both a and b.

are the characteristic energy and length parameters, respectively, for the logistic function that models the bond rupture regime. Boundary conditions are applied such that the model potential is continuous and differentiable at the connection point in the elastic regime. Here we have chosen this connection point to be at $D/4$ above the logistic tail (circles in Figure 7.2a,b); however any connection point before F_{max} can be used without any significant changes. Simple relations connecting the binding energy and length scale to the maximum force and spring constant are immediately obtained by consistently solving the resulting set of implicit equations self-consistently:

$$E_{bind} = 7.79\, F_{max}^2 / K_{harm} = 0.97\, D \qquad\qquad \textbf{Eq. 7-1}$$

$$L_{bind} = 10.66\, F_{max} / K_{harm} = 3.43\, r \qquad\qquad \textbf{Eq. 7-2}$$

where, for convenience, the units used for E_{bind} is eV, L_{bind} is Å, F_{max} is nN and K_{harm} is N/m. Phenomenologically, the harmonic section describes the mechanics near the minimum energy (mirrored by the linear increase in the force up to the maximum force in Figure 7.2a) with an effective spring constant for the junction (K_{harm}), while the logistic segment models the distinctly different mechanics of the bond rupture (as seen in the rapid non-linear drop beyond the maximum force in Figure 7.2a).

Figure 7.1a (solid line) presents the least squares fit of this hybrid model to the DFT calculated potential energy profile of **C4SMe**. First, the very good fit to the calculated energy (*r.m.s.* error between the DFT datapoints and the fit is 0.005 eV in this case) demonstrates the ability of the hybrid model, despite its simple construction using just two parameters corresponding to energy and length scales, to quantitatively capture all the essential features of the calculated potential energy profile. Secondly, Figure 7.1b (solid line) demonstrates the extremely good agreement between the derivative of the hybrid model fit and the DFT calculated

force profile. Finally, this hybrid model potential is similarly successful in describing all the atomic-size junctions we have considered in this study, beyond the illustrative example in Figure 7.1a-c (see supporting information). The combination of these three factors makes the hybrid model an ideal candidate to base the reconstruction of potential energy profiles from single-molecule force measurements. An added advantage of the hybrid model is that the stiffness in the elastic regime is constant, whereas it varies drastically at all locations in the Morse, Lennard-Jones and universal binding energy model potentials (dashed red, green and blue in Figure 7.1b, respectively).

7.2 Experimental and analysis methods

Figure 7.3a presents a schematic of the experimental setup used to study the mechanics of various junctions in this study [9]. Here, the single atomic contacts and single-molecule junctions are formed between an Au coated mica substrate and the tip of an Au-coated AFM cantilever which represent the two metallic electrodes. Using the break-junction procedure, we repeatedly approach the tip and substrate until an Au atomic point contact of more than 5 G_0 ($G_0 = 2e^2/h$, the quantum of conductance) is formed, and then retract them at a constant speed of 18 nm/s to elongate the junction. During the retraction, we simultaneously measure the force and conductance across the junction. As the two Au electrodes are pulled apart, the junction conductance decreases in steps of integer multiples of G_0, representing the thinning of the Au point contact (Figure 7.3b,c). These steps in conductance are accompanied by saw-tooth features in force, which correspond to loading and rupture of the sequence of structures during elongation. Au single atomic contacts, characterized by a conductance of 1 G_0, are frequently observed before the tip and substrate entirely lose contact.
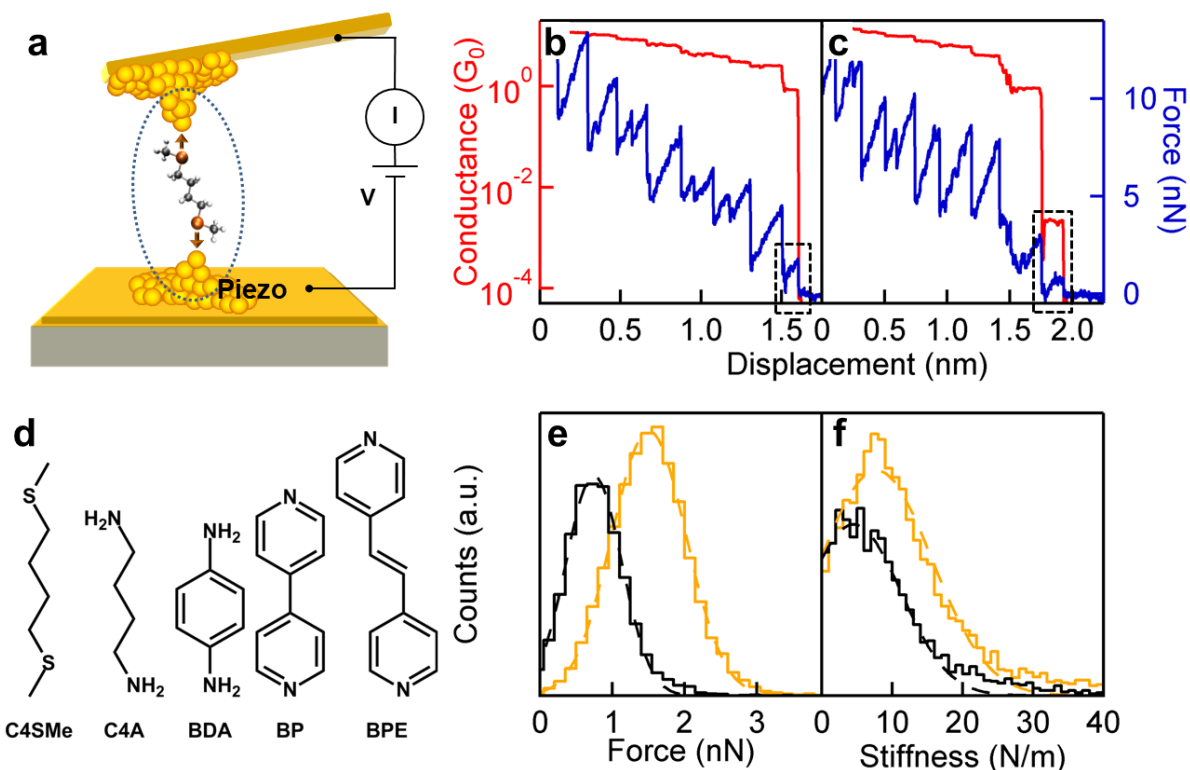
Figure 7.3. Experimental setup and sample simultaneously measured conductance and force data. (a) Schematic of the experimental setup highlighting the relevant junction region. Typical simultaneously measured conductance (red, left axis) and force (blue, right axis) traces for an individual realization of Au single atomic contact (b) and single-molecule junction of **C4SMe** (c). (d) Chemical structures of the molecules with different linker groups used in this study. Histograms of rupture forces (e) and stiffness (f) for Au single atomic contacts (yellow) and **C4SMe** (black). Gaussian fits are overlaid as dashed lines. The peak loations in the fits correspond to $<F_{exp}>$ and $<K_{exp}>$, as defined in the text, respectively.

To study single-molecule junctions, a low concentration of molecules is deposited on the substrate either by thermally evaporating the target molecule or depositing a drop of a dilute solution (<1 mMol) onto the substrate[9, 15, 22]. In this study we present measurements of Au and Ag single atomic contacts as well as five different molecules (Figure 7.3d) which selectively bind to the Au electrodes to form Au-molecule-Au single-molecule junctions. **C4SMe** and **C4A** (1,4-butanediamine) are saturated four carbon chains with methylthio (SMe) and amine (NH_2) terminations, whereas **BDA** (1,4-benzenediamine) is a NH_2-terminated aromatic molecule. **BP** (4,4'-bipyridine) and **BPE** (1,2-bis(4-pyridyl)ethylene)) are heteroaromatic molecules that bind to gold through the pyridyl group. In the presence of these molecules, an additional conductance

plateau at a characteristic value (less than 1 G_0) is frequently observed immediately after the Au single atomic contact ruptures during junction elongation, signifying the formation of a single-molecule junction (Figure 7.3c). Junctions of **BP** and **BPE** are also interesting because their single-molecule junctions exhibit two distinct high (**BP$_H$** or **BPE$_H$**) and low (**BP$_L$** or **BPE$_L$**) conductance features. We have recently demonstrated that these features correspond to two distinct structures: while low conductance structures are analogous to **C4A** in their donor-acceptor N-Au binding, the high conductance structures arise from significant van der Waals interactions between the molecule and the Au electrodes in addition to the donor-acceptor interactions[10]. In this study we separately analyze the mechanics of the high and low conducting features highlighting the significant contribution of van der Waals interactions to the binding energy, and thereby providing a reconstructed potential energy profile that will prove useful in benchmarking future DFT calculations that include dispersive interactions.

We use the conductance features as fingerprints to identify Au and Ag single atomic contacts and Au-molecule-Au single-molecule junctions, and subsequently analyze the force data from each such experimental trace of the relevant junction (boxed regions in Figure 7.3b,c). Specifically, we obtain the maximum force sustained by the junction (drop in force at the location of junction rupture) and the junction stiffness (slope of the force trace during the elongation). The distribution of rupture forces and stiffness (Figure 7.3e,f) is Gaussian with a well-defined peak representing the most frequently measured rupture force ($<F_{exp}>$) and stiffness ($<K_{exp}>$), that are tabulated for each case in this study in Table 7.1. While previous studies have reported on the broad agreement between DFT derived and experimentally measured forces in several metallic single atomic contacts and single-molecule junctions[6-10], physically motivated arguments about the hybrid model potential enable us to extract the potential energy

profile directly from the experimentally measured mechanics. Firstly, we note that the energy scales of single atomic contacts and single-molecule junctions (~ 1 eV) are much larger than the thermal energy scale at room temperature (k_B × 298 K ≈ 0.025 eV). Secondly, the junction is coupled to a stiff (50 N/m), bulk electrode represented by the cantilever on one side, along with an essentially infinitely stiff bulk electrode represented by the substrate on the other. In our experiment, we estimate the thermal fluctuations of the AFM cantilever to be ~ 10 pm (from spectral measurements of cantilever displacement) and the in-contact vibration spectrum of the cantilever yields an estimated mechanical noise of ~ 10 pm in our experimental setup, both much smaller than the length scale of the potential energy profiles of junctions considered in this study (~ 100 pm). The coupling of the single atomic contacts and single-molecule junctions to these bulk electrodes severely restrict the junction from exploring the potential landscape in directions other than that set by the elongation, further minimizing the probability of spontaneous junction rupture. Finally, only the few atoms in the immediate neighborhood of the junction contribute significantly to the mechanics of the single atomic contacts and single-molecule junctions. Therefore, the adiabatic trajectories simulated by DFT (with sufficient number of atoms in the vicinity of the junction allowed to relax, such as in Figure 7.1) can be expected to reasonably capture the mechanical properties of the experiment.

7.3   Results and discussion

To obtain the binding energy from the experimental data, we first substitute $<F_{exp}>$ → F_{max}, and $<K_{exp}>$ → K_{harm}, into Eq. 7-1. These substitutions are motivated by the above arguments, implying that, on average, the junctions rupture close to the adiabatic maximum force[23, 24]. As an illustration, for Au single atomic contacts we obtain a rupture force of 1.5 nN and stiffness of 7.7 N/m based on 8100 individual realizations, in excellent agreement with

previous reports[7]. Using Eq. 6-1, we obtain a binding energy of 2.28 ± 0.06 eV from the experimental data, in remarkable agreement with DFT calculated values for Au linear chains of ~2.2 eV[24, 25] as well as the bond dissociation energy of 2.29 eV for the Au-Au bond[26]. For Ag single atomic contacts, we obtain a lower binding energy (0.91 ± 0.10 eV), in qualitative agreement with the lower binding energy predicted in theoretical results ~1.5 eV[24]. Quantitative agreement might be lacking for Ag either owing to complex atomic-scale structures in the case of Ag single atomic contacts or due to the contamination of the Ag electrodes by O impurities in our room temperature, ambient measurements[27].

Table 7.1. Mean values of experimentally measured mean rupture force and stiffness; binding energies (E_{bind}) and length scales (L_{bind}) obtained from experiments and comparison to DFT. Errors in the experimental E_{bind} and L_{bind} are computed from standard errors of F_{exp} and K_{exp} experimental distributions.

Junction	Experimental data			Binding Energy (E_{bind})		Length Scale (L_{bind})	
	n	$<F_{exp}>$ (N)	$<K_{exp}>$ (N/m)	DFT [a] (eV)	Expt. (eV)	DFT [a] (Å)	Expt. (Å)
Au-Au	8100	1.50±0.01	7.7±0.1	~2.2	**2.28±.06**	-	**2.08±.04**
Ag-Ag	955	0.95±0.02	7.7±0.5	~1.5	**0.91±.10**	-	**1.32±.11**
Au-**C4SMe**	5132	0.77±0.01	5.3±0.1	0.68	**0.87±.04**	1.3	**1.55±.05**
Au-**C4A**	1100	0.62±0.01	3.9±0.3	0.65	**0.77±.08**	1.2	**1.69±.16**
Au-**BDA**	604	0.45±0.02	2.6±0.4	0.37	**0.61±.15**	1.1	**1.85±.37**
Au-**BP$_L$**	7763	0.88±0.01	7.0±0.1	0.81	**0.86±.03**	1.2	**1.34±.03**
Au-**BP$_H$**	4118	1.43±0.01	10.3±0.2	1.34[b]	**1.55±.05**	1.1[b]	**1.48±.04**
Au-**BPE$_L$**	496	0.83±0.02	7.9±0.3	-	**0.68±.06**	-	**1.12±.07**
Au-**BPE$_H$**	529	1.88±0.03	14.5±0.3	-	**1.90±.10**	-	**1.38±.05**

a – DFT values are from Refs [9, 10, 15]
b – For calculations involving BPH junctions, a molecule bound to a single electrode was used because of computational constraints introduced by a non-trivial electrode structure. In all other cases in this table, the calculations were performed with junction structures consisting of two electrodes.

In contrast to the calculations of single atomic contacts, we have previously published DFT results for single-molecule junctions formed by various molecules using DFT calculations with PBE using the projector augmented wave approach and the generalized gradient approximation (GGA) of Perdew, Burke, and Ernzerhof (PBE) for the exchange-correlation density functional [9, 15]. Table 7.1 summarizes the binding energies for all the junctions measured in this study and compares it with calculated values. We observe that the extracted binding energies for the single-molecule junctions are in excellent agreement in each case with our previously published DFT calculations. Indeed, the experimental values highlight the slight underestimation of DFT binding energies (~0.15 eV on average for **C4SMe**, **C4A**, **BDA** and **BP$_L$** single-molecule junctions which bind through donor-acceptor interactions) using the GGA functional[28]. Importantly, this method yields binding energies for both the high and low conducting junctions of molecules **BP** and **BPE**, showing that the high conducting junctions possessing significantly larger binding energy. For the high conducting **BP** junctions, our experimental result is in quantitative agreement with DFT calculations that included van der Waals interactions based on the DFT-D2 approach[29] in addition to the binding energy from the conventional GGA/PBE functional[10]. Finally, using Eq. 7-2 we can also extract the length scale of the binding energy curve that is important in characterizing the full mechanics at the atomic-scale. The L_{bind} values for each type of junction measured in this study is tabulated in Table 7.1.

In summary, we have presented a new model potential that quantitatively captures the many-body mechanics of atomic-size junctions. We utilize this model to reconstruct potential energy profiles of several single atomic contacts and single-molecule junctions from experimental force measurement data. We obtain remarkable agreement with DFT calculations, highlighting the efficacy of this technique. This technique can become a powerful general

method to extract energetic information from single-molecule measurements carried out under various environmental conditions. In the future, this technique can also be extended to obtain detailed mechanical details for individual measurements, giving powerful new insight into the energetics of atomic-scale junctions.

7.4 Supporting information
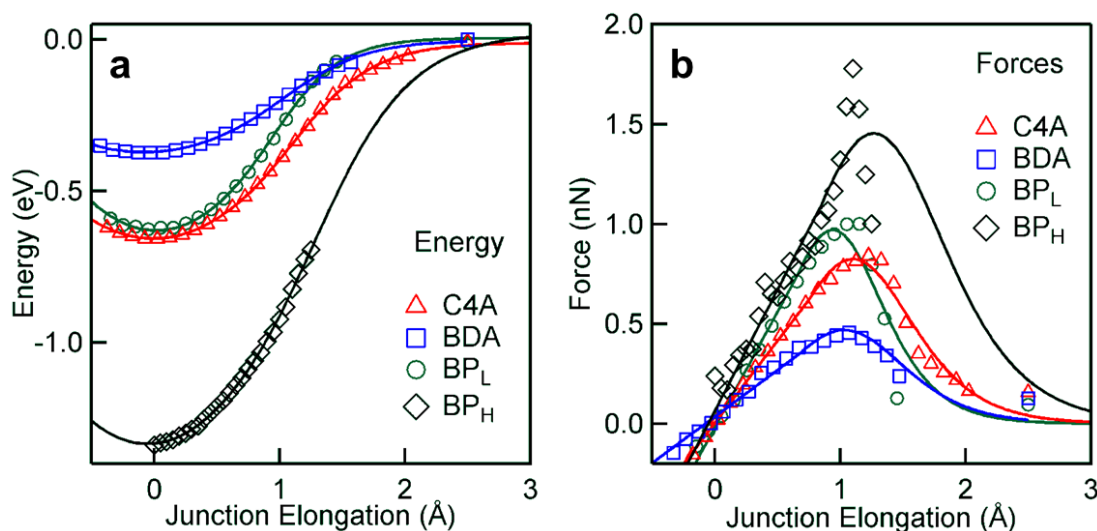
Figure 7.4. Fits to DFT simulations of Au-molecule-Au junctions with nitrogen terminated molecules. (a) Energies calculated by DFT adiabatic trajectory simulations (open symbols), and fits to the hybrid model potential (solid lines). (b) DFT calculated forces (open symbols) and derivative of the hybrid model potential (solid lines). The DFT calculation for **BP$_H$** included van der Waals corrections using the DFT-D2 approach, but with a single Au electrode due to computational constraints.

The DFT based adiabatic trajectory calculations were performed using the generalized gradient approximation (GGA) of Perdew, Burke, and Ernzerhof (PBE)[30] implemented in the VASP package[31]. In addition, for the van der Waals calculations for **BP** SMJs, the DFT-D2 method of Grimme [29] was used. The theoretical results for **C4SMe**, **C4A**, **BDA** and **BP** have been presented previously[9, 10, 15]. Figure 7.4a presents the fits of the model hybrid energy profile to the DFT calculated energies at different values of the junction elongation for **C4A**, **BDA**, **BP$_L$** and **BP$_H$** SMJs. In addition, the derivative of the hybrid potential is compared to the

forces obtained from DFT calculations (Figure 7.4b). Both the energies and forces calculated by the DFT are well-captured by the hybrid model in general, but the agreement in the forces for **BP$_H$** SMJs is poor beyond F_{max}. This could be due to the fact that close to F_{max}, the **BP** molecule rapidly loses its van der Waals binding energy contribution, leading to more complex potential energy variation that the donor-acceptor bonded junctions[10]. However, more work is needed to ascertain if this discrepancy is as artifact of the DFT-D2 approach.

7.5 References

1. A. Nitzan and M.A. Ratner, *Electron Transport in Molecular Wire Junctions.* Science, 2003. **300**(5624): p. 1384-1389.

2. C. Joachim, J.K. Gimzewski, and A. Aviram, *Electronics using hybrid-molecular and mono-molecular devices.* Nature, 2000. **408**(6812): p. 541-548.

3. B. Xu and N.J. Tao, *Measurement of Single-Molecule Resistance by Repeated Formation of Molecular Junctions.* Science, 2003. **301**(5637): p. 1221-1223.

4. M.A. Lantz, H.J. Hug, R. Hoffmann, P.J. van Schendel, P. Kappenberger, S. Martin, A. Baratoff, and H.J. Guntherodt, *Quantitative measurement of short-range chemical bonding forces.* Science, 2001. **291**(5513): p. 2580-3.

5. B.J. Albers, T.C. Schwendemann, M.Z. Baykara, N. Pilet, M. Liebmann, E.I. Altman, and U.D. Schwarz, *Three-dimensional imaging of short-range chemical forces with picometre resolution.* Nature Nanotechnology, 2009. **4**(5): p. 307-310.

6. Y. Sugimoto, P. Pou, M. Abe, P. Jelinek, R. Perez, S. Morita, and O. Custance, *Chemical identification of individual surface atoms by atomic force microscopy.* Nature, 2007. **446**(7131): p. 64-7.

7.   G. Rubio-Bollinger, S. Bahn, N. Agraït, K. Jacobsen, and S. Vieira, *Mechanical Properties and Formation Mechanisms of a Wire of Single Gold Atoms.* Physical Review Letters, 2001. **87**(2): p. 026101.

8.   M. Ternes, C. Gonzalez, C.P. Lutz, P. Hapala, F.J. Giessibl, P. Jelinek, and A.J. Heinrich, *Interplay of Conductance, Force, and Structural Change in Metallic Point Contacts.* Physical Review Letters, 2011. **106**(1): p. 016802.

9.   M. Frei, S.V. Aradhya, M. Koentopp, M.S. Hybertsen, and L. Venkataraman, *Mechanics and chemistry: single molecule bond rupture forces correlate with molecular backbone structure.* Nano Letters, 2011. **11**(4): p. 1518-1523.

10.   S.V. Aradhya, M. Frei, M.S. Hybertsen, and L. Venkataraman, *Van der Waals interactions at metal/organic interfaces at the single-molecule level.* Nature Materials, 2012. **11**(10): p. 872-876.

11.   B.Q. Xu, X.Y. Xiao, and N.J. Tao, *Measurements of single-molecule electromechanical properties.* Journal of the American Chemical Society, 2003. **125**(52): p. 16164-16165.

12.   S. Grimme, *Accurate description of van der Waals complexes by density functional theory including empirical corrections.* Journal of Computational Chemistry, 2004. **25**(12): p. 1463-1473.

13.   K. Lee, E. Murray, D., L. Kong, B.I. Lundqvist, and D.C. Langreth, *Higher-accuracy van der Waals density functional.* Physical Review B, 2010. **82**(8): p. 081101.

14.   K. Tonigold and A. Gross, *Adsorption of small aromatic molecules on the (111) surfaces of noble metals: A density functional theory study with semiempirical corrections for dispersion effects.* Journal of Chemical Physics, 2010. **132**(22): p. 224701.

15.   M. Frei, S.V. Aradhya, M.S. Hybertsen, and L. Venkataraman, *Linker dependent bond rupture force measurements in single-molecule junctions.* Journal of the American Chemical Society, 2012. **134**(9): p. 4003-6.

16.   N. Fournier, C. Wagner, C. Weiss, R. Temirov, and F.S. Tautz, *Force-controlled lifting of molecular wires.* Physical Review B, 2011. **84**(3): p. 035435.

17.   M.L. Trouwborst, E.H. Huisman, F.L. Bakker, S.J. van der Molen, and B.J. van Wees, *Single Atom Adhesion in Optimized Gold Nanojunctions.* Physical Review Letters, 2008. **100**(17): p. 175502.

18.   J. Welker and F.J. Giessibl, *Revealing the Angular Symmetry of Chemical Bonds by Atomic Force Microscopy.* Science, 2012. **336**(6080): p. 444-449.

19.   P.M. Morse, *Diatomic Molecules According to the Wave Mechanics. II. Vibrational Levels.* Physical Review, 1929. **34**(1): p. 57-64.

20. J.E. Jones, *On the determination of molecular fields - II From the equation of state of a gas.* Proceedings of the Royal Society of London Series A, 1924. **106**(738): p. 463-477.

21. J.H. Rose, J. Ferrante, and J.R. Smith, *Universal Binding-Energy Curves for Metals and Bimetallic Interfaces.* Physical Review Letters, 1981. **47**(9): p. 675-678.

22. S.V. Aradhya, J.S. Meisner, M. Krikorian, S. Ahn, R. Parameswaran, M.L. Steigerwald, C. Nuckolls, and L. Venkataraman, *Dissecting contact mechanics from quantum interference in single-molecule junctions of stilbene derivatives.* Nano Letters, 2012. **12**(3): p. 1643-7.

23. M.T. Gonzalez, A. Diaz, E. Leary, R. Garcia, M.A. Herranz, G. Rubio-Bollinger, N. Martin, and N. Agrait, *Stability of Single- and Few-Molecule Junctions of Conjugated Diamines.* Journal of the American Chemical Society, 2013. **135**(14): p. 5420-5426.

24. F.J. Ribeiro and M.L. Cohen, *Ab initio pseudopotential calculations of infinite monatomic chains of Au, Al, Ag, Pd, Rh, and Ru.* Physical Review B, 2003. **68**(3): p. 035423.

25. D. Sanchez-Portal, E. Artacho, J. Junquera, P. Ordejon, A. Garcia, and J.M. Soler, *Stiff monatomic gold wires with a spinning zigzag geometry.* Physical Review Letters, 1999. **83**(19): p. 3884-3887.

26. J.A. Dean, ed. *Lange's Handbook of Chemistry*. 15 ed. 1999, McGraw-Hill.

27. S.V. Aradhya, M. Frei, A. Halbritter, and L. Venkataraman, *Correlating Structure, Conductance, and Mechanics of Silver Atomic-Scale Contacts.* ACS Nano, 2013. **7**(4): p. 3706-3712.

28. N.A. Lambropoulos, J.R. Reimers, and N.S. Hush, *Binding to gold(0): Accurate computational methods with application to AuNH(3).* Journal of Chemical Physics, 2002. **116**(23): p. 10277-10286.

29. S. Grimme, *Semiempirical GGA-type density functional constructed with a long-range dispersion correction.* Journal of Computational Chemistry, 2006. **27**(15): p. 1787-1799.

30. J.P. Perdew, K. Burke, and M. Ernzerhof, *Generalized gradient approximation made simple.* Physical Review Letters, 1996. **77**(18): p. 3865-3868.

31. G. Kresse and J. Furthmuller, *Efficient iterative schemes for ab initio total-energy calculations using a plane-wave basis set.* Physical Review B, 1996. **54**(16): p. 11169-11186.

8

Conclusions and outlook

The experimental setup and analysis techniques outlined in this thesis have proven to be effective in probing a variety of important questions surrounding the structure-function relationships at the atomic scale. These include the quantitative studies of rupture forces across a wide variety of molecular backbones and chemical linker groups and even atomic impurities in silver atomic contacts, measurement of van der Waals forces at the metal-molecule interface, demonstration of destructive quantum interference and the reconstruction of binding energy profiles from experiments. Other than the improvement of instrumentation capabilities and optimization of signal-to-noise ratios, several interesting questions appear to be addressable in the near future using simultaneous measurements of force and conductance across single molecule junctions. Ultimately, it remains to be seen if we can progress from merely studying physical processes, to actively manipulating matter at the atomic scale to perform useful functions.

8.1 Conclusions

We have presented our studies of atomic-scale junctions through the simultaneous measurements of force and conductance. These experimental and analysis techniques have yielded a wealth of information that highlights the relationships between chemical structure, junction mechanics, electronic transport and energetics, stemming from their underlying electronic structure. While the motivations for such studies in the past came from the drive to build-up new electronic devices and architectures starting from the atomic scale, our explorations are indicating new directions for research by probing multiple properties of these junctions.

Starting from a discussion of the experimental setup, measurement protocols and statistical analysis techniques, we proceeded to see their combined application in correlating the chemical structure of various molecules with their junction rupture forces. Then we used systematic measurements of conductance in junctions formed by a series of carboxyl linked molecules in combination with force measurements to estimate their stability. This led us to an understanding of the binding mechanism for carboxyl linker groups, which paves the way for future studies that can take advantage of the chemical modifications achievable through the carboxyl group. We then applied force-based analysis techniques to dissect the junction mechanics, stemming mostly from the contact mechanics at the linker-gold bond, from the signatures of destructive quantum interference in electronic transport of single-molecule junctions of *meta-* terminated molecules. Here we found that by using specially designed molecules, we can retain the mechanical stability of the contacts, while drastically changing the electronic transport properties of single-molecule junctions. The lessons from this study have already motivated another series of experiments to probe electronic transport in the absence of specific interactions.

Going beyond characterizations of rupture force alone, we demonstrated the first quantitative measurement of van der Waals forces at the metal-molecule interface at the single-molecule level through detailed analyses of forces, stiffnesses and structural rearrangements. Van der Waals forces are a manifestation of electronic correlations that are ubiquitous in nature and engineered material, but remains challenging to estimate either through experiment or theory. Our combined experimental and theoretical approach to measure these forces can provide a new understanding of important relationships between electronic structure and interfacial mechanics. We then extended these methods to silver atomic-scale junctions, where we used relationships between conductance and structure were exploited to distinguish between pristine and oxygen contaminated silver junctions. Once more, simple explanations emerged in the correlations between structural motifs at the atomic scale, and their conductance and mechanical evolution.

Finally, we proposed a simplified analytical model that captures the essence of the many-body mechanics occurring in the vicinity of the junction in order to quantitatively extract the energies and length scales of the relevant binding energy profiles. So far, the quantitative estimates for binding energy from experiments were largely limited to course-grained methods such as temperature programmed desorption, while theoretical calculations provided reliable estimates only in relatively simple bonding scenarios. Our new technique presents a universal way to obtain binding energy profiles directly from experiments, and can therefore be useful in benchmarking future theoretical calculations as well.

8.2   Outlook

One of the important challenges that we overcame in order to enable our experiments was the dramatically improved force resolution that we achieved through careful optimization of the

instrumentation. However, significant improvements are still possible, as the fundamental noise limit (thermal noise of the AFM cantilever) have not yet been reached. Further optimization of the laser optics, combined with customized beam deflection detection and pre-amplifier based electronic amplification of the photodetector signal to achieve thermal-limited performance could lower the force noise from ~ 0.1 nN currently, to ~ 0.03 nN. There is also scope for adding other measurement capabilities, in addition to the conductance and force capabilities, especially for optical probing, because the gold-coated AFM cantilever presents an ideal opportunity to utilize local plasmonic resonances in order to enhance the optical coupling to single molecules. While the modifications are challenging, they will open the door for many interesting studies where mechanics can be used to alter not only the electronic transport but potentially the optical properties as well.

Another avenue for future work lies in the development of new analysis techniques to extract more information from both existing and future datasets. This is because, in our studies so far, we have mostly explored correlations between different properties that have been averaged over thousands of individual realizations of atomic-scale junctions. While this was thought to be necessary to obtain statistically relevant comparisons, we are now at a stage in the experimental and analytical ability that it is possible to correlate not only averaged properties, but also obtain statistically robust cross-correlations between different properties of individual junctions, such as their conductance, rupture force, stiffness and the variability in each of these parameters on a junction-by-junction basis. Finally, an important prospect well-suited for our AFM experiments is to explore mechano-chemistry, where forces induce structural changes detectable by changes in electronic transport properties.

8.3 List of publications

1. S.V. Aradhya, M.S. Hybertsen, and L. Venkataraman, *Experimentally Quantifying the Binding Energetics of Atomic-Scale Junctions*, under preparation.

2. S.V. Aradhya and L. Venkataraman, *Single-Molecule Junctions Beyond Electronic Transport*. Nature Nanotechnology, 2013. **8**(6): p. 399-410.

3. S.V. Aradhya, M. Frei, A. Halbritter, and L. Venkataraman, *Correlating Structure, Conductance, and Mechanics of Silver Atomic-Scale Contacts*. ACS Nano, 2013. **7**(4): p. 3706-3712.

4. S.V. Aradhya, M. Frei, M.S. Hybertsen, and L. Venkataraman, *Van der Waals Interactions at Metal/Organic Interfaces at the Single-Molecule Level*. Nature Materials, 2012. **11**(10): p. 872-876.

5. S.V. Aradhya, J.S. Meisner, M. Krikorian, S. Ahn, R. Parameswaran, M.L. Steigerwald, C. Nuckolls, and L. Venkataraman, *Dissecting Contact Mechanics from Quantum Interference in Single-Molecule Junctions of Stilbene Derivatives*. Nano Letters, 2012. **12**(3): p. 1643-1647.

6. S.V. Aradhya, M. Frei, M.S. Hybertsen, and L. Venkataraman. *Simultaneous Measurement of Force and Conductance Across Single Molecule Junctions*. in *Proceedings of the Annual Conference on Experimental & Applied Mechanics*. 2012. Costa Mesa, CA: Springer.

7. S. Ahn, S.V. Aradhya, R.S. Klausen, B. Capozzi, X. Roy, M.L. Steigerwald, C. Nuckolls, and L. Venkataraman, *Electronic Transport and Mechanical Stability of Carboxyl Linked Single-Molecule Junctions*. Physical Chemistry and Chemical Physics, 2012. **14**(40): p. 13841-13845.

8. M. Frei, S.V. Aradhya, M.S. Hybertsen, and L. Venkataraman, *Linker Dependent Bond Rupture Force Measurements in Single-Molecule Junctions*. Journal of the American Chemical Society, 2012. **134**(9): p. 4003-4006.

9. J.S. Meisner, S. Ahn, S.V. Aradhya, M. Krikorian, R. Parameswaran, M. Steigerwald, L. Venkataraman, and C. Nuckolls, *Importance of Direct Metal−π Coupling in Electronic Transport Through Conjugated Single-Molecule Junctions*. Journal of the American Chemical Society, 2012. **134**(50): p. 20440-20445.

10. M. Frei, S.V. Aradhya, M. Koentopp, M.S. Hybertsen, and L. Venkataraman, *Mechanics and Chemistry: Single Molecule Bond Rupture Forces Correlate with Molecular Backbone Structure*. Nano Letters, 2011. **11**(4): p. 1518-1523.